Protein Dielectrophoresis Using Insulator-based Microfluidic Platforms

by

Asuka Nakano

A Dissertation Presented in Partial Fulfillment
of the Requirements for the Degree
Doctor of Philosophy

Approved April 2014 by the
Graduate Supervisory Committee:

Alexandra Ros, Chair
Mark Hayes
Marcia Levitus

ARIZONA STATE UNIVERSITY

May 2014

ABSTRACT

Rapid and reliable separation and analysis of proteins require powerful analytical methods. The analysis of proteins becomes especially challenging when only small sample volumes are available, concomitantly with low concentrations of proteins. Time critical situations pose additional challenges. Due to these challenges, conventional macro-scale separation techniques reach their limitations. While microfluidic devices require only pL-nL sample volumes, they offer several advantages such as speed, efficiency, and high throughput.

This work elucidates the capability to manipulate proteins in a rapid and reliable manner with a novel migration technique, namely dielectrophoresis (DEP). Since protein analysis can often be achieved through a combination of orthogonal techniques, adding DEP as a gradient technique to the portfolio of protein manipulation methods can extend and improve combinatorial approaches. To this aim, microfluidic devices tailored with integrated insulating obstacles were fabricated to create inhomogeneous electric fields evoking insulator-based DEP (iDEP).

A main focus of this work was the development of pre-concentration devices where topological micropost arrays are fabricated using standard photo- and soft lithographic techniques. With these devices, positive DEP-driven streaming of proteins was demonstrated for the first time using immunoglobulin G (IgG) and bovine serum albumin. Experimentally observed iDEP concentrations of both proteins were in excellent agreement with positive DEP concentration profiles obtained by numerical simulations. Moreover, the micropost iDEP devices were improved by introducing nano-constrictions with focused ion beam milling with which numerical simulations suggested enhancement

of the DEP effect, leading to a 12-fold increase in concentration of IgG. Additionally, concentration of β-galactosidase was observed, which seems to occur due to an interplay of negative DEP, electroosmosis, electrokinesis, diffusion, and ion concentration polarization. A detailed study was performed to investigate factors influencing protein DEP under DC conditions, including electroosmosis, electrophoresis, and Joule heating. Specifically, temperature rise within the iDEP device due to Joule heating was measured experimentally with spatial and temporal resolution by employing the thermosensitive dye Rhodamine B. Unlike DNA and cells, protein DEP behavior is not well understood to date. Therefore, this detailed study of protein DEP provides novel information to eventually optimize this protein migration method for pre-concentration, separation, and fractionation.

DEDICATION

To my family, especially my mother and father for their love and support.

To my boyfriend, Ruben for being by my side.

To all my friends for their advice, help, and time spent together.

ACKNOWLEDGEMENT

First and foremost, I would like to express my deep gratitude to my doctoral committee chair, Professor Alexandra Ros for her support, guidance, and constructive criticism throughout the five years of the course of my graduate studies.

I also would like to thank my doctoral committee members, Professor Mark Hayes and Professor Marcia Levitus for their helpful feedback and fruitful discussions.

For the material presented in chapter 5 and 6, I would like to thank co-authors Dr. Tzu-Chiao Chao and Dr. Fernanda Camacho-Alanis from the Department of Chemistry and Biochemistry at Arizona State University. Additionally, I would like to thank Professor Rebecca Wachter and Dr. J. Nathan Henderson in the Chemistry and Biochemistry Department at Arizona State University for assistance with the dynamic light scattering experiments reported in the supplementary information as well as Bryant Doss and Professor Robert Ros in the Department of Physics at Arizona State University for technical assistance with AFM imaging.

For the material presented in chapter 7, I would like to thank co-author Jinghui Luo in addition to Dr. Fernanda Camacho-Alanis for fruitful discussions and Kathleen Bush at Arizona State University for help with fluorescence measurements in microfluidic channels.

Finally, I would like to thank all my fellow graduate students and lab mates at Alexandra Ros lab for their assistance on a daily basis.

TABLE OF CONTENTS

LIST OF TABLES

LIST OF FIGURES

FIGURE Page

FIGURE Page

FIGURE Page

CHAPTER 1

INTRODUCTION

Manipulation of biomolecules poses serious analytical challenges in the area of biomedical and pharmaceutical research. Therefore, reliable and rapid separation techniques are in demand especially for proteins within extremely complex mixtures such as cell lysates, tissues, or body fluids. For instance, rapid separation techniques are necessary in time critical situations such as surgeries and with the analytes degrading rapidly over time. Moreover, low abundant proteins such as disease biomarkers need to be identified and detected with high sensitivity for further diagnostic purposes. Another analytical challenge arises for sample available only in limited amount. Therefore, powerful methods which require only low sample volumes with the ability to concentrate analytes are demanded.

Dielectrophoresis (DEP) is a powerful analytical technique occurring in an inhomogeneous electric field that has the potential to facilitate many processing steps such as pre-concentration, purification, fractionation, and separation. Such a versatile applicability makes DEP an attractive analytical method for biological particles and biomolecules. For instance, a variety of DEP application has been demonstrated in the past including cell separation (Hu et al., 2005; Pethig, 1996), fractionation (X.-B. Wang et al., 2000, 2000; Yang, Huang, Wang, Becker, & Gascoyne, 1999), cytometry (Voldman, Gray, Toner, & Schmidt, 2002), and patterning (Albrecht, Underhill, Wassermann, Sah, & Bhatia, 2006). Moreover, DEP can be used to precisely manipulate and position cells (Gagnon, 2011) and even single molecules (Hölzel, Calander, Chiragwandi, Willander, & Bier, 2005), which makes it a very attractive candidate for

nanotechnological applications (Koh, 2007). This transport phenomenon occurs in an inhomogeneous electric field when particles suspended in an aqueous solution acquire an induced dipole and become polarizable. Since the biomolecule's DEP response is based on their intrinsic properties, DEP can serve as a label-free technique which is important when further processing and/or characterization steps are necessary.

The analysis of proteins often requires powerful separation, fractionation, and pre-concentration techniques, which can in many cases only be achieved through the combination of orthogonal techniques. Adding a novel tool, such as DEP, to the portfolio of protein manipulation techniques has thus large potential to improve protein analysis techniques. As a gradient technique, DEP seems highly suited to extend current protein separation methods as it has the potential to both provide a concentration tool (note that proteins cannot be amplified in contrast to DNA) and improve current separation approaches especially in combination with other orthogonal techniques.

The selectivity of DEP stems from the polarizability of biomolecules in the presence of electric field gradients. An excellent theoretical framework to describe polarizability mechanisms exists for large colloidal particles (Jones, 2005) and biological particles such as cells, viruses, and organelles. For example, DEP response of cells is described using a shell model which assigns different permittivities to each compartment of the cell in the form of layers of shells to calculate an overall effective cell permittivity (Gagnon, 2011; Jones, 2005; Pethig, 2010; Voldman, 2006). However, the models developed for these large cellular structures and viruses are not directly applicable to sub-micrometer sized biomolecules such as DNA and proteins. In case of DNA, the theoretical DEP models are less developed and still under debate especially on the subject

of DNA length and frequency dependence (Henning, Bier, & Hölzel, 2010; Zhao, 2011b). However, it is generally assumed that DNA polarization is mainly caused by the ion cloud surrounding the negatively charged DNA backbone. Nevertheless, a number of DNA DEP applications have been demonstrated including concentration (Swami, Chou, Ramamurthy, & Chaurey, 2009), fractionation (Washizu, Suzuki, Kurosawa, Nishizaka, & Shinohara, 1994), and separation (Huang et al., 2002; Regtmeier, Duong, Eichhorn, Anselmetti, & Ros, 2007; Regtmeier, Eichhorn, Bogunovic, Ros, & Anselmetti, 2010) ranging from Mbp down to ~40 bp DNA length.

For proteins, the mechanism of polarization responsible for DEP transport is not well understood. Theoretically, DEP manipulation of sub-micrometer sized proteins is challenging since extremely high electric field gradients are required in order to generate DEP forces large enough to compete with particle diffusion, electrokinetic, and electrothermal forces. Regardless, nearly 20 groups have investigated protein DEP experimentally employing metal electrodes (Bakewell, Hughes, Milner, & Morgan, 1998; Hölzel et al., 2005; Washizu et al., 1994; Zheng, Brody, & Burke, 2004) , nanopipettes (Clarke, Piper, Ying, & Klenerman, 2007), carbon nanotubes (Maruyama & Nakayama, 2008), and in droplets (Agastin, King, & Jones, 2009). For instance, Hölzel demonstrated single molecule DEP trapping by creating high $\nabla \boldsymbol{E}^2$ of 10^{21} V^2/m^3 (Hölzel et al., 2005). Moreover, protein DEP has been applied for patterning (Asokan et al., 2003; Washizu et al., 1994), bioprobe (Maruyama & Nakayama, 2008), and biosensor (Gong, 2010) applications. Recently several experimental studies have reported insulator-based DEP (iDEP) devices for proteins including the first work by Lapizco-Encinas (Lapizco-Encinas, Ozuna-Chacón, & Rito-Palomares, 2008a) and the first protein DEP streaming

presented by our group (Nakano, Chao, Camacho-Alanis, & Ros, 2011). For protein iDEP trapping, designing a suitable device capable of generating extremely high electric field gradients is necessary, for example as demonstrated with nano-sized constriction devices (Camacho-Alanis, Gan, & Ros, 2012; Liao & Chou, 2012; Liao, Tsegaye, Chaurey, Chou, & Swami, 2012).

DISSERTATION WORK METHODOLOGY

The main objectives of this dissertation are to provide the field of protein DEP using insulator-based devices with:

1. Development of iDEP devices which can create high enough electric field gradients suitable for protein manipulations.
2. An experimental study of diagnostically relevant proteins such as immunoglobulin G (IgG) using tailored iDEP devices.
3. Validation of the experimental investigations with the aid of numerical simulation tools.
4. Extension of protein iDEP study to a wide variety of proteins, such as bovine serum albumin (BSA) and β-galactosidase.
5. Systematic investigation of protein iDEP in order to achieve a better understanding of protein polarization mechanisms.

This dissertation is organized into eight main chapters. Chapter 2 provides a brief review of protein DEP which mainly includes experimental work performed in the past. Chapter 3 explains simulation methodology used to model protein concentration distributions as well as temperature fields within a microfluidic iDEP device. Chapter 4

presents the experimental methods employed to perform iDEP experiments. Chapter 5 presents protein iDEP experiments using micropost array iDEP devices under DC conditions and examines factors influencing protein DEP. Chapter 6 presents protein iDEP experiments using the improved iDEP device with integrated nano-constriction arrays. Chapter 7 presents the experimentally measured temperature distributions occurring due to Joule heating within the iDEP devices. Finally, Chapter 8 provides a summary of my work as well as suggestions for future work which extends the results of this dissertation.

ELECTROKINETIC TRANSPORT IN MICROFLUIDIC DEVICES

In this section, I will give a brief explanation of how electrokinetic transport occurs in a microfluidic system including electroosmosis (EO) and electrophoresis (EP).

Electroosmosis. Electroosmosis is the motion of bulk fluid under the application of electric field, occurring due to the presence of an electrical double layer (EDL) adjacent to the charged walls of a microfluidic channel. The channel walls usually acquire charges on its surfaces when they are in contact with aqueous solutions. For instance, poly(dimethysiloxane) (PDMS) employed for many microfluidic applications has negatively changed walls at pHs between 3 and 5 at which surface silanol groups are deprotonated in an aqueous solutions (Iler, 1979). Such charged walls lead to the formation of a shielding layer where counterions are drawn towards the walls, while co-ions are repelled away from them. This shielding layer termed EDL is comprised of the Stern layer and the diffuse layer. In order to balance the surface charge of the channel walls, counterions are absorbed onto the walls, leading to the formation of a charged

layer with immobilie ions (Stern layer). On the other hand, ions can move by diffusion at the outer layer, thus termed diffuse layer. As depicted schematically in *Figure 1-1*a, the magnitude of electrical potential decreases exponentially as moving away from the wall with the characteristic distance given by Debye length expressed as:

$$\lambda_D = \left(\frac{\varepsilon_0 \varepsilon_r k_B T}{e^2 \sum_i n_i^\infty z_i^2}\right)^{1/2} \quad (1.\ 1)$$

where ε_0 denotes the permittivity of free space, ε_r is relative permittivity, k_B is the Boltzmann constant, T is temperature, e is the elementary charge, and n_i^∞ is the bulk volume density.

Upon application of an external electric field, redistribution of ion in the vicinity of the interface leads to the increased local charge density, which in turn results in the motion of the fluid, termed electroosmosis (EO). EO is characterized by the bulk fluid motion, therefore the electroosmotic flow (EOF) shows a uniform velocity profile throughout the cross section of the channel and drops rapidly to zero at the solid-liquid interface as shown in *Figure 1-1*b. The electroosmotic velocity ($\boldsymbol{u_{eof}}$) is described by the following Smoluchowski equation (von Smoluchowski, M., 1914):

$$\boldsymbol{u_{eof}} = \mu_{eof} \boldsymbol{E} = -\frac{\varepsilon \zeta}{\eta} \boldsymbol{E} \quad (1.\ 2)$$

where μ_{eof} denotes the electroosmotic mobility, $\boldsymbol{E}$ is the electric field, ε is the medium permittivity, η is the buffer viscosity, and ζ is the zeta potential.

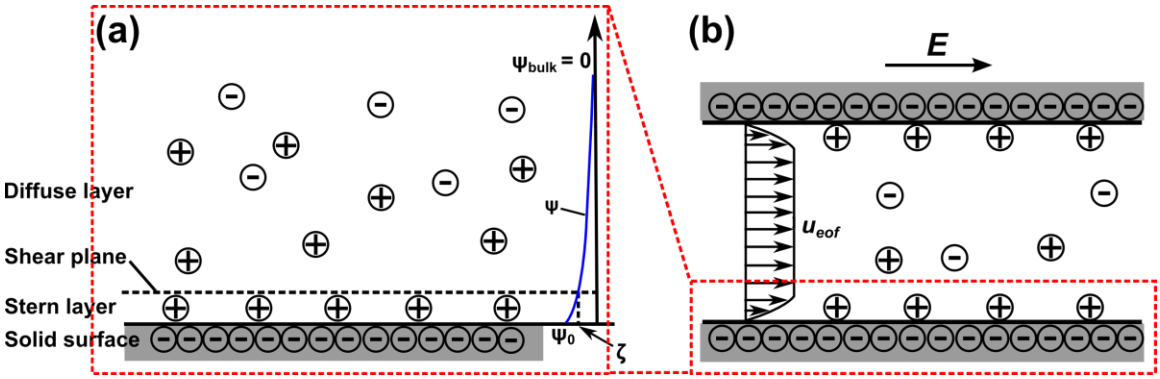

Figure 1-1. Schematic depiction of the electrical double layer (EDL) and the mechanism of electroosmosis. (a) EDL is formed at the interface of solid and liquid (not to scale). When the surface of a microfluidic channel (gray) acquires negative charges, counterions are absorbed onto the surface, resulting in the immobile layer (Stern layer). Diffuse layer is formed just beyond the Stern layer and it is responsible for the electrokinetic phenomena. Electrical potential (ψ) distribution (shown in blue line) decreases while moving away from the surface and becomes zero in the bulk. ζ indicates the zeta potential at the shear plane. (b) EOF profile inside of the microfluidic channel under an applied electric field ($\boldsymbol{E}$). On the negatively charged wall (gray), positive counterions are adsorbed, creating an immobile Stern layer. Fluid velocity is uniform throughout the cross section of the channel and drops to zero at the interface (no-slip).

Electrophoresis. Electrophoresis is defined as the motion of a particle freely suspended in a liquid medium, relative to a stationary liquid upon application of an electric field. Due to electrophoresis, the charged particles move along the electric field lines. For instance, a positively charged particle migrates in the cathodic direction, whereas the neutral particle remains stationary (Lyklema, J., 1995). When a particle migrates at a constant velocity under the application of a homogeneous electric field ($\boldsymbol{E}$), the electrical force is in balance with the viscous drag and the electrophoretic velocity ($\boldsymbol{u_{ep}}$) can be expressed as:

$$\boldsymbol{u_{ep}} = \mu_{ep}\boldsymbol{E} = {}^{q}/_{f}\,\boldsymbol{E} \qquad (1.\ 3)$$

where μ_{ep} is the electrophoretic mobility, q is the charge on the particle, and f is the friction coefficient. Separation of multiple species can be achieved due to the difference

in the rate of migration which depends on the size, shape, and charge of each species (Lyklema, J., 1995).

DIELECTROPHORESIS

Theory of Dielectrophoresis. Dielectrophoresis (DEP) refers to the migration of a polarizable particle in an inhomogeneous electric field ($\boldsymbol{E}$). For most DEP applications, it is useful to describe the force acting on a polarizable particle. The DEP force ($\boldsymbol{F}_{dep}$) acting on a particle is related to the apparent dipole moment, $\boldsymbol{m}$ (Pohl, 1978):

$$\boldsymbol{F_{DEP}} = (\boldsymbol{m} \cdot \nabla)\boldsymbol{E} \tag{1. 4}$$

For an induced dipole moment, equation (1. 4) can also be expressed in terms of the particle polarizability α (Pohl, 1978):

$$\boldsymbol{F}_{dep} = \frac{1}{2}\alpha\, \upsilon\, \nabla \boldsymbol{E^2} \tag{1. 5}$$

where υ denotes the particle volume. In classical DEP theory, the time averaged DEP force for a spherical particle in a medium of permittivity ε_m is given as (Pohl, 1978):

$$\langle \boldsymbol{F}_{dep} \rangle = 2\pi\varepsilon_m r^3 Re[K(\omega)]\nabla|\boldsymbol{E_{rms}}|^2 \tag{1. 6}$$

where r is the particle radius, ω the angular frequency, $\boldsymbol{E}_{\text{rms}}$ the root mean square electric field, and $Re[K(\omega)]$ the real part of the Clausius-Mossotti factor given as:

$$Re[K(\omega)] = \left(\frac{\varepsilon_p^* - \varepsilon_m^*}{\varepsilon_p^* + 2\varepsilon_m^*}\right) \tag{1. 7}$$

Here, ε_p^* and ε_m^* denote the complex permittivities of the particle (p) and medium (m), respectively. The complex permittivity for the particle (and similarly for the medium) is given by $\varepsilon_p^* = \varepsilon_p - j\frac{\sigma_p}{\omega}$, where σ_p denotes the particle conductivity, and j=$\sqrt{-1}$. The

Clausius-Mossotti factor is characteristic for the DEP response. Depending on the sign of the Clausius-Mossotti factor, particles are attracted to the regions of highest electric fields or repulsed from those regions as shown schematically in *Figure 1-2*. These two cases refer to positive DEP (pDEP, see *Figure 1-2*a) and negative DEP (nDEP, see *Figure 1-2*b), respectively. Equation (1. 6) demonstrates the frequency dependence of the dielectrophoretic response of a sphere and allows estimating the resulting forces in electric field gradients. At high frequency, $\boldsymbol{F}_{dep}$ is typically governed by the particle permittivity, while at low frequency and under DC conditions the Clausius-Mossotti factor is dominated by the conductivity of the particle and the medium. Moreover, the frequency dependent change from positive to negative DEP is characterized by the so-called crossover frequency where the Clausius-Mossotti factor reverses its sign. The polarization effects on particles are often studied by investigating the changes in crossover frequency.

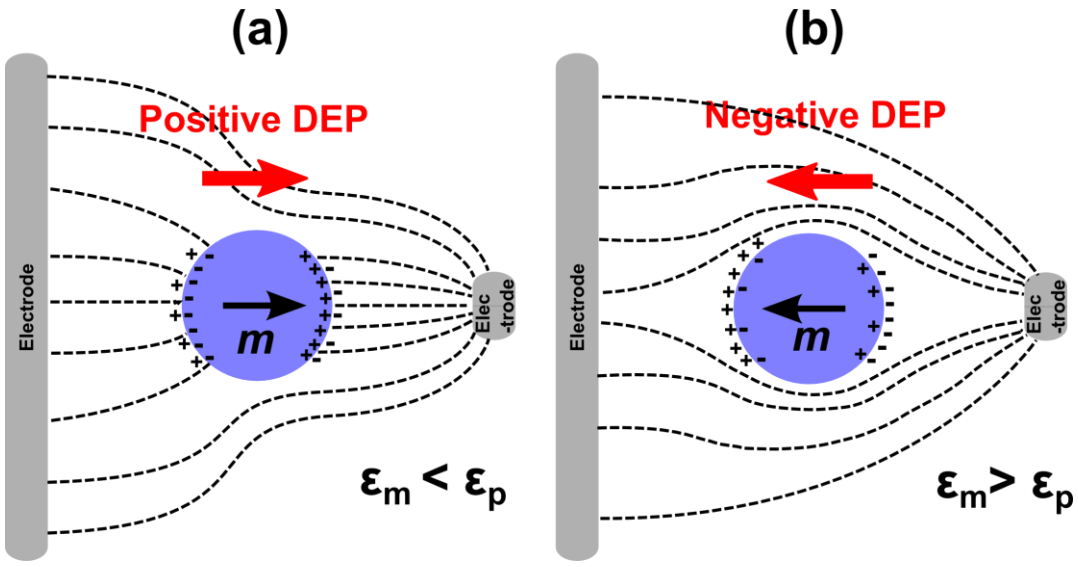

Figure 1-2. Schematic representation of a mechanism of DEP occurring under an inhomogeneous electric field by which a particle is transported (a) toward the higher electric field gradient (positive DEP) or (b) away from it (negative DEP).

Prior Work in Dielectrophoresis. The wide range of DEP applications allows not only for transport of particles or proteins along or against the electric field gradient, but also their concentration. These characteristics make DEP appealing for analytical applications such as fractionation, pre-concentration, and separation methods. Moreover, DEP has the potential to precisely manipulate and position small particles such as cells (Clow, Gaynor, & Oback, 2010; Jaber, Labeed, & Hughes, 2009; MacQueen, Buschmann, & Wertheimer, 2008) or even single molecules (Hölzel et al., 2005), which is important for a variety of nanotechnological applications (Koh, 2007). For example, DEP of biological particles has demonstrated widespread applications. Those include cell separation (H. Li & Bashir, 2002; Pommer et al., 2008), fractionation (X.-B. Wang et al., 2000; Yang, Huang, Wang, Becker, & Gascoyne, 2000; Yang, Huang, Wang, Wang, et al., 1999), cytometry (Voldman et al., 2002), or patterning (Albrecht et al., 2006) and can be achieved selectively for various cell types. Additionally, DEP allows the manipulation of biological objects such as cells without labeling strategies (Jaber et al., 2009; MacQueen et al., 2008). This is also an important aspect for analytical applications of proteins where label-free strategies are desired.

As DEP is expected to occur for particles with induced dipole, a dielectrophoretic response from biomolecules is also predicted. Among biomolecules, DNA has been characterized most intensively, although the mechanism of polarization and the length and frequency dependence remain still debated (Henning et al., 2010; Zhao, 2011b). Commonly, a polarization of the counterions surrounding the negatively charged DNA backbone is assumed to be responsible for DNA DEP. Theoretical models describing the DNA DEP response are available including influences from convection, diffusion, and

electrophoretic migration (Zhao & Bau, 2009; Zhao, 2011a), however they fail to describe DNA response in a general manner and do not apply to the variety of experimentally observed scaling laws and DNA DEP response. Nonetheless, various bioanalytical applications employing DEP of DNA have been demonstrated, including separation (Huang et al., 2002; Regtmeier et al., 2007, 2010), fractionation (Beech, Jönsson, & Tegenfeldt, 2009; Washizu et al., 1994), and concentration (Swami et al., 2009).

The potential of DEP for protein manipulation and analysis has been recognized and pioneered by Washizu et al. almost 20 years ago (Washizu et al., 1994). In their work, the possibility of fractionation of proteins was outlined as well as some fundamental characteristics of biomolecule DEP. Microfabricated electrodes were introduced to generate high electric field gradients in microchip devices in order to compensate for the small polarizability expected for proteins in comparison with micrometer-sized objects such as cells. Follow up work mainly by Hughes, Morgan, and coworkers showed a more detailed investigation of selected proteins on patterned microelectrodes as well as a characteristic frequency dependence of protein DEP (Bakewell et al., 1998; Michael Pycraft Hughes, 2002). In the last decade, the interest in protein DEP intensified due to the demand in protein analysis tools as well as the improvement of micro- and nanofabrication techniques applied to protein DEP (e.g. as sensing tools or in microfluidic devices) (Lapizco-Encinas & Rito-Palomares, 2007). The following chapter summarizes protein DEP experimental work performed in the past, selected simulations, and the applications utilizing protein DEP.

CHAPTER 2

CURRENT STATUS OF DIELECTROPHORESIS

DEVICES TO STUDY PROTEIN DEP

Two types of devices have been used to create an inhomogeneous electric field necessary for DEP to occur: electrode-based DEP devices and insulator-based devices. In the former case, microelectrodes are integrated in a device employing microfabrication techniques. Some examples include interdigitated electrodes (Washizu et al., 1994), quadruple electrode geometries (Bakewell et al., 1998; Zheng et al., 2004), and pairs of triangular electrodes in close proximity to one another (Hölzel et al., 2005). These electrode-based DEP (eDEP) techniques have been employed most commonly in the field of protein DEP. Another relatively new technique termed insulator-based DEP (iDEP) utilizes insulating constrictions integrated within the device. Only a few examples can be found for protein iDEP including sawtooth constrictions (Staton et al., 2012), insulating post arrays with various geometries (Lapizco-Encinas et al., 2008a; Nakano et al., 2011), and nano-constrictions (Liao, Chaurey, Tsegaye, Chou, & Swami, 2011; Liao et al., 2012; Liao & Chou, 2012).

Figure 2-1 depicts eDEP and iDEP schematically as well as the typical ranges of $\boldsymbol{E}$ and $\nabla \boldsymbol{E}^2$ in these devices. In case of eDEP, metal microelectrodes are fabricated with a separation distance normally within the micrometer range requiring the application of low potential (up to ~ 20 V). In case of iDEP, the post geometry and dimension within a microfluidic channel greatly influence the acting field gradients. In contrast to eDEP, iDEP is mostly employed under DC condition with relatively high voltage applied. Thus, the resolution of the employed fabrication techniques limits the achievable electric fields

and gradients thereof. Commonly, photolithographic techniques are used, resulting in micrometer post sizes and distances. As shown in *Figure 2-1*, eDEP can generally create larger $\boldsymbol{E}$ and $\nabla \boldsymbol{E}^2$ with only a few volts applied and thus eDEP has been the major strategy for protein applications. However, these high gradients act only in the vicinity of the electrodes, which might become disadvantageous for separations in microchannels. In order to generate a comparable magnitude of $\boldsymbol{E}$ and $\nabla \boldsymbol{E}^2$ with iDEP devices, one can improve suitable geometries (Nakano et al., 2011) or even include nanometer-sized structures (Camacho-Alanis et al., 2012; Liao et al., 2011, 2012; Liao & Chou, 2012). However, iDEP prevents complicated processing steps, such as integrating metal electrodes in a microfluidic device, and moreover provides the non-uniform field over the entire depth of the microchannel, as compared to flat metal electrodes shown in *Figure 2-1*c and d. Additionally, electrode reactions interfere less with the analytes manipulated by DEP since the electrodes are placed far away from the insulating post regions where DEP occurs. In the following section the device geometries used in protein DEP studies will be discussed in greater detail (see also *Figure 2-2*), together with the major experimental findings. More thorough details on other experimental techniques used for DEP studies which have not been applied to protein DEP can be found in other reviews (Michael P. Hughes, 2002; Lapizco-Encinas & Rito-Palomares, 2007; Martinez-Duarte, 2012; Meighan, Staton, & Hayes, 2009; Srivastava, Gencoglu, & Minerick, 2011; Zhang, Khoshmanesh, Mitchell, & Kalantar-zadeh, 2010).

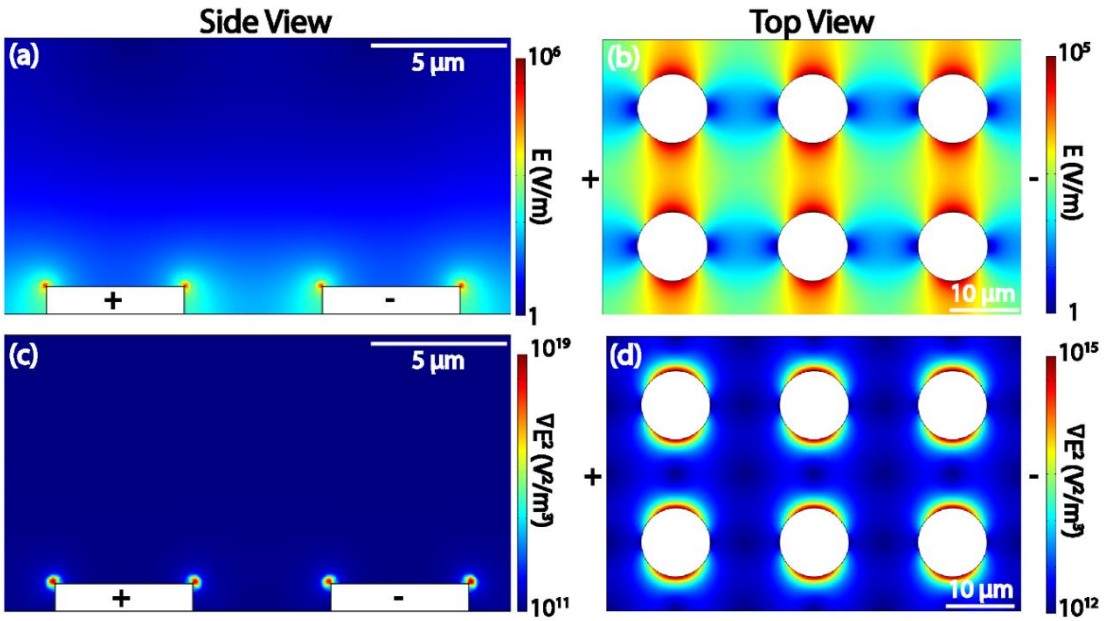

Figure 2-1. Schematic depiction of eDEP and iDEP devices. (a, c) Represent a side view for an eDEP and (b,d) a top view of an insulator-based DEP geometry. (a) Shows the electric field distribution and (c) $\nabla \boldsymbol{E}^2$ values resulting within the eDEP device with 5 V applied between the metal microelectrodes. (b) shows the electric field distribution and (d) $\nabla \boldsymbol{E}^2$ created by an iDEP device with the application of 500 V/cm. Note that the potential is usually applied via electrodes immersed in reservoirs at the end of the microchannel and only a small portion of a post array is represented here.

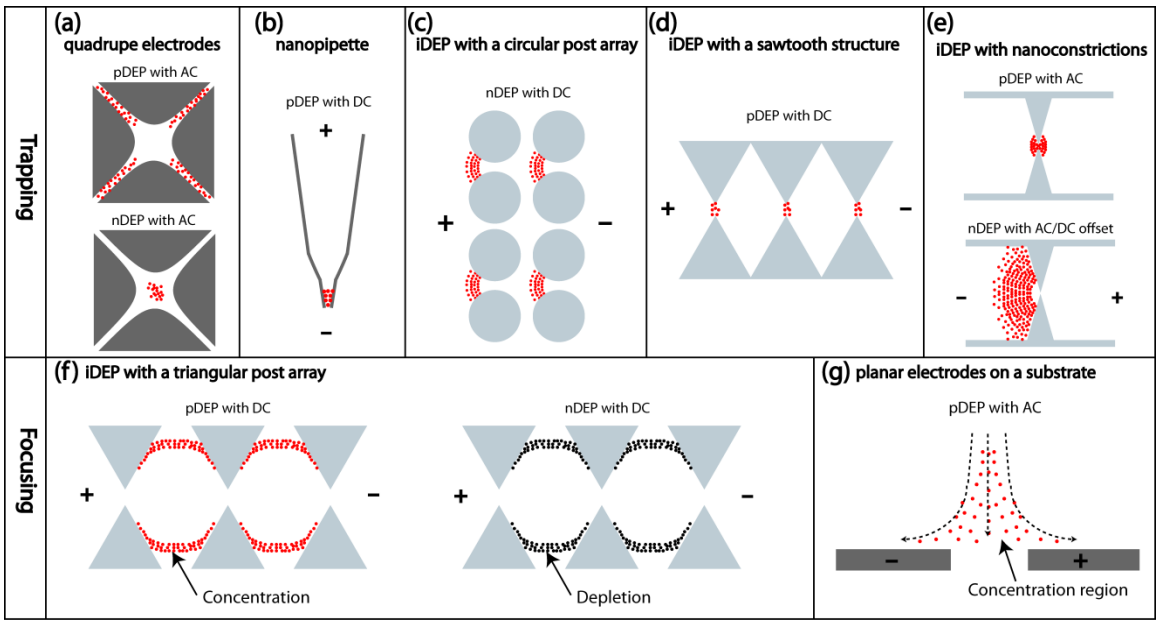

Figure 2-2. Schematic depiction of experimental devices used to study protein DEP. (a) Quadruple electrode geometries (Bakewell et al., 1998; Zheng et al., 2004) to manipulate proteins under AC conditions. Proteins are trapped due to positive DEP (top image) between the electrodes where the electric field gradient is high or negative DEP at the low electric field gradient regions (bottom image). (b) A schematic image of a nanopipette (Clarke et al., 2007; Clarke, White, Zhou, Ying, & Klenerman, 2005): When a negative voltage is applied to the bath electrode, negatively charged protein G is moved electrophoretically into the opposite direction of positive DEP. Thus, DEP force and electrophoretic force are balanced and proteins are trapped at the nanopipette tip. (c) A circular insulating post array (Lapizco-Encinas et al., 2008a). Under DC conditions, the protein BSA is repelled from the constrictions where the electric field gradient is highest, indicating negative DEP. (d) Insulating constrictions with varying sawtooth shapes realized by Staton et al. (Staton et al., 2012). With the application of DC voltage, Aβ fibrils are trapped at the narrow constrictions by positive DEP. (e) A nano-constriction insulating device (Liao et al., 2011, 2012; Liao & Chou, 2012). Under AC conditions at a frequency of 100 kHz, the protein streptavidin is trapped due to positive DEP (top image). With the application of an appropriate AC voltage as well as a DC bias, proteins are accumulated continuously due to negative DEP (bottom image). (f) A triangular insulating post array (Nakano, Camacho-Alanis, Chao, & Ros, 2012; Nakano et al., 2011). With the application of a DC voltage, IgG is focused in streamlines between the posts due to positive DEP (left image). Note that the flow direction is from left to right. By using tri-block copolymer F108 above the critical micelle concentration, IgG is encapsulated within micelles, resulting in protein-depleted streamlines due to negative DEP (right image). (g). Protein DEP focusing (streaming) used for a label-free protein detection sensor exhibiting high sensitivity (Gong, 2010).

PRIOR WORK IN PROTEIN DIELECTROPHORESIS WITH MICROFLUIDIC DEVICES

Around 20 groups have investigated protein DEP experimentally. To provide an overview, the reported work is first classified into two categories, trapping and focusing, and gives a short overview of them. This classification is used since these categories are different in terms of force balances, thus one can utilize either of them for DEP protein manipulation depending on the intended purpose. Finally, some examples of applications are presented pertaining to protein DEP trapping and focusing. *Figure 2-2* schematically depicts the representative device geometries discussed below and Table 2-1and Table 2-2 lists both experimental DEP studies as well as applications.

Trapping. Trapping is defined as electric field-induced particle immobilization at certain regions in a microstructured device. This occurs when the DEP force overcomes other competing forces such as the electrokinetic force, electrothermal force, hydrodynamic force, and Brownian motion. Washizu et al. demonstrated the first molecular DEP studies using four proteins: avidin, concanavalin, chymotrypsinogen, and ribonuclease A. Using a field integrated circuit with a frequency up to 1 MHz, accumulation of proteins started with an applied voltage of 15 V, which is attributed to positive molecular DEP (Washizu et al., 1994). In contrast, Bakewell et al. demonstrated both positive and negative DEP of the same protein avidin using quadruple electrode geometries schematically shown in *Figure 2-2*a (Bakewell et al., 1998). A crossover frequency of 9 MHz was experimentally determined. Bakewell et al. concluded that positive DEP occurs at frequencies below 9 MHz, while negative DEP prevails in a frequency range between 9 MHz and 20 MHz (Bakewell et al., 1998). Using similar

quadruple electrode geometries, Zheng et al. reported DEP trapping of bovine serum albumin (BSA). The eDEP device was employed to position BSA between the electrode gap in order to measure protein conductance (Zheng et al., 2004). Hölzel et al. used different electrode geometries, namely pairs of microelectrodes as close as 500 nm (Hölzel et al., 2005). The expected value of $\nabla \boldsymbol{E}^2$ reaches 10^{21} V^2/m^3 with which single R-phycoerythrin molecules would experience a DEP force of 0.1 pN according to their model. The theoretical calculations suggested that the DEP force overcomes diffusion. It was further shown experimentally that R-phycoerythrin was successfully trapped due to positive DEP at the tip of the electrodes with an applied voltage of 10 V and a frequency of 0.1 ~5 MHz (Hölzel et al., 2005).

Another iDEP approach can be performed by employing a nanopipette used by Clarke et al. to demonstrate the trapping of two proteins, protein G and immunoglobulin G (IgG) (Clarke et al., 2005), as schematically depicted in *Figure 2-2*b (Clarke et al., 2005). The tip of this nanopipette has a 100 ~ 150 nm internal diameter creating an electric field strength of 10^6 V/m. Using a physiological buffer to retain protein integrity, a maximum of 3000-fold protein concentration was achieved due to positive DEP with reversible protein accumulation (Clarke et al., 2005). Moreover, the same device was used to measure protein conductivity (Clarke et al., 2007).

Furthermore, Lapizco-Encinas et al. reported protein trapping using an iDEP device, as schematically shown in *Figure 2-2*c (Lapizco-Encinas et al., 2008a). The authors showed that BSA could be manipulated via negative DEP under DC condition within a microfluidic device containing insulating circular post arrays. The DEP response was systematically studied by varying the buffer conductivity (25 ~ 100 μS/cm) and pH

(8 and 9) with an applied voltage of 700 ~ 1600 V/cm. The maximum protein concentration in the trapping region was observed using the highest conductivity buffer (100 µS/cm, pH 8) (Lapizco-Encinas et al., 2008a). In addition, Staton et al. fabricated insulating constrictions in a single microfluidic channel with varying sawtooth shape to construct an iDEP system (see *Figure 2-2*d) (Staton et al., 2012). They employed this device to study iDEP of amyloid-beta (Aβ) fibrils which play an important role in Alzheimer disease pathogenesis. With a DC-iDEP device they showed rapid and selective concentration of the Aβ species. While Aβ monomers exhibited streaming DEP, Aβ fibrils were captured and concentrated at the narrow constriction of the sawtooth structure demonstrating iDEP trapping (Staton et al., 2012).

Most recently Liao et al. reported iDEP devices with nanometer-sized constrictions fabricated by a combination of photo- and electron beam lithography as depicted in *Figure 2-2*e (Liao & Chou, 2012) and further employed in the following work (Liao et al., 2011, 2012). Numerical simulations suggested that with a 100 nm constriction device the DEP force acting on a streptavidin molecule reaches 10^{-10} ~ 10^{-11} N, whereas less than 10 pN DEP force is generated with 1 µm constrictions (Liao et al., 2011). They used a physiological buffer to maintain the protein's conformation and functionality, which poses a challenge due to significant Joule heating. However, using a 30 nm nano-constriction device at 200 ~ 300 V_{pp}/cm AC voltage and 1 MHz frequency combined with a slight DC offset, concentration of the protein streptavidin was resulted due to negative DEP at regions of low electric field strength. The authors specifically selected a frequency range for negative DEP so that the protein would be trapped at the low electric field regions where a rise in temperature is less

significant. With this well-designed device, they achieved a > 10^5-fold concentration increase within 20 seconds (Liao & Chou, 2012).

Focusing. Unlike trapping, focused particles are not immobilized but flow as narrow or confined streams. To focus particles DEP has to overcome Brownian diffusion, whereas other bulk fluid flows such as electroosmosis overpower DEP. There are only a few groups that have investigated DEP focusing for proteins. DEP focusing can – despite the large bulk flow component – be employed as an analytical tool. For example, it has been shown that DEP focusing can be successfully employed to separate or sort cells and colloidal particles (K. H. Kang, Kang, Xuan, & Li, 2006; Y. Kang, Li, Kalams, & Eid, 2008). Moreover, DEP focusing has been demonstrated with nanoparticles by Cummings and Singh (Cummings & Singh, 2003) and was applied to sub-micrometer bead sorting (B. Abdallah, Chao, Fromme, & Ros, 2012). It is thus expected that protein DEP focusing will be important for analytical applications as well as a general tool to investigate protein DEP. Our work presented herein is classified into this category of protein focusing with which the protein DEP behavior was tested using various proteins.

A computational study on the DEP streaming behavior of myoglobin was presented by Gunda et al. (Gunda & Mitra, 2010). A detailed study on the electric field distribution along an electrode-based device was provided as well as the concentration distribution of myoglobin with a convection-diffusion model. The underlying protein DEP response was modeled for different shapes, such as ellipsoids as well as a sphere according to classical DEP theory, demonstrating that DEP forces overcome Brownian forces in the presented device geometry and computed electric fields. Furthermore, an electrode-based DEP device for protein streaming has been employed by Gong (Gong,

2010). This is an excellent application of streaming DEP and used in nanoelectronic devices for label-free, sensitive protein detection. This work is further detailed in the next section on applications.

Applications. This section presents detailed applications utilizing DEP to manipulate proteins. There are three main applications in the past: separation, molecular patterning and bioprobes, and biosensors.

***Separations*.** For a successful separation of protein mixtures, forces acting on each species have to be significantly different. DEP has the potential to be applied as a separation method since DEP forces greatly depend on polarizability. Even though the theoretical framework detailing the mechanism of protein polarization and dielectrophoretic response has not been investigated for a large variety of proteins yet, current knowledge suggests a wide variety in DEP response including the occurrence of positive and negative DEP. Exploiting protein DEP has the advantage to probe a frequency dependent quantity rendering the separation process 'tunable'. However, not only the frequency can be used to tailor DEP response, but also the magnitude of $\nabla \boldsymbol{E}^2$. Microfabricated devices (either employing electrodes or using the iDEP approach) allow spatial tuning of the forces molecules experience within a separation experiment, for example along a separation channel. This can be exploited advantageously to improve resolution. Moreover, DEP response can be used as an enrichment or trapping approach prior to separation, in which particles with similar DEP properties can first be enriched before a higher resolution separation follows. This approach would also be useful for situations with low sample concentrations, such as is the case for many biomarkers.

Finally, sorting or fractionation approaches are also achievable with DEP as has been demonstrated with particles and cells (X.-B. Wang et al., 2000).

Washizu et al. first demonstrated the potential use of DEP for protein separation employing the technique named "DEP chromatography" (Kawabata & Washizu, 2001; Washizu et al., 1994). In their device a pair of interdigitated electrodes is mounted on a substrate and the sample mixtures are driven into the device from the inlet at a constant flow velocity. Due to an electric field gradient created by the integrated electrodes, species experiencing larger DEP force retard from others. Therefore these species exhibit a longer elution time as detected by changes in fluorescence intensity at the outlet. Using this device Washizu et al. performed DEP experiments with DNA ranging from 9 ~ 48 kbp and found that 48 kbp was separated from the others. Next, they conducted a similar experiment with the protein avidin at 1 kHz and could show that the protein was trapped upon application of voltage (Washizu et al., 1994). Furthermore, Kawabata et al. used a similar DEP chromatography device to extend Washizu's study to a larger variety of proteins and DNAs including insulin, BSA, and Immunoglobulin M (Kawabata & Washizu, 2001). Even though no actual separation of the protein mixtures was performed in these two studies, they both showed that more polarizable and/or larger particles are trapped more efficiently by a DEP chromatography device. This work indicates that the development of a protein separation assay should be possible with careful device design and choice of proteins.

Molecular Patterning and Bioprobes. DEP has been used to investigate the motility of biological motor systems in the field of microelectronics where molecular motor systems, such as the kinesin/microtubule system and actin/myosin system which

have attracted much interest due to their possible uses as microsensors and actuators (Heuvel & Dekker, 2007). Biological motor proteins as well as associated cytoskeletal motor proteins are responsible for a variety of cellular processes and functionalities including muscle contraction and segregation of chromosomes during cell division. Therefore, it is essential to understand and control the molecular motor-based motility as well as to investigate these interactions within a biological system. Asokan et al. applied DEP forces to pattern actin on a substrate using quadruple electrodes in order to investigate actin motility (Asokan et al., 2003). Upon the application of 7 V_{pp} AC voltage in a frequency range of 100 kHz ~ 30 MHz, they observed positive DEP and DEP orientation torques, resulting in an alignment of actin parallel to electric field lines. Additionally, the numerical simulations revealed the maximum $\nabla \boldsymbol{E}^2$ of 10^{20} V^2/m^3 which created DEP forces of ~ 0.4 pN (Asokan et al., 2003).

In another application, Uppalapati et al. fabricated microelectrodes on glass substrates (Uppalapati, Huang, Jackson, & Hancock, 2008). In a low ionic strength buffer, bundles of microtubules were collected and oriented by the application of AC voltages. The combination of DEP forces, AC electroosmosis, and electrothermal forces controls particle motion in this device. By tuning the buffer conductivity and AC frequency, the apparent conductivity of taxol-stabilized microtubules was found to be 250 mS/m. Using this particle conductivity value the maximum DEP force per unit length of microtubules was found to be 10 pN/μm at a frequency of 5 MHz (Uppalapati et al., 2008).

DEP has also been applied in order to develop carbon nanotube (CNT) bioprobes used as a force measurement probe in atomic force microscopy (AFM) by Maruyama et

al. (Maruyama & Nakayama, 2008). CNT bioprobes could be used to investigate protein dynamics by enabling site-specific and rotational specific force measurements. Under AC DEP conditions streptavidin-quantum dot conjugates as well as streptavidin molecules were covalently attached mainly to the tip of the CNTs due to positive DEP and effectively reduced the protein attachment on the sidewall (Maruyama & Nakayama, 2008).

***Biosensors*.** DEP was also used to develop a label-free detection device for biomarkers with high sensitivity. Gong demonstrated a label-free attomolar detection system for prostate-specific antigen (PSA) which is considered a biomarker for prostate cancer. Gong integrated silicon nanowire field-effect transistors and planar electrodes on a sensor substrate (Gong, 2010). The nanowire surface was functionalized with PSA antibodies serving as receptors. In order to increase the sensor sensitivity, AC DEP was utilized: AC electroosmosis drives proteins to the receptors, and moreover proteins are pre-concentrated in the vicinity of receptors due to positive DEP. This transport mechanism is considered DEP streaming where a DEP component caused by AC excitation overlays with a convective electroosmotic flow (Gong, 2010). The pathogen binding events to the antibodies are detected by AC conductance. It was shown that the sensitivity of the nanowire device increased 10^4-fold when compared to the mere diffusion controlled device. The lowest PSA concentration detected by the nanowire device was found to be 10 aM under the application of 0.5 V AC and a frequency of 47 Hz (Gong, 2010). Another example for sensing probes was demonstrated with the detection of viruses with very high sensitivity (de la Rica, Mendoza, Lechuga, & Matsui, 2008). De la Rica et al. developed a peptide-nanotube sensor platform on which peptide

nanotubes are aligned between the Au electrodes due to positive DEP at 10 Hz frequency and 5 V_{pp}. The surface of the peptide nanotubes was coated with antibodies specifically binding to a target pathogen, thus the target pathogens are selectively captured on the nanotube surface. Virus binding events on the nanotubes were detected by an AC capacitance change between the electrodes. This peptide-nanotube based sensor successfully detected a label-free herpes simplex virus type 2 (HSV-2) within 1 hour with a concentration as low as 10^2 plaque forming units per ml (pfu/mL) which corresponds to the number of infective virus particles (de la Rica et al., 2008).

Castillo et al. also studied self-assembled amyloid peptide nanotubes (SAPNT) employing DEP (Castillo, Tanzi, Dimaki, & Svendsen, 2008). SAPNT is known for excellent thermal and chemical stability as well as high mechanical strength, which can be used for nanotechnological applications such as biosensors and field effect transistors. In this study, bundles or a single SAPNT were successfully manipulated and deposited on top of the micro Au electrodes due to positive DEP with an application of 10 V_{pp} and a frequency of 1 MHz. In addition, the electrical properties of the nanotubes were studied by plotting I-V curves, which confirmed a low ohmic conductivity of SAPNT under applied potential (Castillo et al., 2008).

Table 2-1

Fundamental studies of peptide and protein DEP.

	Type of DEP	Devices	References	Proteins used
		Fundamental Studies		
Trapping	Electrode EDP	Interdigitated electrodes	(Washizu et al., 1994)	Avidin, concanavalin, chymotrypsinogen and ribonuclease A
		Multipole electrodes	(Bakewell et al., 1998) (Zheng et al., 2004) (Asokan et al., 2003)	Avidin BSA Actin
		Nanopipette	(Clarke et al., 2007, 2005)	Yellow fluorescence protein Protein G IgG
		Planar electrodes	(Hölzel et al., 2005), (Castillo et al., 2008) (Uppalapati et al., 2008)	R-phycoerythrin Amyloid peptide nanotubes Microtubules
		Others	(Maruyama & Nakayama, 2008) (Kawabata & Washizu, 2001) (Hübner, Hoettges, McDonnell, Carter, & Hughes, 2007)	Streptavidin Insulin, BSA, and IgM Albumin
	Insulator-based DEP	Nanoconstrictions	(Liao et al., 2011, 2012; Liao & Chou, 2012)	Streptavidin
		Post arrays	(Lapizco-Encinas et al., 2008a)	BSA
		Sawtooth	(Staton et al., 2012)	Aβ amyloid
Focusing	Electrode DEP	Planar electrodes	(Gong, 2010)	Prostate-specific antigen (PSA)
	Insulator -based DEP	Post arrays	(Nakano et al., 2012, 2011)	IgG, BSA
		Nanostructures	(Camacho-Alanis et al., 2012)	BSA

Table 2-2

Applications of peptide and protein DEP.

Applications				
Separations	Electrode DEP	Interdigitated electrodes	(Washizu et al., 1994)	Avidin
		Electrode arrays	(Kawabata & Washizu, 2001)	Insulin, BSA, and IgM
Molecular patterning	Electrode DEP	Planar electrodes	(Washizu et al., 1994)	Avidin
		Multipole electrodes	(Asokan et al., 2003)	Actin
Bioprobes		Carbon nanotube (CNT) tip	(Maruyama & Nakayama, 2008)	Streptavidin
Biosensors	Electrode DEP	Planar electrodes	(Gong, 2010) (de la Rica et al., 2008) (Castillo et al., 2008)	PSA Peptide nanotubes Amyloid peptide nanotubes

CHAPTER 3

NUMERICAL MODELING

CONVECTION-DIFFUSION EQUATION TO MODEL CONCENTRATION DISTRIBUTION

The anticipated DEP forces acting on biomolecules, i.e. proteins in our case represent an important aspect in iDEP devices. Little is known on the mechanisms involved in protein DEP up to date and a detailed model is lacking. Therefore, involved trapping forces are related to well-studied theories for solid particles, enabling the estimation of the anticipated trapping forces in accordance with micro- and nanoparticles. The DEP forces for different shapes of particle have been studied previously and a prolate ellipsoid model was employed for IgG and an oblate ellipsoid model for β-galactosidase. Clarke et al. (Clarke et al., 2007) previously related the trapping forces for protein DEP to a prolate ellipsoid model, assuming an overall prolate ellipsoid shape of proteins in solution. This seems reasonable in my case considering reported shape of IgG molecules in solution (Sandin, Öfverstedt, Wikström, Wrange, & Skoglund, 2004). For β-galactosidase, an oblate ellipsoid shape is assumed based on its dimension from x-ray crystallography data (Jacobson, Zhang, DuBose, & Matthews, 1994). In the case of DC DEP, the DEP force acting on an ellipsoid particle is given as (Clarke et al., 2007; Morgan & Green, 1997):

$$\boldsymbol{F} = \frac{4}{3}\pi abc\varepsilon_m \left(\frac{\sigma_p - \sigma_m}{Z\sigma_p + (1-Z)\sigma_m}\right)\nabla \boldsymbol{E^2} \qquad (3.\ 1)$$

where a, b, and c are the radii of the ellipsoid along x, y, and z axes, ε_m is the medium, i.e. surrounding buffer, permittivity, $\boldsymbol{E}$ the electric field and σ_m and σ_p the medium and

particle conductivity, respectively. *Z* indicates the geometrical polarization relaxation factor. The shape dependent factor *Z* is given in Appendix A 1 for a prolate ellipsoid and oblate ellipsoid case.

The expression $$f_{MCM} = \frac{\sigma_p - \sigma_m}{Z\sigma_p + (1-Z)\sigma_m} \quad (3.\ 2)$$

denotes the modified Clausius–Mossotti factor arising as a result of the ellipsoid model. The magnitude and sign of f_{MCM} governs the DEP behavior and is responsible for DEP migration either to the regions of high field gradients (positive DEP) or away from these regions (negative DEP).

Furthermore, considering convection due to electrokinetic forces, an electrokinetic velocity can be assigned as:

$$\boldsymbol{u_{ek}} = \mu_{ek}\boldsymbol{E} = \left(\mu_{eo} - \mu_{ep}\right)\boldsymbol{E} = \boldsymbol{u_{eo}} + \boldsymbol{u_{ep}} \quad (3.\ 3)$$

where μ_{eo} and μ_{ep} are the electroosmotic and electrophoretic mobility, respectively. For the negatively charged species such as IgG and β-galactosidase at the employed pH of 8, electrophoretic transport of these proteins is in opposite direction to the electroosmotic bulk flow. Depending on the magnitude of μ_{ep} relative to μ_{eo} this could considerable decrease the overall electrokinetic force or result in an overall reversed migration direction (for $\mu_{ep} > \mu_{eo}$ and in the case of opposite sign). In my study, μ_{ep} is considerably smaller than μ_{eo} and of opposite sign because the experimental observations reflected a strong cathodic electroosmotic flow, confirming that electrophoresis counteracts electroosmosis only to a marginal extent. Therefore, our simulations were conducted using an overall electrokinetic mobility reflecting the actual flow direction. Thus, μ_{eo} =

1.5×10^{-8} m^2/V s is used as previously reported under similar experimental conditions in PDMS microfluidic channels (Hellmich et al., 2005).

Similar to the case of electrokinesis, one can assign a DEP mobility μ_{dep} to a particle traveling in a liquid due to DEP. The DEP force is assumed to be balanced with the particle's drag force given by Probstein (Probstein, 2003):

$$\boldsymbol{F_{drag}} = 6\pi\eta\bar{R}\boldsymbol{u} \tag{3. 4}$$

where η is the medium viscosity, $\boldsymbol{u}$ is the particle velocity, and $\bar{R}$ is the mean translational coefficient (see Appendix A 1). Additionally the DEP velocity can be written as:

$$\boldsymbol{u_{dep}} = \mu_{dep}\nabla\boldsymbol{E}^2 \tag{3. 5}$$

By balancing equation (3. 1) and (3. 4), the expression of μ_{dep} is resulted as:

$$\mu_{dep} = \frac{2abc\varepsilon_m}{9\eta\bar{R}} f_{MCM} \tag{3. 6}$$

Similar to the early works on streaming DEP, a convection–diffusion model is employed to describe streaming DEP (Cummings, 2003; Lapizco-Encinas, Simmons, Cummings, & Fintschenko, 2004). I consider electroosmosis the convection component interplaying with diffusion and DEP. The total flux in our model can thus be expressed as:

$$\boldsymbol{J} = -D\nabla c + c\left(\boldsymbol{u_{ek}} + \boldsymbol{u_{dep}}\right) \tag{3. 7}$$

where D is the diffusion constant and c is the concentration of the particles. Any pressure drop across the microchannels is not accounted for and thus the non-electrokinetic component of velocity can be neglected in the *COMSOL* model. Equation (3. 7) is solved at steady state:

$$\frac{\partial c}{\partial t} = \nabla \cdot \boldsymbol{J} = 0 \tag{3. 8}$$

To solve this model, I used commercial software *COMSOL Multiphysics 4.4*. In particular, *electric currents physics* was first added to model the electric field distribution in the channel, whereas *creeping flow* was used to solve the electroosmotic component. Finally, to plot the concentration distributions using the convection-diffusion equation shown in equation (3. 7), *transport of diluted species* was employed with an initial concentration of unity.

Using equation (3. 1) allows predicting protein DEP behavior with the prolate elliptic radii chosen as previously reported for IgG (a = 5 nm, $b = c$ = 2.5 nm (Sandin et al., 2004)). An experimentally derived value for σ_p of proteins in solution was reported by Clarke et al. (Clarke et al., 2007) for yellow fluorescent protein. Thus this value was used for all calculations and a medium conductivity of 0.01 S/m adapted to the experimental conditions. The corresponding values are shown in Table 3-1. Based on these calculations, positive DEP is predicted for IgG according to a positive f_{MCM} value. It is important to note that these equations were deduced for a prolate ellipsoid particle. While it is a reasonable assumption, the actual polarization behavior of the considered proteins may deviate from these values. However, this model can used to reasonably estimate the involved trapping forces for such nanoscale objects. This is very useful for the design of iDEP devices and for the understanding of future DEP-based separation mechanisms. Chapter 5 will further show that this model is in excellent agreement with the experimental observations. Note, a negative DEP case for each geometry is purposefully defined by assigning a particle conductivity of zero. The differences in positive and negative DEP will be discussed in detail in Chapter 5 and 6 in relation to experimental results.

In the case of β-galactosidase, its dimension can be estimated as an oblate ellipsoid of 4.5 × 4.5 × 8 nm from x-ray crystallography data (Jacobson et al., 1994). Based on the experimental results of which the position of protein concentration indicates negative DEP (see discussion in Chapter 6), parameters needed for numerical simulations can be determined using equation (3. 6). As shown in Table 3-1, an extreme negative DEP case was assumed, thus σ_p = 0 S/m was employed.

Table 3-1

Input values used for numerical simulations.

Protein	σ_p **[S/m]**	σ_m **[S/m]**	f_{MCM}	**DEP type**	μ_{DEP} [c] **[m^4/V^2s]**	D **[m^2/s]**	α **[F/m^2]**
IgG	24.6 [a]	0.01	5.75	Positive	$8.60*10^{-24}$	$3.89*10^{-11}$ [d]	$5.34*10^{-34}$
β-galactosidase	0 [b]	0.01	-1.34	Negative	$-8.95*10^{-24}$	$3.2*10^{-11}$ [e]	$-1.15*10^{-33}$

[a] Experimentally derived value σ_p of proteins reported for yellow fluorescent protein (Clarke et al., 2007).
[b] Extreme negative DEP case is assumed with σ_p = 0 S/cm.
[c] Calculated using equation (3. 6) and values corresponding to IgG.
[d] From reference (Rosenqvist, Jøssang, Feder, & Harbitz, 1986).
[e] Calculated using Stokes-Einstein equation.

TEMPERATURE DISTRIBUTION IN A MICROFLUIDIC CHANNEL

To elucidate the Joule heating effect in the iDEP device, a numerical model was developed using commercial simulation software *COMSOL Multiphysics 4.4* (MA, USA). Both the fluid in the channel and the solid phase surrounding the channel in the numerical model were considered and solved for the electric current, flow field, and temperature field in 3D. First, the electric field distribution was simulated by applying the same potentials used in experiments (100 V, 1000 V, and 3000 V for a 1 cm long channel between the inlet and outlet) for each buffer conductivity (100 µS/cm and 1 mS/cm). All other channel walls were defined as electrically insulating.

A buffer of pH 8 is assumed to match with the experimental conditions with which negatively charged PDMS and glass walls create bulk electroosmotic flow in cathodic direction. To simulate this flow field, the incompressive Navier-Stokes equation was solved along with the continuity equation. The electroosmotic mobility (μ_{eo}) was

applied as a boundary condition to the PDMS walls employing μ_{eo} of 1.5 × 10^{-8} m^2/V s for PDMS channels coated with F108 prior to temperature measurements (Hellmich et al., 2005).

The temperature field is created by Joule heating within the fluid in the channel and extended to the surrounding PDMS and glass walls. This Joule heating induced temperature field is governed by the energy equation expressed as (Bergman, Lavine, Incropera, & DeWitt, 2011a):

$$\rho c_P \left(\frac{\partial T}{\partial t} + \boldsymbol{u_B}\nabla T\right) = k_1 \nabla^2 T + Q \quad \textbf{(}3.\ 9)$$

where c_P and k_1 denote the specific heat and thermal conductivity of the buffer, respectively, and they are assumed to be independent of temperature. $\boldsymbol{u_B}$ is the bulk flow velocity, T is the temperature, and Q is the heat generated by Joule heating:

$$Q = \boldsymbol{J} \cdot \boldsymbol{E} \quad (3.\ 10)$$

where $\boldsymbol{E}$ is the electric field and $\boldsymbol{J}$ is the current density expressed as $\boldsymbol{J} = \lambda(T)\boldsymbol{E}$ of which $\lambda(T)$ is the temperature dependent buffer conductivity. In addition, heat conduction through the solid walls plays a significant role in resultant temperature distributions and thus needs to be considered. The heat transfer through the solid is expressed with the following equation (Bergman et al., 2011a):

$$\rho_s c_{Ps} \left(\frac{\partial T}{\partial t}\right) = k_s \nabla^2 T + Q \quad (3.\ 11)$$

where ρ_s , c_{Ps}, and k_s denote the density, specific heat, and thermal conductivity of the solid, respectively. Note that our iDEP device is fabricated with the combination of PDMS and glass whose thermal properties differ significantly. Therefore, different values of thermal properties were assigned for the top and side PDMS walls (k_s = 0.18 W/m·K,

c_{ps} = 1100 J/kg·K, p_s = 1030 kg/m^3) and the bottom glass wall (k_s = 1.4 W/m·K, c_{ps} = 835 J/kg·K, p_s = 2225 kg/m^3). Isothermal boundary conditions were assumed for the inlet and outlet reservoirs since the volume of the reservoirs is much larger than that of the channel, and therefore expect the resultant temperature changes in the reservoir to be negligible. For the outside surface of the channel, the natural convection heat transfer with surrounding air was assumed as boundary conditions, and a heat transfer coefficient (h) of 20 W/m^2 K was employed (Bergman, Lavine, Incropera, & DeWitt, 2011b). Upon performing the numerical modeling, the buffer viscosity, buffer electrical conductivity, and the buffer permittivity were treated as temperature dependent and were accounted for as expressed in the following (Haynes, 2012):

$$\mu(T) = 2.761 \times 10^{-6} exp\left({}^{1713}/_{T}\right) \quad (3.\ 12)$$

$$\lambda(T) = \lambda_0\{1 + 0.02(T - T_0)\} \quad (3.\ 13)$$

$$\varepsilon(T) = 305.7\exp\left({}^{-T}/_{219}\right) \quad (3.\ 14)$$

where λ_0 is the electrical conductivity of the buffer at room temperature.

Both steady-state and time-dependent temperature changes were simulated numerically. In the case of the steady-state simulation, all three physics were coupled by taking into account the aforementioned temperature dependent parameters in a 3D device. However, for time-dependent simulation, only the electric current and temperature field were solved with only accounting for the temperature dependency of the electrical conductivity. The electroosmotic velocity was entered in the *Heat transfer in solids* module as a bulk fluid flow velocity as indicated in equation (3. 9). Although this approach was chosen for the 3D time-dependent simulation due to the lack of

computation capability, the resultant temperature distribution was not affected by employing the simplified methodology.

CHAPTER 4

EXPERIMENTAL METHODS

In this chapter the device fabrication processes and the experimental procedures are described to perform iDEP experiments presented in Chapter 5 and 6. The iDEP devices used for experiments are categorized largely into two, micropost iDEP devices and nano-constriction iDEP devices, based on the dimensions of the constrictions and the corresponding techniques used to fabricate each device.

MATERIALS AND CHEMICALS

Si wafers (5 in.) were purchased from University Wafer. SU-8 2007 negative photoresist and developer were obtained from Microchem (Newton, MA, USA). (Tridecafluoro-1,1,2,2-tetrahydrooctyl)dimethylchlorosilane (TDTS), vinyl PDMS prepolymer, Pt calalyst (platinum divinyltetramethyldisiloxane), and hydrosilane prepolymer was purchased from Gelest Corp (Morrisville, PA, USA). Sylgard 184, composed of silicone elastomer base and curing agent for poly(dimethylsiloxane) (PDMS), was purchased from Dow Corning Corporation (Midland, MI, USA). Potassium phosphate monobasic, sodium phosphate dibasic, poly (ethylene glycol)-block-poly(propylene glycol)-block-poly(ethylene glycol) (F108), 3-[(3-Cholamidopropyl)dimethylammonio]-1-propanesulfonate (CHAPS), acetone, isopropanol, and a modulator (2,4,6,8-Tetramethyl-2,4,6,8-tetravinylcyclotetrasiloxane) were purchased from Sigma-Aldrich (St. Louis, MO, USA). Alexa Fluor 488 BSA and Alexa Fluor 488 chicken anti-rabbit IgG conjugates were obtained from Invitrogen (Carlsbad, CA, USA). Glass slides were obtained from Fisher Scientific, and Pt wire was

from Alfa Aesar (Ward Hill, MA, USA). Ultrapure water was supplied from a Synergy purification system (Millipore, USA).

DEVICE FABRICATION

To fabricate iDEP microfluidic devices with micropost arrays, a standard photolithographic technique (Duong et al., 2003) was employed to fabricate the inverted microstructure used as a master wafer for soft lithography. The fabrication steps are shown in *Figure 4-1*. In brief, SU-8 was spin coated on a Si wafer at a proper rpm to obtain a desired thickness of 10 µm (*Figure 4-1* Step 1), exposed under UV light through a chrome on soda-lime photomask (*Figure 4-1* step 2), and developed in SU-8 developing solution. After silanization of the wafer, the soft lithography step was performed by casting PDMS on the master wafer (*Figure 4-1* step 5), followed by curing in an oven for 4 h at 85 °C. Subsequently, the cured PDMS was peeled off from the wafer, and the 2 mm diameter reservoir holes were manually punched through the PDMS piece at both ends of a 1 cm long channel. The resultant PDMS piece and 0.15 mm thick glass slide were sonicated in isopropanol and DI water baths and blow-dried with nitrogen. In order to tightly seal the PDMS with the glass slide, both surfaces were activated by oxygen plasma cleaner (PDC-001 Harrick Plasma, Harrick, USA) for 1 min at the highest RF setting. A 5 mm thick PDMS slab with 5 mm diameter reservoir holes was pressed on the top of the device above the microchip reservoirs to enlarge the reservoirs and to hold the Pt wire electrode in position.

To fabricate a nano-constriction iDEP device, a combination of photolithography and focused ion beam milling (FIBM) was employed to fabricate an inverted Si master as

previously demonstrated (Camacho-Alanis et al., 2012). In short, a master relief of SU-8 photoresist was first patterned on a Si wafer using a standard photolithographic technique as described above. This wafer was coated with 20 nm Cr layer (*Figure 4-1* step 3) using Cressington 308R Evaporator (Ted Pella Inc. USA). Subsequently, FIBM was performed to mill nanoposts (*Figure 4-1* step 4) with Nova 200 (FEI Company, USA) between the tips of the triangular microposts. For β-galactosidase DEP experiments using a nano-constriction device, a composite of thin toluene-diluted *h*-PDMS layer supported by thick Sylgard184 PDMS was used as described previously (H. Kang, Lee, Park, & Lee, 2006) since mere Sylgard184 PDMS structure tends to cause roof and/or lateral collapse for shallow features (Odom, Love, Wolfe, Paul, & Whitesides, 2002) such as my device of 2 μm height. Moreover, *h*-PDMS prevents deformation of the relief surface, resulting in sharper edges (H.-W. Li, Muir, Fichet, & Huck, 2003; Odom et al., 2002). The resultant h-PDMS piece was assembled by following the same procedures used for iDEP devices with micropost arrays.

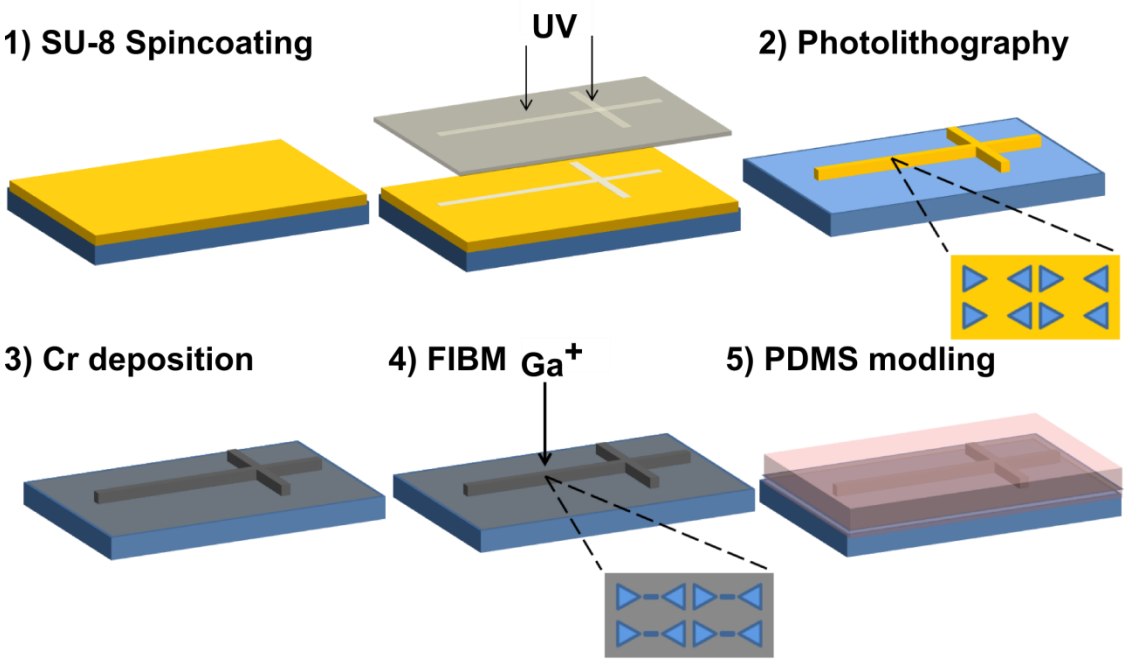

Figure 4-1. The fabrication process for iDEP microfluidic device where an array of topological posts are integrated in the channel. For a device with micropost arrays, only step 1, 2, and 5 are required. 1) SU-8 negative photoresist (yellow) is spin coated on a Si wafer (blue) to a thickness of 10 µm, followed by exposure to UV light through a chrome on soda-lime photomask (gray). 2) SU-8 removal with developing solution. 5) Casting PDMS on the master wafer to make a PDMS mold (pink). For a nano-constriction iDEP device, additional steps of 3 and 4 are performed. 3) Deposition of 20 nm chrome layer on a master wafer. 4) FIBM to mill the nanoposts between the tips of the triangular microposts.

EXPERIMENTAL SETUP

Prior to the experiment, the channel was coated for approximately 10 hours with 500 µM tri-block-copolymer F108 to reduce undesirable protein adsorption onto the PDMS surface. After the incubation in case of F108 static coating, F108 solution was washed three times and exchanged with the buffer used for the subsequent DEP experiment. On the other hand, channels operated under F108 dynamic coating conditions required no buffer exchange prior to DEP experiments. The experimental buffers were prepared with various conductivities and pHs including 32 µS/cm HEPES

buffer at pH 6.4, phosphate buffers with pH between 6.5 ~ 8 at conductivities from 100 μS/cm to 1 mS/cm, acetate-acetic acid buffer at pH 4, and tris-HCl at pH 9. All buffer pHs and conductivities were assessed with a pH meter (SB70P sympHony, VWR, USA) and conductivity meter (ORION 3 STAR, Thermo scientific, USA). For the subsequent DEP experiments the inlet reservoir was filled with the sample buffer containing analyte proteins and the other reservoir was filled with 80 μL working buffer. Pt electrodes attached to both reservoirs were connected to the high voltage power supply (HVS448 6000V, LabSmith, Livermore, CA) for DC iDEP experiments. To operate under AC conditions, electrodes were connected to a high voltage amplifier (AMT-3B20, 3000 V, Matsusada Precision, Inc.) to which an AC input was provided by a function generator (NI USB 6343, National Instruments, Columbus, OH). The AC signal generation was programmed using Labview version 2010 (National Instruments).

Three different proteins were tested with tailored iDEP devices, including immunoglobulin G (IgG) (Invitrogen, USA), bovine serum albumin (BSA) (Invitrogen, USA), and β-galactosidase (Sigma-Aldrich, USA) with the concentration of 45 nM, 7nM, and 33 nM, respectively. Prior to the experiments, proteins required labeling with fluorescence for visual detection. Alexa Fluor 488 labeled IgG was used as received from the supplier and β-galactosidase was labeled using an Alexa Fluor 488 protein labeling kit (Invitrogen, USA) following the basic protocol. Labeled proteins were purified using a suitable molecular weight cutoff centrifugal filter (EMD Millipore Corp., USA) with which the purity was tested using TLC. Recovered protein concentration was determined using Bradford protein assay with a plate reader spectrophotometer (Synergy HT, BioTek Instruments, VT).

DETECTION AND DATA ANALYSIS

For fluorescence microscopy imaging, an inverted microscope (IX 71, Olympus, Center Valley, PA, USA) with a 100x objective (LUCPlan FL N, Olympus, USA), a mercury burner (U-RFL-T, Olympus, USA), and fluorescent filter set (Olympus, USA) equipped with a 470/40 nm exciter, 495 nm dichroic, and 525/50 nm emitter was used. Images were acquired at a rate of 10 images per second using a CCD camera (Quantum 512 SC, Photometrics, Tucson, AZ, USA) and Micro-Manager software (University of California, San Francisco, CA, USA) and analyzed with Image J software (version 1.43).

A concentration factor, R, was calculated as: $R = (I_{SC} - I_{NS}) / (I_B - I_{PDMS})*100$. Here, I_{SC} denotes the fluorescence intensity at concentrated regions when voltage was applied for DEP to occur, while I_{NS} is the intensity at the non-streaming regions. I_B is the average fluorescence intensity with no applied voltage while no DEP streaming is observed. I_{PDMS} is the intensity of PDMS background aside from the channel. The depletion factor was calculated similarly except I_{SC} was substituted with I_{SD}, which denotes the fluorescence intensity at depleted streaming regions when negative DEP is observed. For both concentration and depletion factor calculations the intensities were calculated as the average of a defined number of pixels in each area and averaged over a total of 10 frames.

CHAPTER 5

PROTEIN DC INSULATOR BASED DIELECTROPHORESIS WITH MICROPOST ARRAYS

INTRODUCTION

Our study focuses on the manipulation of proteins by DEP to exploit its potential for bioanalytical applications. The potential of DEP arises from the manipulation of biomolecules in gel-free environment as well as rapid separation and pre-concentration capability. In DEP, electric field gradients evoke forces on polarizable objects leading to migration and/or trapping (Jones, 2005; Pohl, 1978). This technique thus contrasts electrophoresis, in which migration of charged species arises in a homogeneous electric field. Based on the dielectric properties of the analytes, a broad range of intrinsic characteristics, such as size, shape, charge, charge distribution and charge mobility, permittivity, and deformability can be probed with DEP (K. P. Chen, Pacheco, Hayes, & Staton, 2009). It thus provides a large parameter space which allows highly specific probing of analytes in complex samples.

For proteins the mechanism of polarization responsible for DEP transport is not well understood with much less experimental work that has been performed in the past. Theoretically, DEP manipulation of sub-micrometer sized proteins is challenging since extremely high electric field gradients are required in order to generate DEP forces large enough to compete with particle diffusion, electrokinesis, and electrothermal flow. Washizu et al. who performed the very first protein DEP estimated that the electric field of $10^6 \sim 10^7$ V/m is necessary for DEP manipulation of biomolecules of 1 ~ 5 nm in diameter (Washizu et al., 1994). Although this is just a rough estimation assuming the

$Re[f_{CM}] = 1$ using the conventional DEP theory given in equation (3. 1), it served as our starting point to design a suitable iDEP device with which protein manipulation can be realized.

In this chapter, iDEP geometries are optimized with the aid of numerical simulations which allow us to estimate the resultant electric field distributions, electric field gradients, and concentration profiles due to positive or negative DEP. Using the novel triangular and elliptical posts designs, our experimental results demonstrate streaming DEP under DC conditions using two different proteins, namely bovine serum albumin (BSA) and immunoglobulin G (IgG) molecules. In contrast to previous studies, the influence of protein aggregation is observed on DEP behavior and downscale the size of the post arrays to sizes smaller than 20 μm in an elastomeric platform. In addition a convection-diffusion model is developed that qualitatively captured this protein DEP streaming behavior in order to compare to our experimental observations. Even though DEP for IgG and BSA is not strong enough to completely trap these biomolecules, proteins were able to get concentrated along the streamlines in accordance with positive DEP, thus our study demonstrates that DEP is suitable to concentrate proteins in tailored microfluidic devices.

Additionally, with both the experimental microfluidic tool and the theoretical model at hand, our previous studies are extended to investigate factors influencing protein DEP. In particular, I study the influence of pH, surfactant concentration, and electrokinesis resulting both from electrophoretic and electroosmotic components as well as aggregation on DEP. To the best of our knowledge, this is the first detailed study on protein DEP streamline concentration in a microfluidic iDEP device. This study thus

points towards the potential of protein DEP for future analytical applications such as separation or pre-concentration.

DEVICE OPTIMIZATION WITH VARIOUS MICROPOST ARRAY GEOMETRIES

Figure 5-1 shows the schematic of one of our array geometries used to create iDEP devices. Arrays of insulating posts are integrated in a microfluidic channel to create non-uniform electric field around the post. I used a linear channel exhibiting such iDEP arrays and applied potential to it via electrodes immersed in the channel reservoirs located at both side of the channel. Three insulating post geometries were designed, which creates unique electric field gradient as shown in the scanning electron microscopy (SEM) images in *Figure 5-1*d-f. In the first device triangular post arrays were created in which strong gradients are expected between the tips of the triangles facing each other. A second and third device consisted of elliptical and circular post arrays with a symmetric distribution of electric field gradients. These structures were fabricated using standard photo- and soft lithographic techniques. The resulting PDMS molds for each geometry were verified by SEM and I thus adapted numerical simulations of protein DEP in these devices to the actual post dimensions.

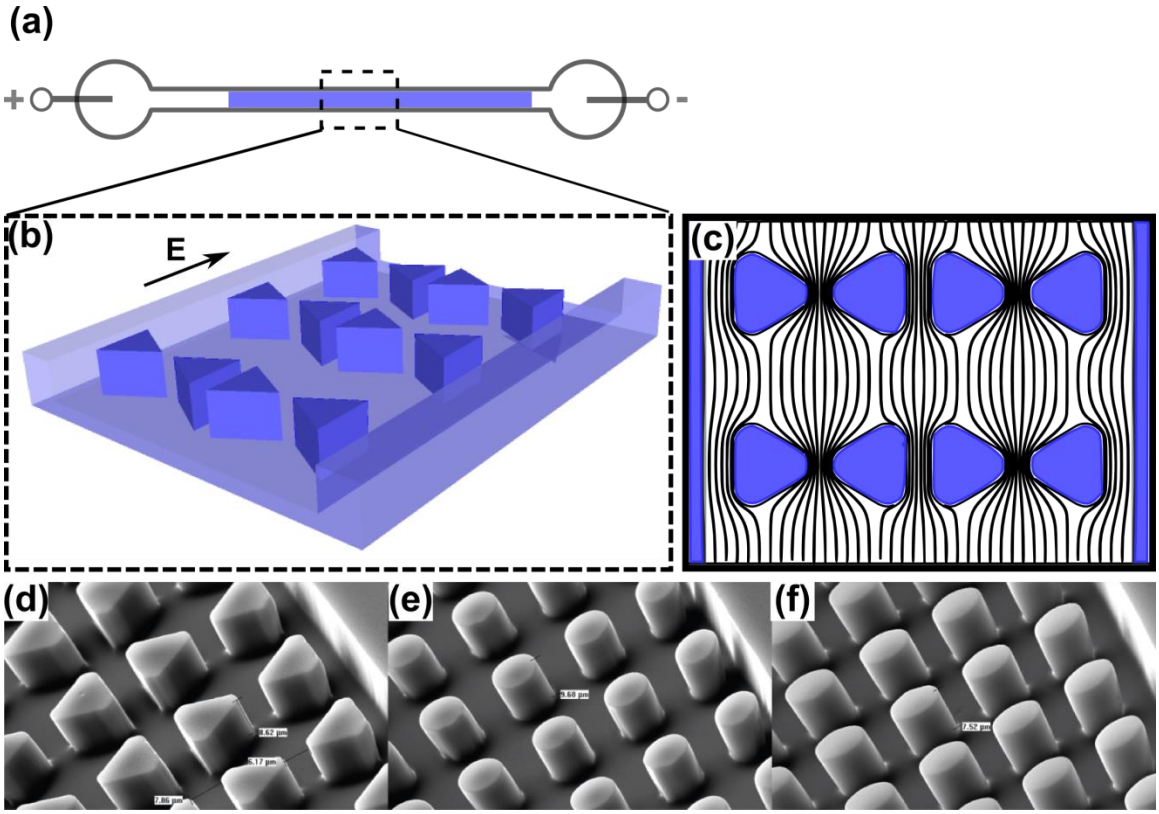

Figure 5-1. Schematic representation of insulating post arrays in the microfluidic device for iDEP protein manipulation and SEM images of different post geometries. (a) A straight iDEP channel with a DEP region indicated by blue. (b) The device contains periodic arrays of insulating topological posts which distort the electric field, thus creating non uniform electric fields. (c) A top view of the iDEP device, providing non-uniform electric field lines in the presence of insulating triangular posts. (d-f) SEM images of a PDMS mold with an array of (d) triangular posts, (e) circular posts, and (f) ellipsoidal posts.

I start the discussion on numerical simulations with each post array geometry. *Figure 5-2* demonstrates the electric field and $\nabla \boldsymbol{E}^2$ at an applied potential of 3000 V for a 1 cm channel for arrays of ellipsoidal, circular, and triangular posts. *Figure 5-2* depict the electric field (a-c) and $\nabla \boldsymbol{E}^2$ (d-f) at 3000 V/cm in these geometries. In the case of the ellipsoid and circular posts, the highest electric field and $\nabla \boldsymbol{E}^2$ are located at the vertical edges of the ellipse or circle, corresponding to values of 6.7×10^5 and 6.1×10^5 V/m and 4.1×10^{17} and 1.5×10^{17} V^2/m^3, respectively. However, that the highest electric field

(8.22×10^5 V/m) and strongest $\nabla \boldsymbol{E}^2$ values (4.25×10^{17} V^2/m^3) are obtained with the triangular post array. Additionally, the triangular post array creates the largest area of high electric field gradients. Therefore, the iDEP device with the triangular post array is expected to be most suited for manipulation of nanoscale objects such as proteins.

In the case of an array of triangular posts, the vertices facing each other are the areas with the highest electric field. Therefore, in the case of positive DEP proteins would be attracted toward the triangular tips facing each other. Our iDEP geometry is compared with previously reported streaming DEP for 200 nm latex spheres. In their contributions, Cummings et al. (Cummings & Singh, 2003; Cummings, 2003) demonstrate that streaming behavior and concentration occurs when DEP overcomes diffusion but is too weak to overcome the electrokinetic flow. These findings occurred using 200 nm particles which are larger in size than IgG and performed in different iDEP post geometries at applied electric fields of 80 ~ 250 V/cm (Cummings & Singh, 2003). In our case, the arising $\boldsymbol{u_{eo}}$ and $\boldsymbol{u_{dep}}$ can be estimated via the computed $\boldsymbol{E}$ and $\nabla \boldsymbol{E}^2$ values using equation (3. 3) and (3. 5), respectively. Thus the DEP force cannot overcome the electrokinetic flow. Therefore, DEP streaming behavior for proteins would be expected to be in accordance with previously reported data for nanoparticles (Cummings & Singh, 2003; Cummings, 2003). To test the assumed DEP behavior, the concentration profile were computed for particles exhibiting positive ($\mu_{dep} = 8.60 \times 10^{-24}$ m^4/V^2s) and negative ($\mu_{dep} = -7.14 \times 10^{-24}$ m^4/V^2s) using convection-diffusion equation shown in (3. 7). *Figure 5-3* provides the resultant concentration distribution for each post geometry. When DEP is positive (*Figure 5-3*a-c), the protein concentration was obtained along the posts, whereas the very same regions became depleted in the case of negative DEP

(*Figure 5-3*d-f). As expected from the magnitude of $\nabla \boldsymbol{E}^2$value resulted from each geometry, the most enhanced DEP effect was observed with the triangular post array with the maximum concentration of 7 % for positive DEP and depletion of 7 % for negative DEP. Note, that the concentration enhancement in the positive DEP case is more pronounced than the depletion in the negative DEP case. All the geometries therefore demonstrate highly distinct regions for DEP mode dependent enhancement (positive DEP) or depletion (negative DEP) that can be used to manipulate proteins within the microfluidic system. It is important to mention that potential electrolysis or Joule heating effects were not considered in our simulation. However, a separate study has been conducted to investigate the creation of pH gradients in iDEP experimentally as well as by numerical simulations (Gencoglu et al., 2011). This study showed that the pH changed toward the acidic range in time scales of ~ 10 mins under similar buffer conductivity and applied potentials. A lower pH (however pH above pKa of PDMS) can reduce the EOF in PDMS microchannels, thus resulting in increased overall contribution of DEP versus electroosmotic flow. As a consequence, protein concentration as a result of iDEP streaming can be enhanced. Indeed, our numerical simulation shows lower concentration factors as compared with our experiments (see the following section), indicating an overestimation of the electroosmotic component in simulations. Although Joule heating can, in principle, not be neglected in our case, little influence on protein DEP was found within the course of our experiments. Indeed temperature rise was found not to be too significant by temperature measurement experiments discussed thoroughly in Chapter 7.

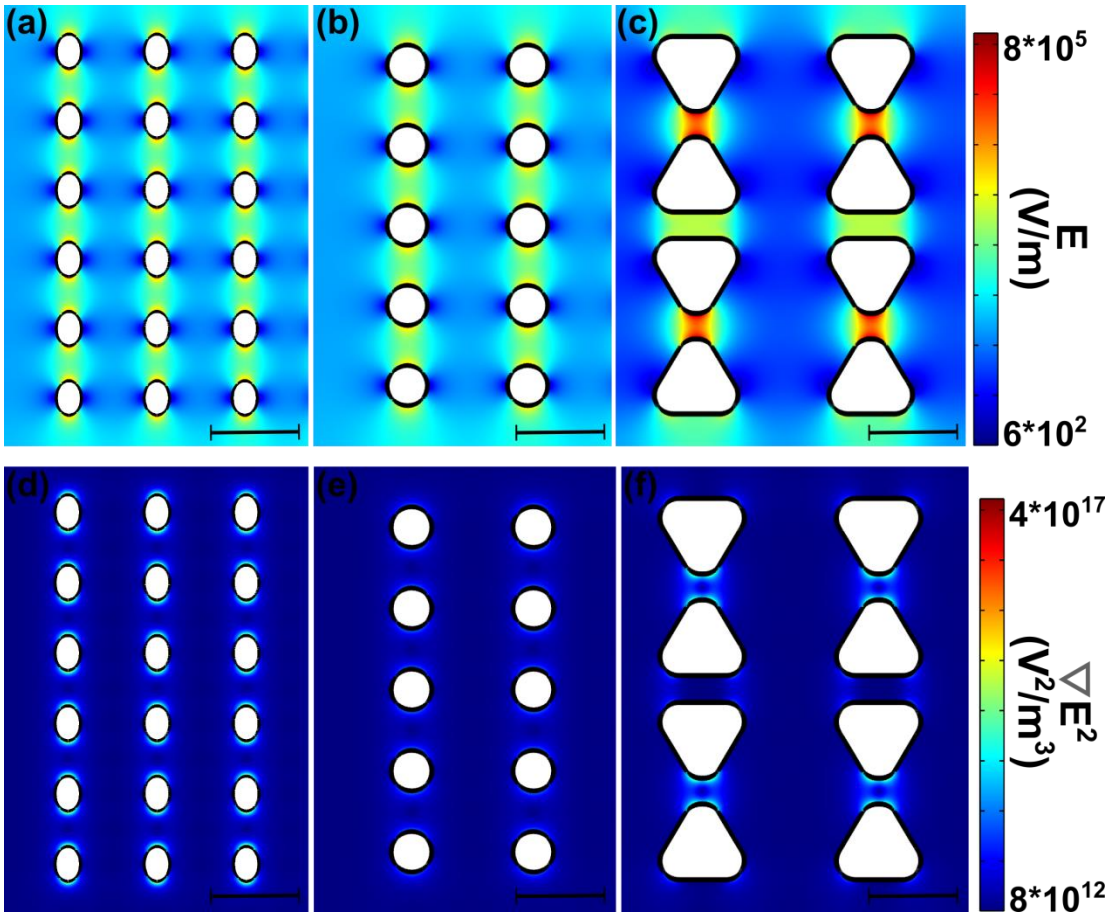

Figure 5-2. Simulation results providing the electric field and $\nabla \boldsymbol{E}^2$ distribution at 3000 V for a 1 cm channel within the iDEP channel with arrays of insulating posts of various geometries including ellipsoid, circle, and triangle. (a-c) shows the electric field distribution and (d-f) for $\nabla \boldsymbol{E}^2$. The scale bar is 20 μm.

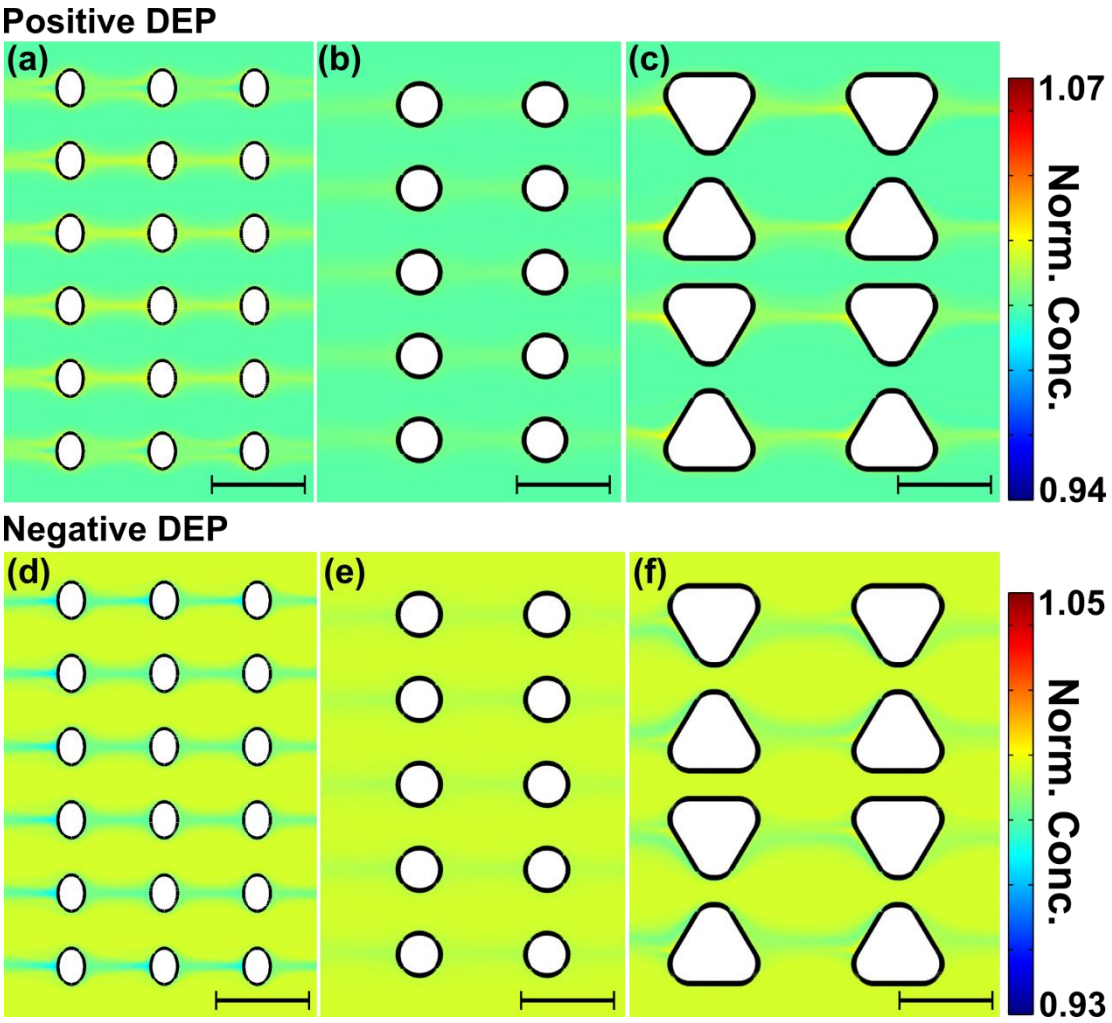

Figure 5-3. Simulation results demonstrating the concentration distribution considering DEP, electroosmosis, and particle diffusion at 3000 V for a 1 cm channel. (a-c) concentration profile considering positive DEP in which μ_{dep} is calculated for IgG. (d-f) concentration profile considering negative DEP. Normalized concentration is simulated with the initial concentration of unity. The scale bar represents 20 µm.

DIELECTROPHORETIC BEHAVIOR OF IMMUNOGLOBULIN G AND BOVINE SERUM ALBUMIN

Various iDEP post geometry designs were tested for protein manipulation experimentally. The triangular geometry was first employed to test DEP behavior of IgG. The protein solution was filled in the inlet reservoir and transported toward the post array at low applied potentials via cathodic electroosmotic flow. Upon an increase in the

electric potential, trapping of protein was observed within the device (see *Figure 5-4*a). This indicates that in the respective trapping areas the DEP component overcame the electrokinetic flow. This was a surprising finding as according to the simulations only streaming DEP was expected. However, once the electric field was turned off, proteins diffused away from the trapping positions as large, cohesive aggregates. Hence, I speculated that under these experimental conditions, large protein aggregates may form, and subsequently become trapped. This could be attributed by Joule heating within the microdevice at higher electric fields potentially leading to protein denaturation and subsequent aggregate formation. This trapping behavior can be explained by the much larger size of the aggregates compared with individual proteins and thus larger DEP forces as can be derived from equation (3. 1). To prevent aggregate formation, the zwitterionic detergent CHAPS was added to the buffer. CHAPS is known to improve protein solubility in bioanalytical applications (Hjelmeland, Nebert, & Osborne, 1983) and reduced aggregate formation was expected with this buffer additive. Owing to the zwitterionic nature of CHAPS, the overall conductivity of the buffer was not significantly changed. While the proteins may still be denatured due to Joule heating, CHAPS clearly prevented the formation of larger aggregates. More importantly, completely different behavior of IgG was observed in the channel upon electric field application. Our results indicated DEP streamline formation at 3000 V/cm as demonstrated in *Figure 5-4*b. Interestingly, these streamlines are formed at the same locations as in our simulation in the case of positive DEP (see *Figure 5-3*c). This positive DEP behavior of IgG is in agreement with the previously reported result by Clarke et al. where IgG is trapped via positive DEP at the tip of the nanopipette (Clarke et al., 2005). Our numerical model is

thus in excellent qualitative agreement with experimental findings when aggregate formation was prevented by the additive CHAPS. In addition, we observed a slight increase in fluorescence in the direction of the bulk flow (see *Figure 5-4*b). This was also observed in the simulations with the triangular posts (*Figure 5-3*c) indicating that the concentration effect could be intensified with extended rows of insulating structures.

This finding of protein aggregation was also applicable to the smaller protein BSA employing our iDEP device with an array of elliptic posts (Nakano et al., 2011). Similar to the case of IgG, trapping of larger entities suggested the formation of protein aggregates. This indicates that protein aggregation is not limited to IgG, but also occurs with other proteins. It is therefore possible that most iDEP manipulations of proteins may require the control of protein aggregation. Similar to the larger IgG proteins, streamline DEP was observed once the zwitterionic agent was added (Nakano et al., 2011). The concentration of BSA was increased along streamlines developing between the center edge positions of the periodically arranged ellipsoidal posts as simulated using the convection-diffusion model shown in *Figure 5-3*a in which positive DEP was assumed. Similar to the case of IgG, concentration enhancement was observed for the positive DEP simulation in accordance with the observed streamline behavior. I thus conclude that BSA also demonstrated positive DEP behavior as well as IgG under our experimental conditions.

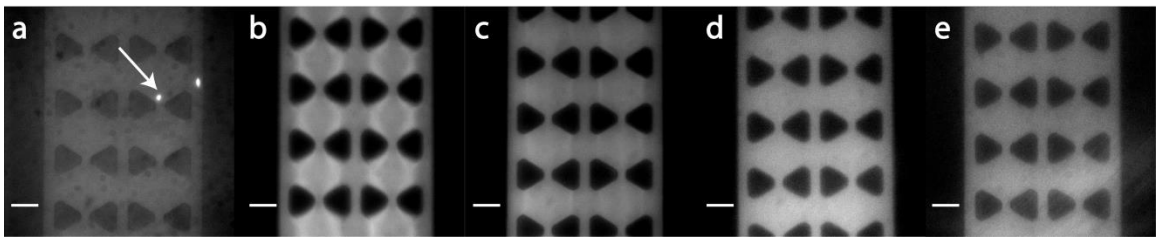

Figure 5-4. Fluorescence microscopy images of fluorescently labeled IgG obtained from iDEP experiments performed with pH 8 phosphate buffer. (a) IgG aggregate trapping observed without CHAPS additive as indicated by the white arrow. (b-e) Streaming DEP with an applied potential of 3000 V for a 1 cm channel in the presence of 1.7 mM CHAPS at a buffer conductivity of (b) 0.01 S/cm, (c) 0.02 S/cm, (d) 0.03 S/m, and (e) 0.04 S/cm. Flow is from top to bottom. The scale bars indicate 20 μm.

FACTORS INFLUENCING PROTEIN DIELECTROPHORESIS

Dependence on Buffer Conductivity. The influence of protein DEP was investigated in relation to the buffer conductivity as the change in buffer medium conductivity has influence on the calculated DEP force as shown in equation (3. 1). To this aim, we repeated the experiments with IgG in the presence of CHAPS, but varied the conductivity of the buffer between 0.01 and 0.04 S/m by changing the salt concentration. As demonstrated in *Figure 5-4*b-e, the intensity of the streamlines decreased with increasing buffer conductivity. This phenomenon was further investigated more quantitatively. *Figure 5-5*a shows the concentration factor determined at the streamline positions in relation to buffer conductivity. The highest concentration increase was achieved in the lowest conductivity case of 0.01 S/m. At an applied potential of 3000 V for a 1 cm long channel, this resulted in a concentration factor of 46 %. Interestingly, this corresponds to an order of magnitude higher concentration factor as compared with simulations. This is attributed to an overestimation of the electroosmotic component versus the electrophoretic migration of proteins in opposite direction. In fact when using

our numerical model and simulating the case of a reduced electroosmotic flow component higher concentration factors are found in accordance with experiments (data not shown). Furthermore, *Figure 5-5*a also shows that higher buffer conductivities resulted in an overall lower concentration factor down to 8% at 0.04 S/cm with the same applied potential. This behavior can be explained in the case of positive DEP from equation (3. 1). When increasing σ_m the f_{CMC} factor is reduced, thus leading to lower DEP forces. As a consequence, concentration of proteins in streaming iDEP declines. Overall, the data demonstrated successful iDEP streaming of IgG proteins resulting in enhanced concentration of proteins at defined areas in the iDEP device. Additionally, the DEP behavior of protein is greatly influenced by the formation of aggregates as demonstrated the DEP trapping of IgG aggregates in contrast to iDEP streaming of IgG when aggregate formation is circumvented by the use of a surfactant.

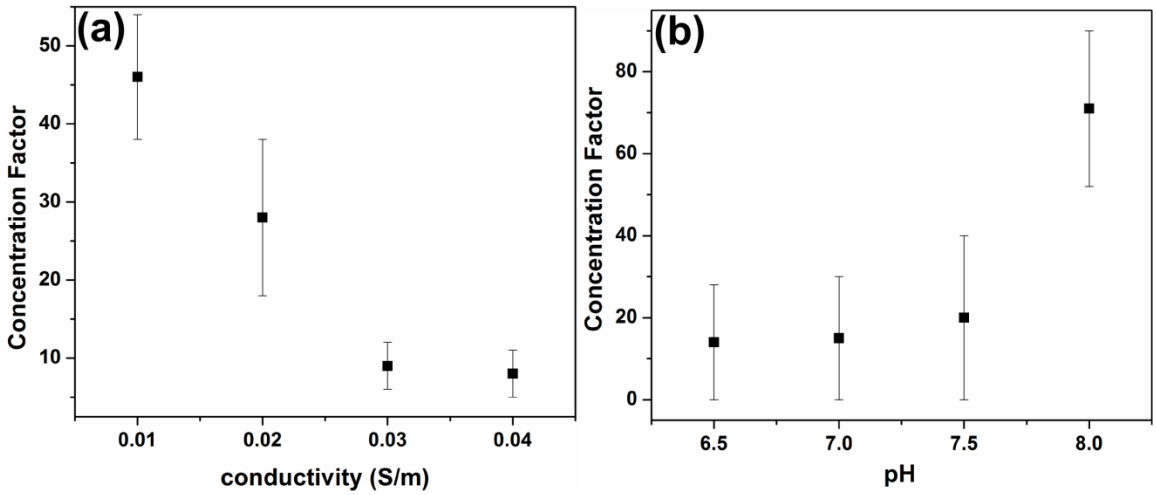

Figure 5-5.Normalized concentration factor as a function of conductivity and pH. (a) conductivity at 3000 V and (b) pH at 4200 V both for a 1 cm channel.

It is important to note that the experimental streamline behavior of IgG is in excellent qualitative agreement with the performed numerical simulations as indicated by

the match of streaming iDEP concentration enhancement. Quantitatively, however, I find a discrepancy in the absolute magnitude of the concentration factor. While concentration up to a factor of 46 % is observed in the case of IgG in the triangular post geometry, only a maximum value of 7 % is obtained from the simulation (*Figure 5-3*c). This can be attributed to differences of the input parameters used for the numerical simulations in comparison to our detailed experimental conditions. Clearly, the limitation arises due to the lack of the reported data on protein conductivity and thus our simulation input parameters were adapted to the data most relevant to IgG in solution as previously reported by Clarke et al. (Clarke et al., 2007). Additionally, other influences may arise from deviations of the actual electroosmotic mobility in the microchannels. Again, the simulation parameters were adapted to our previously reported data in coated PDMS channels (Hellmich et al., 2005). In this study, however deviating buffer conductivity and pH were used, possibly giving rise to changes in the absolute value of μ_{eo}. As found in our simulation, slightly reduced μ_{eo} can increase the streaming concentration considerably (see "influence of electroosmosis")

Dependence on Buffer pH the influence of pH on the DEP behavior of IgG was investigated within a pH range of 4 ~ 9 in the presence of the zwitterionic additive CHAPS. I started with pH 8 at a conductivity of 0.01 S/cm and as a result, high fluorescence intensity was observed in streamlines along the posts (*Figure 5-6*a) resembling positive DEP streaming as described in the previous section. Then additional DEP experiments were performed with other pH values, while keeping the buffer medium conductivity at 0.01 S/m. As a result, two main effects were found. First, protein aggregates started to form below pH 6.5 and above 8 regardless of the presence of

CHAPS (*Figure 5-6*e-f). Immediately after applying a voltage, large amounts of aggregates started to flow within the channel and hindered further experiments by clogging the channel and adsorption on the PDMS surface. Interestingly, the DEP behavior has changed from streaming to trapping – a strong indicator for larger particles resulting from aggregate formation. I conclude that at pH below 6.5 and above 8, aggregation is favored even in the presence of CHAPS. This is attributed to a pronounced degradation and conformational changes within the protein.

In contrast, in the pH range between 6.5 and 8, aggregate formation was not apparent and iDEP streaming according to positive DEP was observed. *Figure 5-6*a-d show streamlines resulting for pH 6.5 to pH 8, whereas the intensity profile at the midpoint line between the two rows of posts is plotted under each representative image. As clearly shown in *Figure 5-6*a-d, the protein concentration is enhanced with increasing buffer pH. This phenomenon was investigated more quantitatively by calculating the concentration factor. *Figure 5-5*b shows protein concentration factors with varying pH between 6.5 and 8. With an applied electric field of 4200 V/cm, the protein concentration is enhanced towards higher pH. The largest concentration factor of 71 % is obtained at pH 8 at 4200 V/cm.

The variation of the pH clearly demonstrates a working range for IgG DEP streaming. Both below pH 6.5 and above pH 8, aggregation hampers protein streaming. This is in contrary to recently published results of the Lapizco-Encinas group on DC iDEP of bovine serum albumin (Lapizco-Encinas et al., 2008a). While this group reports on protein particle trapping in a DC iDEP device at similar solution conductivities, note that electric fields and gradients thereof are much larger in our device. Comparing their

data (Lapizco-Encinas et al., 2008a) with ours (Nakano et al., 2011), I conclude that even at an order of magnitude higher electric fields and 2 ~ 3 order of magnitude larger $\nabla \boldsymbol{E}^2$ DC iDEP streaming is apparent, both theoretically and experimentally (this manuscript). This is remarkable, as a larger protein (150 kDa IgG compared to 60 kDa bovine serum albumin) was even employed (Lapizco-Encinas et al., 2008a)) from which a larger DEP force would be expected according to classical theory. I thus suspect that protein aggregation – barely resolvable in fluorescence microscopy studies – can enhance DEP forces leading to trapping at even lower electric fields. I furthermore find from calculations of the trapping criterion as developed previously (Baylon-Cardiel, Lapizco-Encinas, Reyes-Betanzo, Chávez-Santoscoy, & Martínez-Chapa, 2009a; R. V. Davalos et al., 2008; Kwon, Maeng, Chun, & Song, 2008a) that the trapping condition is not satisfied in either iDEP device (see Appendix B 1).

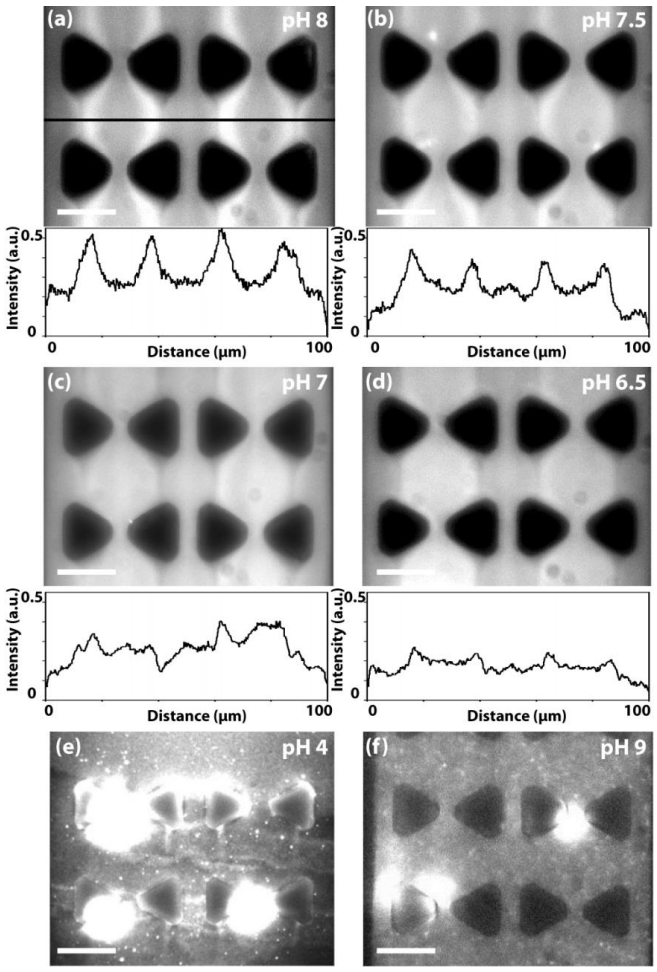

Figure 5-6. Fluorescence microcopy images of IgG streaming iDEP in an array of triangular posts. The scale bar indicates 20 μm and the flow direction is from top to bottom. Below each image is a profile intensity plot at the position marked in a) (black line). (a-d) Streamlines are observed due to positive DEP at an applied electric field of 4200 V/cm with pH buffer media in the range of pH 6.5 ~ 8: (a) pH 6.5, (b) pH 7, (c) pH 7.5, (d) pH 8. Positive DEP streaming is increased from (a) to (d) while increasing the medium pH results as an increase of the concentration. (e, f) Protein aggregates are formed regardless of the presence of CHAPS at (e) pH 4 and (f) pH 9.

It is interesting to note that the working pH range is relevant for diagnostic applications, in which circumneutral conditions are essential for affinity reactions of immunoglobulins with antigens. Although our experiments are carried out at low buffer conductivity, our work complements protein DEP studies under physiological conditions in nanometer-sized constriction devices, in which trapping was observed (Chaurey,

Polanco, Chou, & Swami, 2012; Liao & Chou, 2012). Thus, the resulting optimum pH range for iDEP as observed here is well suited for applications combining DEP manipulation with biological immunoassays. The concentration increase in the range of pH 6.5 ~ 8 additionally demonstrate that IgG streaming behavior is indeed influenced by pH. In the following section potential pH-dependent factors are thus investigated influencing iDEP migration such as electroosmosis and electrophoresis.

Influence of Electroosmosis. In order to understand the influence of the electroosmotic transport on DEP streaming variations of μ_{ek} (based on electrophoresis (EP) and electroosmotic flow (EOF)) were investigated. This is considered to be an important factor in protein streaming iDEP since strong electrokinetic transport counteracts DEP concentration. A reduction of the competing electrokinetic forces is therefore expected to result in a higher protein concentration effect. Therefore, the influence of the magnitude of EOF on IgG streaming DEP was studied by only considering an electroosmotic mobility, μ_{eo}, and its variations in our numerical model. Thus all variations in μ_{eo} correspond to changes in the overall μ_{ek}. *Figure 5-7*a-c depict the concentration profiles for IgG (with positive DEP) in dependence of μ_{eo}. A typical μ_{eo} of 1.5×10^{-8} m^2/Vs was first used for oxygen plasma treated PDMS with F108 coating according to a static coating procedure (Hellmich et al., 2005) and the mobility values were varied by up to an order of magnitude.

Clearly, *Figure 5-7*a-c show that protein iDEP streaming is enhanced by reducing the electrokinetic component. The concentration factor can be significantly improved up to 11 % for the lowest employed μ_{eo}. Furthermore, this change in the overall μ_{ek} contributes to the characteristic peak formation of the line profiles. *Figure 5-7*d shows the

concentration intensity plots with μ_{eo} ranging from 1.5×10^{-8} m^2/Vs to 0.1×10^{-8} m^2/Vs. Note that the regions of the highest streaming concentration shift inwards with increasing μ_{eo}. Further, these streamlines are broadened towards lower μ_{eo} values.

The following discusses whether under our experimental conditions changes in the EOF could be responsible for the observed pH-dependence of the streaming iDEP. If μ_{eo} is decreased with increasing pH, improved streaming DEP should be expected, as our simulation results in *Figure 5-7*d suggests. It is well known that EOF on PDMS and glass stems from deprotonated silanol groups with a pKa of 3 ~ 5 (Tandon, Bhagavatula, Nelson, & Kirby, 2008). It is thus not likely that pH changes in the range of pH 6 ~ 9 would considerably contribute to EOF changes. Additionally, the channel walls are coated with the tri-block copolymer F108. A pH influence is thus also not likely to occur under these conditions. To experimentally verify this assumption, μ_{eo} was measured in the range of pH 6 ~ 8 under static coating conditions employing F108 as the coating agent. As expected, no significant changes was observed in the magnitude of EOF (data not shown).

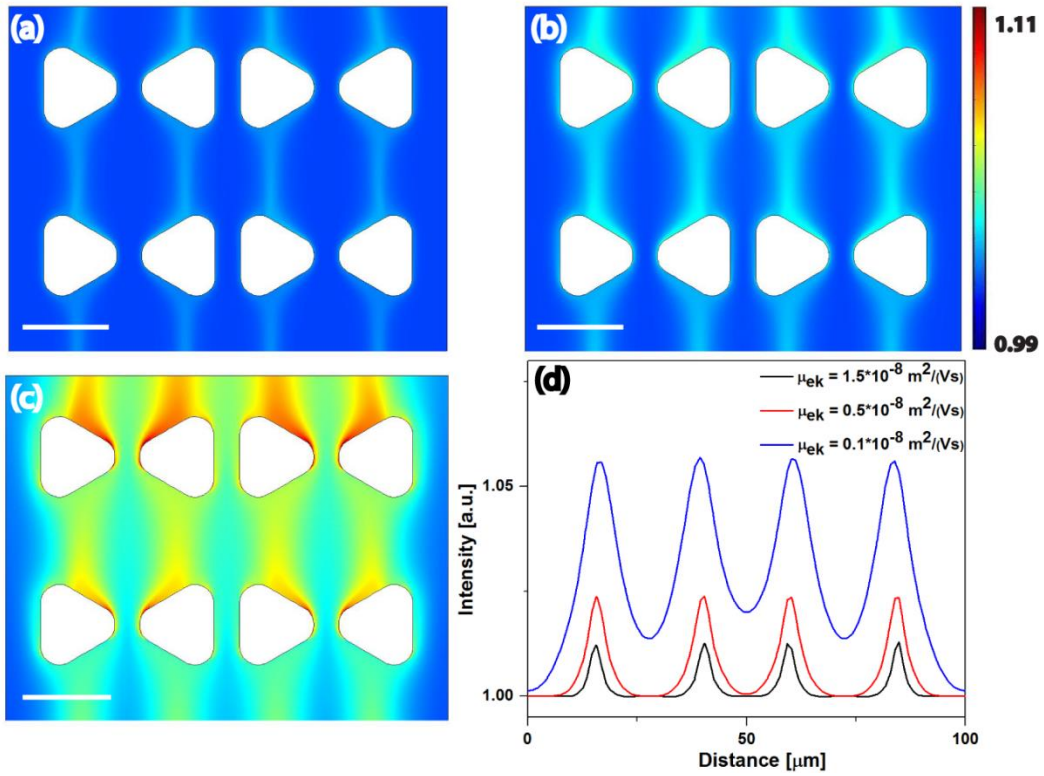

Figure 5-7. DEP streaming simulation with varying μ_{ek} for IgG molecules within a triangular post array at 4200 V/cm. (a-c) Streaming concentration at steady-state according to positive DEP with varying μ_{ek} of (a) 1.5×10^{-8} m^2/V s, (b) 0.5×10^{-8} m^2/V s and c) 0.1×10^{-8} m^2/V s to reflect changes in EOF. (d) Profile plots of (a-c) at the midpoint line of the two rows of posts. μ_{ek} is varied (reflecting changes in EOF) as indicated in the inset while other parameters remain constant with $\mu_{dep} = 8.6 \times 10^{-24}$ m^4/V^2 s and $D = 3.89 \times 10^{-11}$ m^2/s.

Influence of Electrophoresis. Herein, the influence of the protein's electrophoretic mobility (μ_{ep}) is discussed, attributing to the overall electrokinetic transport. Under our experimental conditions, cathodic EOF was observed (Viefhues et al., 2011). Assuming that μ_{eo} found previously for PDMS/glass channels (Hellmich et al., 2005) is in the same order of magnitude (10^{-8} m^2/V s) as μ_{ep} for proteins (Jachimska, Wasilewska, & Adamczyk, 2008), two scenarios are possible. First, the protein has a positive charge; as a consequence EOF and electrophoresis act in the same direction. The second case arises when EOF and electrophoresis counteract due to negatively charged

proteins. In the latter case, the overall electrokinetic transport should be lower in magnitude than in the first case, as a result of the reduced overall μ_{ek}. If strong enough, the overall transport direction changes. As the proteins charge is critically influenced by the solution conditions, changes in the electrokinetic transport are expected for different pH.

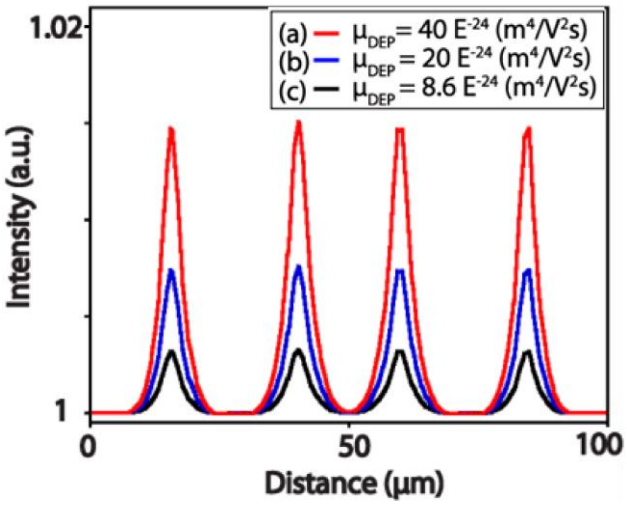

Figure 5-8. Numerically obtained concentration profile plots for varying μ_{dep} at the midpoint line of the two rows of posts while the other parameters stay constant; μ_{ek}= 1.5×10^{-8} m^2/V s and $D = 3.89 \times 10^{-11}$ m^2/s.

In order to understand the influence of the protein charge on DEP streaming, our simulations are discussed for variations of μ_{ek} in relation to our experimental data. First, an isoelectric point of the polyclonal IgG used in this experiment (see Appendix B 2) was determined to be pI ≤ 5. Thus, the negative charge of the protein should rise with an increase in pH. As electrophoresis counteracts EOF in pH > 5 for the employed IgG, a reduced μ_{ek} would be expected. Thus, an overall stronger DEP streaming concentration would be expected with pH values above the pI due to the decreased μ_{ek}. This is underlined by *Figure 5-7*d, indicating increased streaming concentration for lower μ_{ek}.

Indeed, experimentally the streaming DEP concentration is enhanced towards higher pH (see *Figure 5-5*b and *Figure 5-6*a-d).

Influence on DEP Mobility. With the change in a protein's charge, such as induced through pH changes, the DEP behavior could also be influenced. Assuming that a larger amount of charges relates to a larger polarization of a protein, the DEP behavior would increase for pH conditions far from the pI of a protein. Our numerical simulations allow us to examine this scenario as well. *Figure 5-8* shows the changes in the concentration profile arising from an increase in the protein μ_{dep}. As expected, higher μ_{dep}, arising from stronger DEP forces, increases the streaming concentration. Using similar arguments as above for the protein charge state, we conclude that our experiments are also in agreement with an increase in μ_{dep} possibly arising from an increased polarization of the double layer. While our experimental results do not allow us to distinguish between the two cases (increase of DEP or reduction of overall μ_{ek}) I can nonetheless conclude from the simulations that the more pronounced concentration towards higher pH (up to pH 8) is reasonably well explained by the numerical model.

Effect of Surfactants. Our preceding experimental and simulation data demonstrated that highest improvement in DEP concentration is expected around a pH of 8, which can be tuned by decreasing the electrokinetic component and thus favoring DEP vs. streaming. In this study, adsorptive treatment with a tri-block-copolymer F108 was employed to prevent non-specific protein adsorption and control EOF (Alexandridis, Holzwarth, & Hatton, 1994). A recent report demonstrated that dynamic coating, in which the coating agent is apparent in the buffer throughout the entire experiment, is able to reduce EOF even further (Viefhues et al., 2011). Hence, this dynamic coating

procedure was employed in our experiments with 3 mM F108 as final concentration in the buffer and studied its effect on streaming DEP of IgG.

As shown in *Figure 5-9*a, the streaming behavior changed drastically. The regions under which concentration were previously observed (*Figure 5-3* and *Figure 5-6*) are now depleted. In order to further understand this astonishing DEP streaming behavior our results were compared to numerical simulations. Interestingly, simulations of negative DEP closely reflect our experimental observations (*Figure 5-9*b). Therefore, the dynamic coating procedure changed the streaming behavior from positive DEP concentration to negative DEP streaming depletion. To the best of our knowledge, our data are the first to demonstrate negative DC iDEP streaming of a protein caused by a surfactant.

It is noteworthy that these experiments critically depend on the concentration of the dynamic coating agent F108. It has been reported, that the tri-block copolymer F108 forms micelles in solution and that this micelle formation is dependent on temperature. Alexandridis et al.(Alexandridis et al., 1994) found a critical micelle concentration (CMC) of F108 at 25 ºC at 3 mM. Our experiments demonstrating negative DEP were performed with a CMC of 3 mM F108. I therefore propose that micelle formation and integration of IgG therein is responsible for the change in protein DEP behavior. This is likely to occur due to a reduced surface conductivity of the protein micelle so that the Clausius-Mossotti factor changes sign. Note that equation (3. 2) indicates that the Clausius-Mossotti factor is negative when the particle conductivity is lower than that of the medium.

In order to investigate whether micelle formation is responsible for the change of DEP mode from positive to negative DEP, dynamic light scattering (DLS) measurements

were conducted using the same solutions employed for the iDEP experiments (see Appendix B 3). I studied the temperature dependent micellation of F108 alone and with CHAPS and/or IgG added. Our data clearly shows that micellation occurred at 3 mM F108 above 30 °C regardless whether CHAPS is added and independent of IgG addition. I thus conclude that the observed iDEP streaming depletion is due to F108 micelle formation.

This negative DEP behavior was further investigated quantitatively by calculating the concentration depletion factor. Note that the depletion effect was enhanced with increasing the applied electric field from 1400 to 4200 V/cm as demonstrated in *Figure 5-10*. The largest depletion of (54 %) was observed with the highest applied voltage of 4200 V/cm in accordance with a similar trend in concentration increase for positive DEP streaming with applied potential. As previously observed in our numerical simulations (Nakano et al., 2011), DEP experiments demonstrated larger depletion than obtained in the simulation (only 15 %, see *Figure 5-9*b). The simulation was conducted using a μ_{dep} value of -1.28×10^{-23} m^4/V^2s calculated based on the size of the spherical micelle-IgG complex measured by DLS, as well as μ_{eo} of 0.14×10^{-8} m^2/Vs for F108 dynamic coated PDMS channels (Viefhues et al., 2011). Note that the here employed numerical model for DC conditions does not capture the contribution of the double-layer to the protein polarizability in detail (Basuray & Hsueh-Chia Chang, 2010; Zhao, 2011a). I can however speculate that the contribution of double layer polarization and a decrease in the zeta potential due to the polyethylene glycol chains of F108 forming the micelles results in a lower protein conductivity and consequently negative Clausius-Mossotti factor. The influence of dynamic polarization phenomena on nanocolloid polarization was recently

reported (Ermolina & Morgan, 2005; Zhao, 2011a) and may also hold for proteins. In addition to the ionic transport in the double-layer, the electrophoretic motion of proteins may also be responsible for the here observed transition to negative DEP (Zhao, 2011a). The theoretical framework to fully understand protein DEP (including DC iDEP) needs yet to be fully developed and a further study of DC and AC protein DEP may provide more insight into protein polarization and DEP.

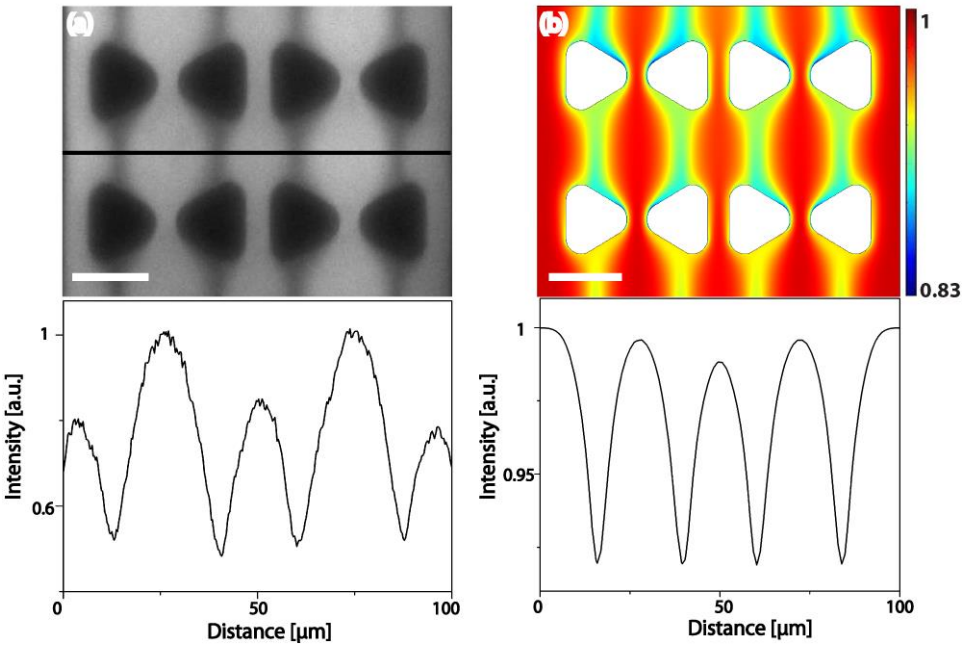

Figure 5-9. Experimental and simulation results of negative iDEP streaming for 3 mM F108. (a) Fluorescence microcopy image of streaming iDEP of fluorescently labeled IgG molecules in a triangular post array for 3 mM F108. Concentration depletion along the streamlines is observed due to negative DEP at an applied electric field of 4200 V/cm at pH 8. (b) Normalized concentration as obtained from the simulation within a triangular post array at 4200 V/cm in the case of negative DEP (μ_{dep} =-1.28 × 10^{-23} m^4/V^2 s). The scale bar indicates 20 µm and the flow direction is from top to bottom. The color bar indicates concentration in arbitrary units.

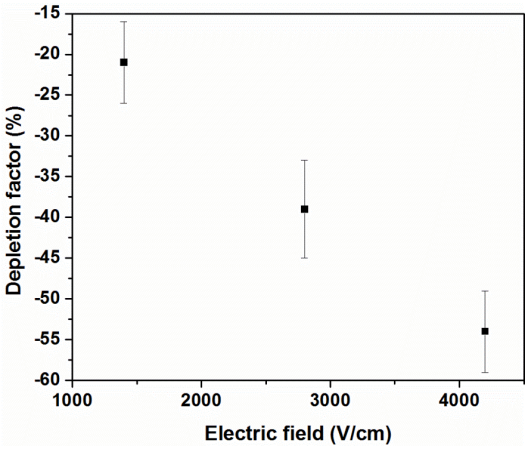

Figure 5-10. Depletion factors under 3 mM F108 dynamic coating for an applied potential of 1400, 2800, and 4200 V for a 1cm channel.

SECTION CONCLUSIONS

In this chapter, I demonstrated successful iDEP-based manipulations of proteins with different geometries in a PDMS-based microfluidic system. Theoretical considerations predicted positive DEP behavior for proteins resulting in locally concentrated streamlines, which were accurately observed in experiments and were in excellent qualitative agreement with simulations. Moreover, this work demonstrates that protein aggregation readily occurs using standard phosphate buffers without the use of additives. These protein aggregates exhibit a different behavior (i.e. trapping) as opposed to individual proteins in the presence of a surfactant. Additionally, our experimental results demonstrated a thorough investigation of the factors affecting protein iDEP. The higher concentration is achieved with lower conductivity buffer in the range of 0.01 ~ 0.04 μS/cm. Furthermore, a suitable pH range of pH 6 ~ 8 was revealed, under which IgG iDEP concentration can be performed without aggregation. Moreover, the influence of electrokinesis was studied thoroughly by numerical simulations. I postulate that the numerical modeling will be useful in the future, when more quantitative data obtained

from independent experimental techniques and theoretical models on biomolecule polarization become available. This will allow the prediction of migration differences for proteins and eventually reveal suitable separation and fractionation conditions for biomolecules based on DEP. Our work is thus an important step towards employing DEP as a new analytical tool for biomolecules.

Moreover, this work demonstrated a clear distinction between positive and negative iDEP streaming of proteins. For the first time, both positive and negative DEP were demonstrated with the same protein species only by tuning the surrounding environment with a surfactant. Micelle formation was expected to be responsible for the observed negative DEP. Our results indicate the potential for manipulation of biomolecules with molecular dimension smaller than 10 nm thus highlighting the ability to manipulate proteins using DEP. Specifically, streaming DEP has demonstrated the ability to concentrate proteins within a microfluidic device thus providing an exciting new tool for protein analysis devices in microfluidic format. The enhancement of this iDEP concentration is anticipated by further optimization of the device geometry (see Chapter 6) with the aid of the theoretical model presented herein and the future application of iDEP for analytical applications of proteins on microfluidic platforms.

CHAPTER 6

PROTEIN INSULATOR BASED DIELECTROPHORESIS WITH NANOCONSTRICTION DEVICES

INTRODUCTION

In the previous chapter, the potential of iDEP was demonstrated to manipulate proteins under DC conditions, providing the demonstration of protein iDEP streaming for the first time. Additionally, the buffer conditions were optimized to achieve the highest protein concentration by performing a thorough investigation of the factors influencing protein DEP, such as electrophoresis and electroosmosis. The previous investigations presented the potential of iDEP device with micropost arrays as a pre-concentration tool, however, they also showed that such micropost iDEP devices cannot create high enough electric field gradients with which DEP force overcomes electrokinetic force.

To achieve such high electric field gradients for manipulation of sub-micrometer sized proteins, improvement of our pre-existing device with triangular microposts was attempted (Nakano et al., 2012). A gap distance of a few hundred nanometers was created by fabricating additional rectangular posts between the tips of the microposts by focused ion beam milling (FIBM). This nano-constriction device allowed the transition from streaming DEP to trapping DEP for λ-DNA with more than 10^3-fold concentration enrichment (Camacho-Alanis et al., 2012). Here, protein DEP in this nano-constriction device are investigated with β-galactosidase and IgG under both DC and AC conditions. These experimental results are compared with numerical simulations in order to estimate the unknown experimental parameters, in particular, electrokinetic and DEP mobility to

aid our understanding of protein DEP response. Finally, I discuss additional factors influencing protein DEP concentration using this nano-constriction DC-iDEP device.

NUMERICAL COMPARISON BETWEEN MICRO AND NANOPOST ARRAYS

Our improved structure was fabricated based upon the existing iDEP device with triangular micropost arrays since this geometry was well-characterized for application of protein iDEP as demonstrated in the previous chapter. In addition to a standard optical lithography to fabricate triangular micropost arrays, focused ion beam milling (FIBM) was employed to create an additional rectangular post between the triangular posts where the vertices face each other. *Figure 6-1*c-d show the SEM images of the resulting PDMS structures of a triangular post array device and nano-constriction device of which the length of the constriction was found to be 100 ~ 500 nm. Note that due to the difficulty of FIBM, the size of the constriction is not uniform throughout the array. Table 6-1 and *Figure 6-1*a-b provide the comparison of maximum electric field strength and the distribution of $\nabla \boldsymbol{E}^2$ resulting from each device, revealing that the maximum electric field increases by nearly a factor of four. Moreover, the maximum $\nabla \boldsymbol{E}^2$ is enhanced by two orders of magnitude with which the resulting DEP force increases by up to two orders of magnitude in theory based on the relation in equation (3. 1).

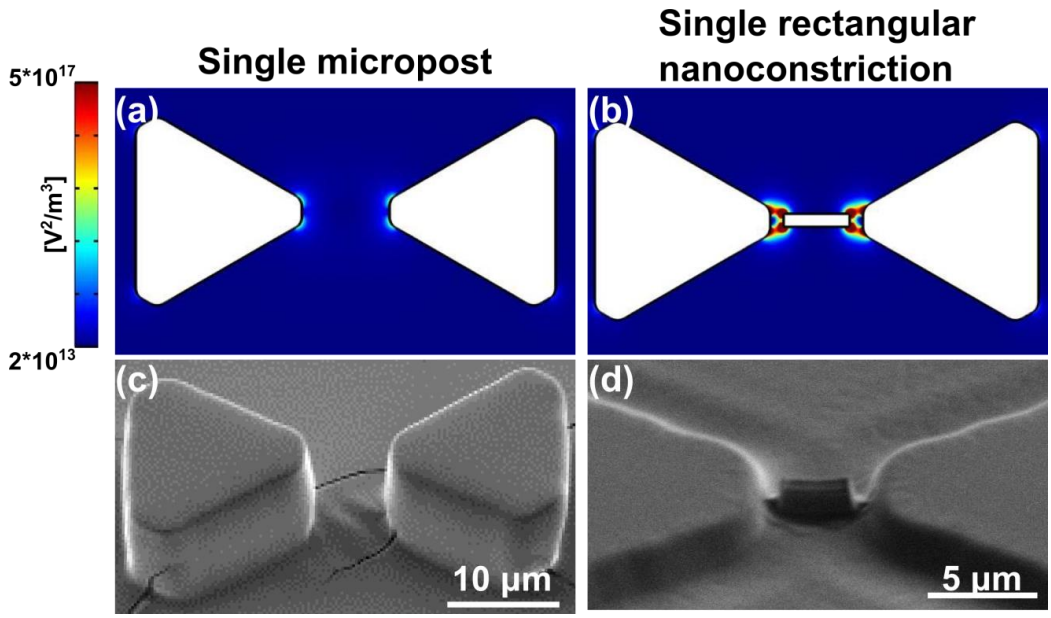

Figure 6-1. Comparison of micropost iDEP device and nano-constriction device (a, b) $\nabla \boldsymbol{E}^2$values simulated numerically (c,d) SEM images of a micropost array and nano-constriction iDEP device.

Table 6-1
Comparison of maximum electric field strength and maximum$\nabla \boldsymbol{E}^2_{max}$ values resultant from a micropost array and nano-constriction iDEP device via numerical simulations.

	$\boldsymbol{E}_{max}$[V/m]	$\nabla \boldsymbol{E}^2_{max}$[V^3/m^2]
Micropost array	4.5×10^5	3.5×10^{17}
Nano-constriction	1.6×10^6	3.3×10^{19}

DIELECTROPHORETIC BEHAVIOR OF PROTEINS UNDER DC CONDITIONS

Immunoglubulin G and beta-galactosidase Dielectrophoresis. The DEP behavior of the two proteins IgG and β-galactosidase was investigated using the nano-constriction DC iDEP device shown in *Figure 6-2*. For DEP experiments, proteins were suspended in a low conductivity buffer (100 μS/cm) at pH 8 with the zwitterionic

additive CHAPS as previously used to reduce protein aggregation (Nakano et al., 2011). Upon application of 100 V for a 0.8 cm long channel, IgG was transported through the channel by anodic electrokinetic flow and was concentrated at the outlet side of the nano-constriction (*Figure 6-3*a). This protein concentration was attributed to positive DEP based on the regions of the concentration and depletion around the nanoposts schematically depicted in *Figure 6-3*e. Protein concentration occurs at the outlet side of the nano-constriction since pDEP force is directed toward the nano-constrictions counteracting electrokinetic flow. On the other hand, protein depletion occurs at the inlet side since an overlay of pDEP with electrokinesis creates faster overall flow, resulting in depletion. This is in agreement with the pDEP behavior of IgG using an micropost iDEP device under DC conditions presented in the previous chapter (Nakano et al., 2012, 2011).

Subsequently, β-galactosidase was employed for iDEP experiments which is known to form a tetramer in native state with a molecular weight of 465 kDa (Jacobson et al., 1994). After the channel was filled with the protein and a steady state was established, β-galactosidase started to concentrate at the inlet side with an application of 100 V for a 0.8 cm channel as shown in *Figure 6-3*b. As flow directions indicated by arrows in *Figure 6-3*b, β-galactosidase was transported by cathodic electrokinetic flow. Note that the direction of the bulk flow changed from anodic in case of IgG to cathodic flow, which was attributed to the change in electrokinetic velocity comprised of electrophoresis and electroosmosis. The isoelectric point of β-galactosidase (~4.6) is similar to that of IgG used in the previous experiment. However, the decreased electrophoretic component can be expected for β-galactosidase due to its larger size

which leads to a decrease of the charge density. *Figure 6-3*b shows that the β-galactosidase concentration occurred at the inlet side of the nano-constrictions in contrast to IgG, while the outlet side resulted in protein depletion. As depicted schematically in *Figure 6-3*f, this concentration and depletion is characteristic to negative DEP interplaying with electrokinesis.

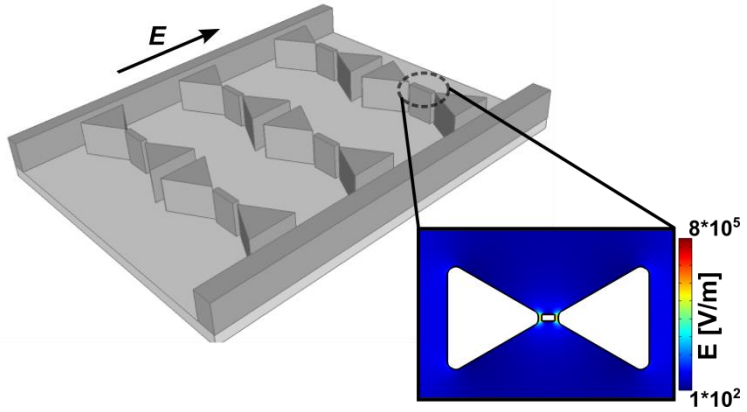

Figure 6-2. Schematic of the nano-constriction iDEP device (not to scale) where an inhomogeneous electric field is created at the nano-constrictions as depicted in the zoom in representation.

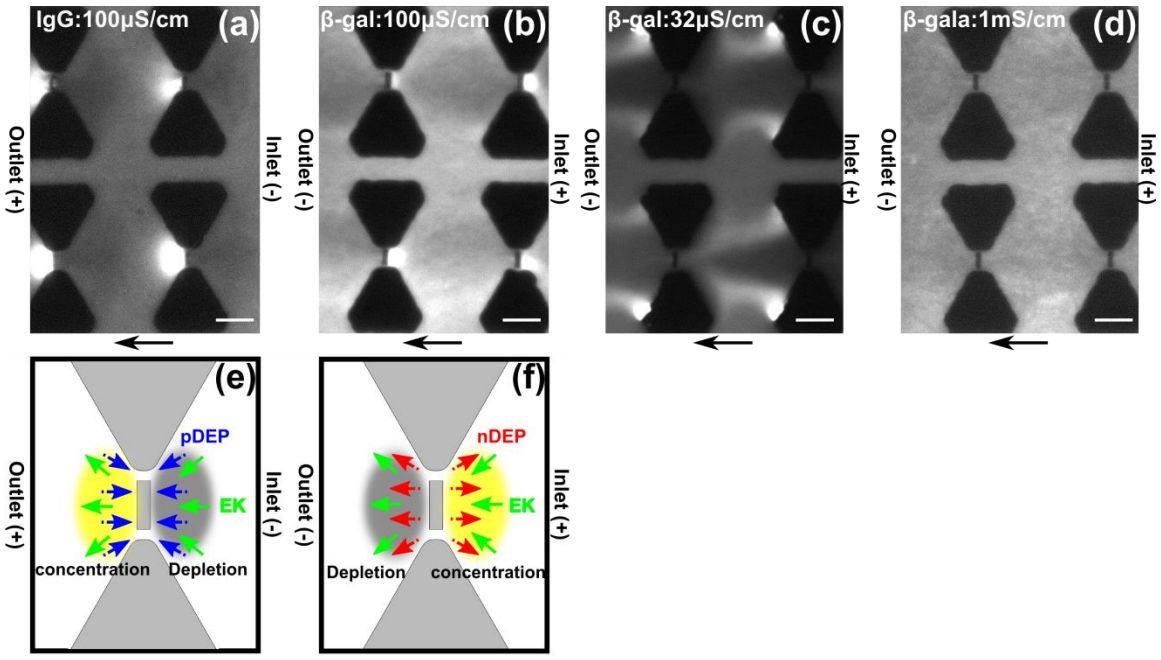

Figure 6-3. Fluorescence microscopy images obtained from DC iDEP experiments and schematic images to explain DEP behavior with two different proteins, IgG and β-galactosidase and various buffer medium conductivities. Flow direction is from right to left. Scale bar indicates 10 µm. (a) IgG concentration at the outlet side of the nanoposts and slight depletion at the opposite side due to positive DEP with 100 µS/cm phosphate buffer with 250 V potential for a 1.5 cm channel. (b) β-galactosidase concentration at the inlet side of the nanoposts and depletion at the outlet side due to negative DEP with 100 µS/cm phosphate buffer with 100 V for a 0.8 cm channel. (c) β-galactosidase concentration behavior with 32 µS/cm HEPES buffer with 100 V for a 0.8 cm channel. (d) β-galactosidase showing no apparent concentration change throughout the channel with 1 mS/cm phosphate buffer with 100 V for a 0.8 cm channel. (e-f) Schematics showing the flow directions due to DEP and electrokinesis and the resultant species concentration and depletion around the nanoconstriction. (d) Positive DEP counteracting electrokinesis at the outlet side of the nanopost, resulting in protein concentration at the outlet side, whereas depletion is apparent at the inlet side. (e) Protein concentrates at the inlet side of the post due to negative DEP interplaying with electrokinesis.

FACTORS INFLUENCING PROTEIN DIELECTROPHORESIS UNDER DC CONDITIONS

Dependence on Buffer Conductivity. Both DEP and electrokinesis are influenced by the buffer medium conductivity. Therefore, the influence on protein DEP concentration in relation to buffer conductivity was investigated. To this aim, the DEP

experiments were repeated with β-galactosidase using the following buffers: 32 µS/cm HEPES and 1 mS/cm phosphate buffer. *Figure 6-3*c showing the DEP behavior with 32 µS/cm buffer conductivity demonstrates strong depletion around the nanoposts which even expands to the regions between the rows of the microposts. In case of higher conductivity buffer of 1 mS/cm, no concentration or depletion was observed as shown in *Figure 6-3*d. The lack of changes in the protein concentration at this medium conductivity is a surprising finding. Based on the classical theory, a somewhat stronger nDEP response would occur since the CM factor should be more negative with higher buffer medium conductivity. Additionally, a smaller electrokinetic mobility would be expected under higher medium conductivity. A similar conductivity dependency was previously reported in case of pDEP for IgG with which the iDEP concentration effect decreased with increasing the buffer conductivity (Nakano et al., 2011). I can speculate on the possible reason for this behavior in relation to the contribution of EDL polarization for sub-micrometer particles. It was previously shown that nanocolloidal particles with thick EDL exhibit extraordinary large EDP response largely due to their electrophoretic motion distorting the ion distributions within the EDL (Zhao & Bau, 2009). The EDL thickness is estimated to be 18 nm for 32 µS/cm buffer and 3 ~ 4 nm for 1 mS/cm. Therefore, proteins in the smaller buffer concentration would show increased DEP response compared to the ones in the higher conductivity buffer. Recently, Zhao and Bau demonstrated that a thick EDL accounts for a major contribution to the total dipole moment in the case of DNA (Zhao & Bau, 2010). Although this model has not yet been extended to proteins, it might hold for our experimental observations.

Magnitude of the Dielectrophoretic Mobility and Simulations. Even though a general model to describe protein polarization is lacking, it is of importance to estimate DEP force to understand the polarization behavior of proteins. For this purpose, numerical simulation serves as a helpful tool to compare with the experimental results. The concentration distribution within the iDEP device can be assessed by solving the convection-diffusion model presented in chapter 3 under steady state condition. The μ_{dep} value for β-galactosidase was first calculated based on the protein dimension of $9 \times 7 \times 5$ nm measured via x-ray crystallography data (Jacobson et al., 1994) from which the shape as an oblate ellipsoid was approximated. Using the classical model developed for the shape (Rivette & Baygents, 1996) and assuming $\sigma_m = 0$ S/m to simulate an extreme nDEP case, a negative DEP mobility of -8.95×10^{-24} m^4/V^2s was obtained. However, using the apparent μ_{ek} of 1.5×10^{-8} m^2/Vs for PDMS statically coated with F108 (Hellmich et al., 2005), the result did not produce significant change in concentration distribution (less than 0.1 %) in simulations according to this model (data not shown). Considering that no appropriate model has been developed for protein DEP response, the classical theory developed to model solid particle DEP response might be over-simplified which does not accurately represent protein complexity. Moreover, it has been evidenced that nano-sized colloidal particles with thick EDL exhibit exceptionally large DEP response due to EDL polarization (Basuray & Chang, 2007; Ermolina & Morgan, 2005; N.G Green, Morgan, & Milner, 1997) as well as the particle's electrophoretic motion (Zhao & Bau, 2009).

Therefore, the concentration distribution was further investigated with various μ_{dep} and μ_{ek} values attempting to match the experimentally observed distributions in

protein concentration in the nano-constriction under iDEP conditions with simulations. The μ_{ek} was varied from 1.5×10^{-7} to 1.5×10^{-9} m^2/V s and μ_{dep} ranging from -4.5×10^{-24} to -4.5×10^{-21} m^4/V^2 s. As a result, two distinctive types of concentration distribution were found: type A in which the protein is depleted around the nanopost and type B in which the protein concentration is enhanced at the inlet side of the constriction as shown in the inset of *Figure 6-4*.

These simulated concentration patterns were compared with the *β*-galactosidase iDEP experiment at a conductivity of 100 µS/cm as shown in *Figure 6-3*b. The type B distribution was found to qualitatively best represent the experimental results where the concentration enriches at the inlet side and depletes at the opposite side. By analyzing the variations of μ_{ek} and $\mu_{dep,}$ I found that the parameter set of -4.5×10^{-23} m^4/V^2s $\geq \mu_{dep}$ and $\mu_{ek} \geq 1.5 \times 10^{-8}$ m^2/V s show type B behavior similar to the experimentally observed concentration effect. It is interesting to know that previously a value of 1.5×10^{-8} m^2/Vs was reported for μ_{ek} under similar buffer conditions in PDMS devices (Hellmich et al., 2005). This leads to the conclusion that μ_{dep} is underestimated with the classical model.

The numerically obtained concentration patterns are also discussed in relation to variations in the medium conductivity with *β*-galactosidase. In the case of 32 µS/cm the simulation results indicate that the experimentally observed concentration matches a type A concentration distribution. This transition can be explained with the increase in the zeta potential of the channel surface, thus enhanced electrokinetic mobility induced through a decreased ion concentration of the buffer medium. *Figure 6-3*c clearly shows the transition of concentration distribution from type B to A with increased electrokinetic mobility.

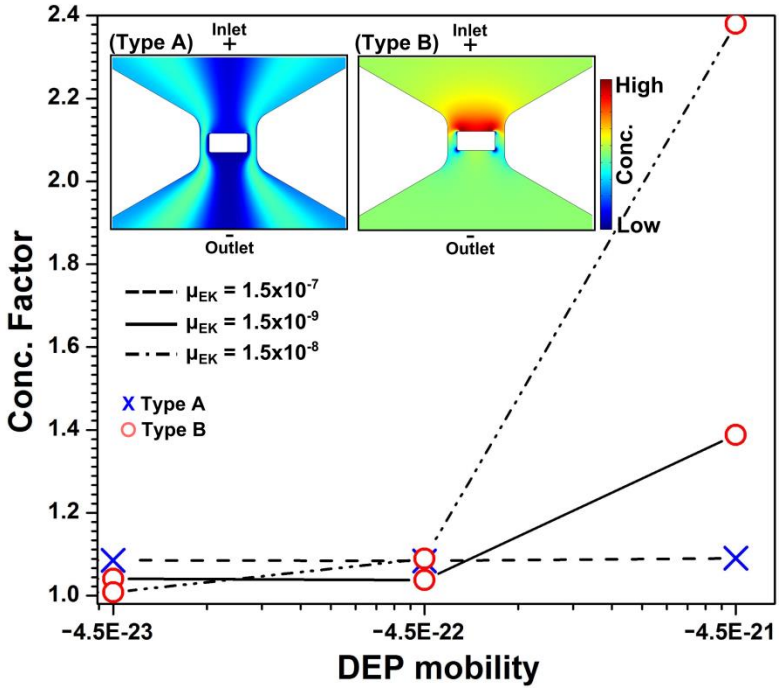

Figure 6-4. The resultant concentration factors obtained by numerical simulations are plotted as a function of μ_{dep} for three different electrokinetic mobilities with 1.5×10^{-7}, 1.5×10^{-8}, and 1.5×10^{-9} m^2/V s . Different markers are used in order to represent the different types of concentration distributions: red circle markers and blue cross markers representing the type A and B concentration distributions, respectively. The inset shows representative images of these two types of concentration distributions, type A and type B.

Applied Potential Dependency on Protein Concentration. Subsequently, the DEP behavior of β-galactosidase was investigated in dependence of the applied potentials in a range from 50 V to 500 V at a medium conductivity of 100 µS/cm. Fluorescent microscopy images shown in *Figure 6-5*a-d demonstrate a transition of concentration distribution with increasing applied potential. With only 10 ~ 20 V, β-galactosidase was depleted at the outlet side (data not shown). Subsequently, by gradually increasing the applied potential β-galactosidase started to concentrate at the inlet side, while depletion at the outlet side intensified (*Figure 6-5*a, at 50 V). This protein enrichment at the inlet side was enhanced with increasing the voltage further (*Figure 6-5*b, at 100 V) and a similar

concentration trend was observed with higher applied potentials up to 200 V (*Figure 6-5*c). However, protein streaming from the inlet side started with applied potential higher than 200 ~ 300V (*Figure 6-5*d, at 500 V).

It is interesting to discuss the transition of concentration distribution as shown in *Figure 6-5*a-d in dependence of applied potentials. To clearly visualize the concentration distribution around the nano-constriction regions where the higher electric field gradients are created, fluorescence intensity profiles perpendicular to the nanopost are plotted with different applied potentials (*Figure 6-5*h). For this operation, the fluorescence intensities are normalized with the intensities at the same region obtained at 0 V. Interestingly, the maximum concentration was observed ~ 5 μm away from the nanopost at the inlet side at 50 V. By increasing the potential, the concentration maximum approached the nanopost and was closest to the nanopost at 200 V. Concomitantly, the peak maximum increases with increasing applied potential with a maximum concentration factor of 3.8 at 200 V. Assuming that DEP is the dominant cause for protein concentration around the nanopost, the highest concentration increase would be expected to coincide with the highest electric field gradient region (i.e. the corner of the nanoposts in our device). Thus, the observed variation of peak maximum cannot solely be explained through DEP.

To further characterize the voltage dependent protein DEP behavior, numerical simulations were carried out to reveal concentration distribution in the iDEP device. *Figure 6-5*e-g shows the normalized concentration distribution around the post regions at 50 V, 100 V, and 500 V estimating the following parameters for the simulation: μ_{ek} = 1.5×10^{-8} m^2/V s and μ_{dep} = $- 9 \times 10^{-22}$ m^4/V^2 s for β-galactosidase exhibiting negative DEP. Simulation results using these parameters revealed type B concentration

distribution and a similar voltage dependency as observed in the experiments. Specifically, the region of protein concentration is located at the inlet side of the nanopost at 50 V (*Figure 6-5*e) and 100V (*Figure 6-5*f), whereas the opposite side is depleted. With the higher applied potential of 500 V, the concentration distribution changed its shape drastically as shown in *Figure 6-5*g where streamlines similar to the experimental observations were apparent. Although the concentration distribution obtained by simulation is similar to our experiments, I noticed a difference. The experimentally observed concentration at 50 ~ 200 V is more delocalized compared to the simulation where the protein concentration only occurs at very small region adjacent to the nanopost. This localized concentration would be expected considering that the high electric field gradient region is strongly localized around the corners of the rectangular nanoposts.

It is likely that multiple phenomena contributing to protein migration play a role and change their balance in dependence of the applied potentials. For instance, numerical simulations previously showed that the change in electrophoresis, electroosmosis, and DEP influences the protein concentration profiles in DC iDEP (Nakano et al., 2012). However in the nano-constriction device as employed in this study, I suggest an additional factor influencing the concentration behavior due to the nanometer-sized constrictions. It is known that nanometer-sized channels with critical dimension of 10 ~ 100 nm exhibit a unique ion permselectivity due to their overlapping electrical double layer, termed ion concentration polarization (ICP) (S. J. Kim, Li, & Han, 2009; S. M. Kim, Burns, & Hasselbrink, 2006; Napoli, Eijkel, & Pennathur, 2010; Y.-C. Wang, Stevens, & Han, 2005). The SEM images of our device revealed the smallest constrictions scale down to ~ 100 nm. These small constrictions are known to generate

ICP, which dynamically changes ion concentration gradients around the nano-constriction under the ionic strengths employed here. At low voltages, protein transported through the channel by cathodic electrokinetic flow is depleted at the outlet side of the nanopost and concentrated on the opposite side due to nDEP in accordance with the simulation shown in *Figure 6-5*e-f. However, at the same time as DEP concentration, protein started to concentrate several micrometer away from the nanopost which is assumed to be triggered by ICP. Since ICP is known to create parabolic-like backflow at the ion depletion zone formed in front of the nanostructure (see *Figure 6-6*), ICP would enhance the protein concentration caused by nDEP. While increasing the voltage, the concentration zone due to ICP moves closer to the nanoposts since the forward electrokinetic flow increases. As the nanopost region is approached, nDEP protein concentration also enhances due to the larger electric field gradient at the nano-constriction, resulting in the overall concentration enhancement adjacent to the nanoposts.

This aforementioned scenario involving the interplay of DEP, EK, and ICP creates a unique voltage dependent concentration distribution caused by a dynamic change of the local environment (i.e. electric field distribution and ion distribution). Therefore, it is worthwhile to discuss the influence of the local changes on iDEP and the resultant concentration distribution. The presence of the nanostructure acting as a permselective membrane induces the formation of ICP with an overall ion depletion zone at the anodic side, whereas an ion enrichment zone on the opposite side of the nanostructure (Zangle, Mani, & Santiago, 2010). Thus, the formation of ICP leads to a dynamic change in local conductivity which results in a potential drop in the depletion

zone at the inlet side of the nanostructure. Specifically, considering our mico-/nanopost structure the influence of the dynamic changes can be discussed in two separate regions: anodic side (inlet side of a nanopost) and the cathodic outlet side. First, the inlet side of the nanopost is characterized by depleted ion concentration due to ICP. Kim et al. previously measured the electric field strength in the depletion zone to be as high as ~1000 V/cm with the externally applied electric field of 30 V/cm (S. J. Kim et al., 2009). This largely enhanced electric field amplifies the electrokinetic migration at the inlet side of the nanostructure thereby counteracting DEP. In terms of DEP the CM-factor for nDEP results in a smaller negative value due to ion depletion (i.e. decreased σ_p) at the inlet side. Therefore, one can expect a declined DEP force. On the other hand, the local electric field at the outlet side of the nanopost is significantly lowered due to ICP, leading to a smaller electrokinetic migration. Moreover, one would expect the increase of nDEP forces since the CM-factor becomes more negative with increased σ_m at the outlet side due to ICP. Even though it is challenging to quantitatively assess the effect of ICP with our current device, I can conclude that the observed concentration distribution resulted from dynamic changes of electrokinesis and iDEP due to the change in ion concentration originating from ICP at nano-constrictions. Moreover, protein concentration can decrease at the anodic inlet side due to amplified electric fields (e.g. increased EK) as well as declined DEP forces. On the other hand, nDEP is enhanced at the cathodic outlet side.

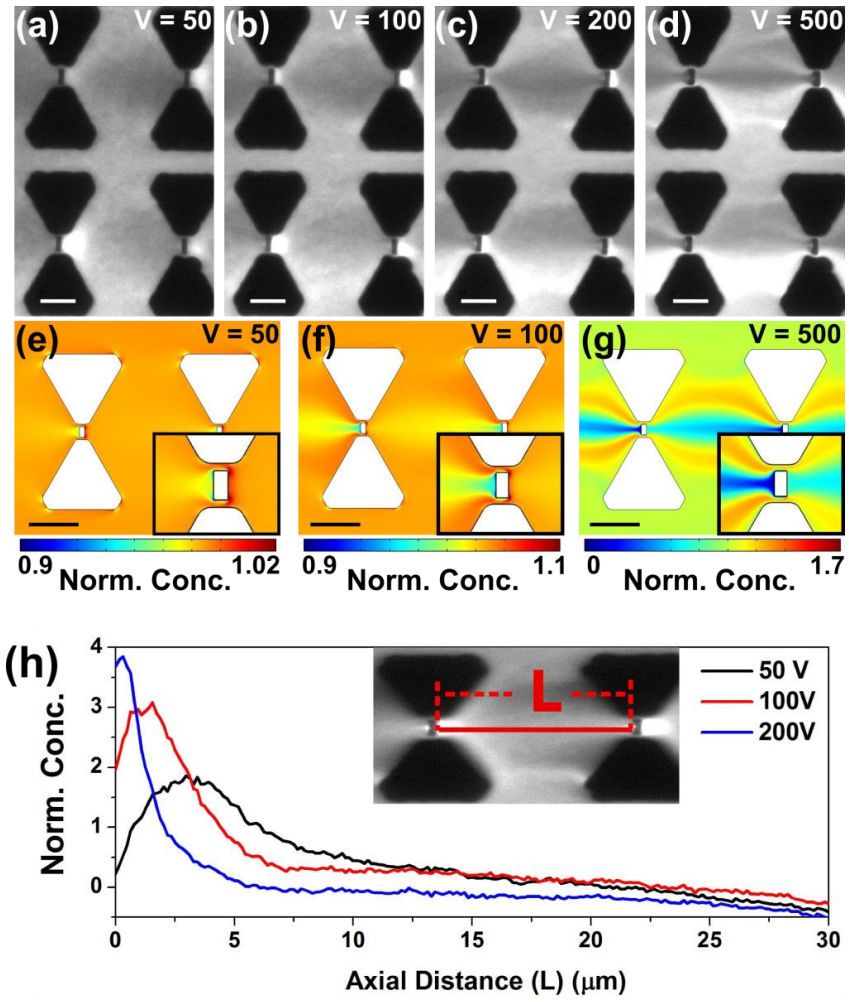

Figure 6-5. Experimental results and numerical simulations for the nano-constriction iDEP device with integrated triangular microposts and rectangular nanoposts between the tips of the triangles. Flow direction is from right to left in the cathodic direction. Scale bar indicates 10 μm. Fluorescence microscopy images obtained by DC-iDEP experiments with β-galactosidase, demonstrating voltage dependent concentration distributions due to nDEP with the following applied voltages: (a) 50 V (b) 100 V, (c) 200 V, and (d) 500 V for a 0.8 cm long channel. (e-g) Numerical simulation results with the same external electric field as the experiments: (e) 63 V/cm, (f) 125 V/cm, and (g) 625 V/cm. The insets show the close-up around the nanopost region where the highest electric field gradient is expected. (h) Protein concentration profiles extracted from the concentration distribution at the regions perpendicular to the nanopost as indicated in the inset image and plotted as a function of voltages 50, 100, and 200 V applied potential for a 0.8 cm channel. Fluorescence intensity is normalized with the intensity at the same region at 0 V.

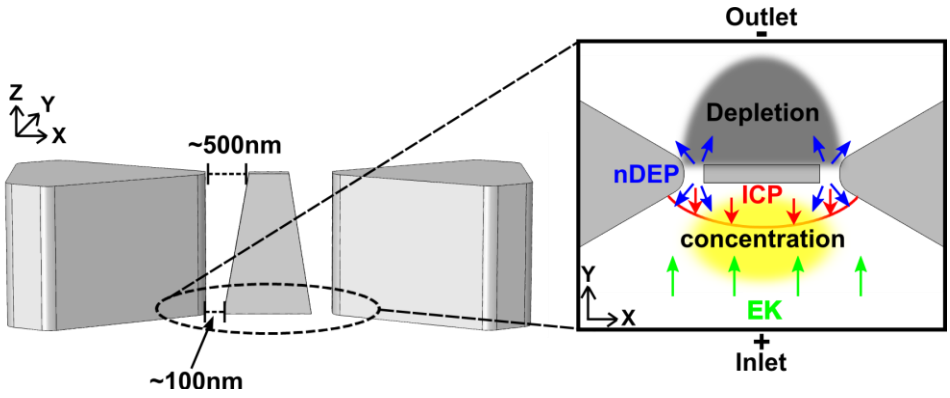

Figure 6-6. A schematic to explain the occurrence of ICP showing the micro- and nanopost region showing the frontal cross section of the triangular and variable width rectangular posts. The smallest constriction scales down to ~ 100 nm which can cause ion concentration polarization. An inset shows the force balance around the nano-constriction including electrokinesis, negative DEP, and ICP and resultant concentration distribution.

Theoretical Considerations to Understand Dielectrophoretic Properties of Proteins. Our experimental results in comparison to the numerical simulation suggested that the DEP mobility calculated using the classical model might underestimate the actual DEP response of proteins. Therefore, factors contributing the overall DEP response of proteins are herein discussed.

Proteins are polypeptides composed of amino acids forming a particular tertiary structure. A dipole arises in most proteins due to the spatial arrangements of polarizable groups originating from polarizable bonds in the polypeptide backbone. Polar and charged groups of the amino acid side chains (Pethig, 1979) or specific motifes such as α-helices also contribute to some extent to the overall protein dipole (J. Antosiewicz, 1995; Jan Antosiewicz & Porschke, 1989). Dipoles arising from the molecular composition of proteins are usually termed permanent dipoles with typical magnitudes of a few hundred Debye (J. Antosiewicz, 1995; Oleinikova, Sasisanker, & Weingärtner, 2004; Sasisanker, Oleinikova, Weingärtner, Ravindra, & Winter, 2004; Takashima,

2002). Dipolar contributions from solvent (water) and solvent-protein interactions also contribute to the protein dipole moment. Moreover, the distribution of ions in the electrical double layer (EDL) characterized via the Debye layer thickness, λ_D, can give rise to polarization influencing protein dielectrophoretic response (Michael Pycraft Hughes, 2002). In contrast to contributions from the permanent dipole, the polarization in the EDL can account for a characteristic frequency dependent DEP.

Here, I attempt to calculate DEP force acting on a protein arising due to the protein's permanent dipole using equation (1. 4). Previous work demonstrated that the protein dipole moment varies strongly among proteins ranging from < 100 D to several hundred D. For example, the protein lysozyme was reported to have a dipole moment of 223 D, whereas the dipole moment of ribonuclease A with similar molecular weight amounts in ~ 400 D (Oleinikova et al., 2004). In the following, the DEP force arising due to protein's permanent dipole is calculated. With the dipole moment of lysozyme of 223 D reported previously (Matyushov, 2012a) as well as an experimental arrangement, in which an electric field gradient of 10^{13} V/m^2 is established (in case of nano-constriction iDEP device shown in this chapter), the resulting DEP force acting on a protein can be estimated with equation (1. 4). For lysozyme, this results in a force of ~ 10 fN.

Classical DEP theory using the well-described DEP response of nanoparticles was also used to quantitatively describe protein response. As shown in Table 3-1 in chapter 3, the polarizability of IgG and β-galactosidase was calculated using the classical theory formulated for a prolate ellipsoid for IgG (see numerical model in chapter 3) and oblate ellipsoid shape for β-galactosidase (see Appendix A 1), respectively. As a result, the

polarizability was 5.34×10^{-34} F/m^2 for IgG and -1.15×10^{-33} F/m^2 for β-galactosidase. Using equation (1. 6), the DEP force acting on IgG and β-galactosidase was calculated as ~20 fN and ~40 fN, respectively, assuming the $\nabla \boldsymbol{E}^2_{max} = 3.3 \times 10^{19}$ V^3/m^2 obtained via numerical simulations for the nano-constriction iDEP device.

Additionally, to compare the magnitude of the electrokinetic force ($\boldsymbol{F_{ek}}$) with the DEP force ($\boldsymbol{F_{dep}}$), $\boldsymbol{F_{ek}}$ was evaluated using the following relation (Liao et al., 2012):

$$\boldsymbol{F}_{ek} = f \mu_{ek} \boldsymbol{E} \tag{7. 1}$$

where f denotes the friction coefficient ($f = 6\pi\eta\bar{R}$) where $\bar{R}$ is calculated as a shape dependent factor (see Appendix A 1). In case of IgG, I calculated $\bar{R} = 3.29 \times 10^{-9}$ m and $f = 6.2 \times 10^{-11}$ N·s/m. Similarly, $\bar{R} = 6.8 \times 10^{-9}$ m and $f = 1.28 \times 10^{-10}$ N·s/m were obtained for β-galactosidase. Assuming $\boldsymbol{E}_{\max}$ of 1.6×10^6 V/m, $\boldsymbol{F_{ek}}$ resulted in ~ 1 pN for both proteins. This comparison of $\boldsymbol{F_{dep}}$ and $\boldsymbol{F_{ek}}$ shows that DEP does not overcome electrokinesis with our iDEP device (see Table 6-2). However, I should note that the aforementioned calculation was a gross estimate performed using the maximum $\boldsymbol{E}$ and $\nabla \boldsymbol{E}^2$ not necessarily found at the same spatial location in the iDEP device. Additionally, electrophoresis was assumed to be negligible compared to the electroosmosis and the other contributing factors such as diffusion and electrothermal flow were also not accounted for in this comparison.

Table 6-2
Gross estimates of the magnitude of DEP and electrokinetic force

DEP force due to protein's permanent dipole	DEP force using classical theory[b]	Electrokinetic force
~ 10 fN (lysozyme)[a]	~ 20 fN (IgG) ~40 fN (β-galactosidase)	~ 1 pN

[a] Calculated using the dipole moment of lysozyme of 223 D (Matyushov, 2012a)
[b] Calculated using the classical DEP theory for a prolate ellipsoid shape for IgG and oblate ellipsoid model for β-galactosidase.

However, this estimation/comparison suggests that the classical DEP theory underestimates the DEP response of proteins. This classical approach might be over-simplified and does not account for detailed protein structure, solvent interactions, or EDL polarization.

In order to account for the complexity of protein dielectrophoresis, polarization effects in the EDL should play an important role influencing the dielectrophoretic behavior of proteins (Michael Pycraft Hughes, 2002). Thus, the DEP response should deviate from the classical cell and particle models. In analogy, it has been experimentally evidenced that sub-micrometer particles with EDL thickness comparable to the particle diameter show different DEP behavior than similar micrometer-sized particles (Nicolas G. Green & Morgan, 1999). Polarization and induced dipoles due to the EDL surrounding a nanometer-sized particle should thus play an important role in DEP behavior of proteins. Two major mechanisms are considered to contribute to the EDL polarization. The first contribution is attributed to ionic currents caused by ion migration and convection within the EDL. In addition, the electrophoretic motion of the particle modifies the ion distribution around it, leading to changes in the induced dipole moment

(Dukhin, 1993). The classical Maxwell-Wagner-O'Konski (MWO) model accounts only for ion migration and convection as a surface conductivity.

Recently, Basuray and Chang (Basuray & Chang, 2007; Basuray, Wei, & Chang, 2010) proposed another modified MWO theory by accounting for a normal current component in the diffuse layer as well as the classical tangential current. Their model extends to situations where the radius of the particle is comparable to the thickness of the Debye layer. The normal component of the ion migration within the diffuse layer leads to ion adsorption on the Stern layer at the particle poles, thus inducing capacitive properties in the EDL which influence the polarization. Interestingly, the induced dipole moment results in one order of magnitude larger than predicted by the classical MWO theory (Basuray & Chang, 2007). This larger induced dipole moment has important experimental implication, as smaller electric field gradients could be used for protein DEP manipulations. Experimentally, indeed DEP of proteins was achieved in devices exhibiting electric field gradients not significantly differing to those manipulating large DNA molecules (Nakano et al., 2011; Regtmeier et al., 2010).

Furthermore, another theoretical approach was presented to assess nanoparticle's DEP property arising due to the presence of the EDL accounting for ion migration, convection, diffusion in the EDL as well as the electrophoretic particle motion based on Poisson-Nernst-Plank (PNP) equations (Zhao & Bau, 2009; Zhao, 2011a). Their results attributed a major contribution of the polarization to the total dipole moment due to electrophoretic motion within the thick EDL, which is significantly larger than the particle radius (Zhao & Bau, 2009). This model could predict the DEP mobility of large DNA adequately at low frequency (Zhao, 2011b), but was not extended to proteins yet.

This model indicates that a more complex mechanism is necessary to describe biomolecule DEP (here DNA) and will most likely be needed to fully describe frequency dependent protein DEP response.

Based on these aforementioned proposed mechanisms, a more complex relationship than developed for nanoparticles seems likely to be necessary to describe protein DEP, which should strongly depend on protein type and surrounding electrolyte. Unfortunately, there is currently no comprehensive study including a variety of proteins and experimental conditions to elaborate the mechanism of protein DEP in more detail. The experimental conditions as well as experimental setups studying protein DEP further differ significantly, making it difficult to draw generally applicable conclusions from these studies. Note that a detailed analysis and theoretical model of frequency dependent protein dipolar response was recently reported by Matyushov (Matyushov, 2012a, 2012b). In his work, Matyushov predicted a complex dipolar behavior taking into account intrinsic protein polarization, protein-water and long-range solvent polarization employing molecular dynamics simulations for selected proteins. Matyushov predicted negative DEP to occur for the protein ubiquitin over a large frequency range (Matyushov, 2012a, 2012b), while positive DEP was predicted for charged proteins such as cytochrome B and lysozyme (Matyushov, 2012a) in the MHz to GHz range. These results are interesting as they account for intrinsic DEP characteristics of proteins, which could be exploited for their guided manipulation.

I conclude that the dipolar response of proteins is complex and that equation (1. 6) and (3. 1) oversimplify protein polarization. Current models including details on the effects contributing to polarization in the EDL for nanoparticles should be extended to

estimate DEP forces exerted on proteins. These models based on non-conducting particles do not take into account structural influences of proteins on DEP or influences on the polarization due to the amphoteric nature of proteins. Theoretical frameworks such as the one developed by Matyushov (Matyushov, 2012a, 2012b) need to be extended to a larger pool of proteins to reveal scaling laws and more detailed predictions for DEP response. It is further necessary to relate the experimental investigations to the existing models in more detail. Future frequency dependent DEP studies on a larger variety of proteins should thus allow confirming the theoretically predicted dielectrophoretic response of proteins and eventually allow refining current theoretical models.

DIELECTROPHORETIC BEHAVIOR OF PROTEINS UNDER AC CONDITIONS

β-galactosidase and Immunoglobulin G iDEP Behavior at Low Frequencies. Subsequently, iDEP experiments were performed under AC conditions using the same nano-constriction iDEP device with an application of 100 and 500 V_{pp} for a 0.8 cm long channel. For these experiments the voltage applied to the device was an AC step function of frequencies ranging from 0 to 5 kHz. First, the results using the low frequency of 1 Hz are discussed for both β-galactosidase and IgG. *Figure 6-7* shows the representative fluorescence microscopy images of protein iDEP trapping at the positive and negative half cycles. For the positive half cycle, β-galactosidase was concentrated at the right side of the post, while the concentration was observed at the opposite side for IgG. Similar to the case under DC conditions, these concentration behaviors can be explained by the direction of the total force, namely DEP, EOF, and EP. For the positive half cycle at the

right hand of the post, EK points toward the nano-constriction, while nDEP is directed away from it, leading to the β-galactosidase concentration on the right side of the post. On the other hand, pDEP balances with EK at the left side of the post, thus IgG concentration occurs at the left side. These concentration behaviors were in accordance with the results under DC conditions where IgG and β-galactosidase were concentrated at the opposite sides of the posts due to positive and negative DEP, respectively.

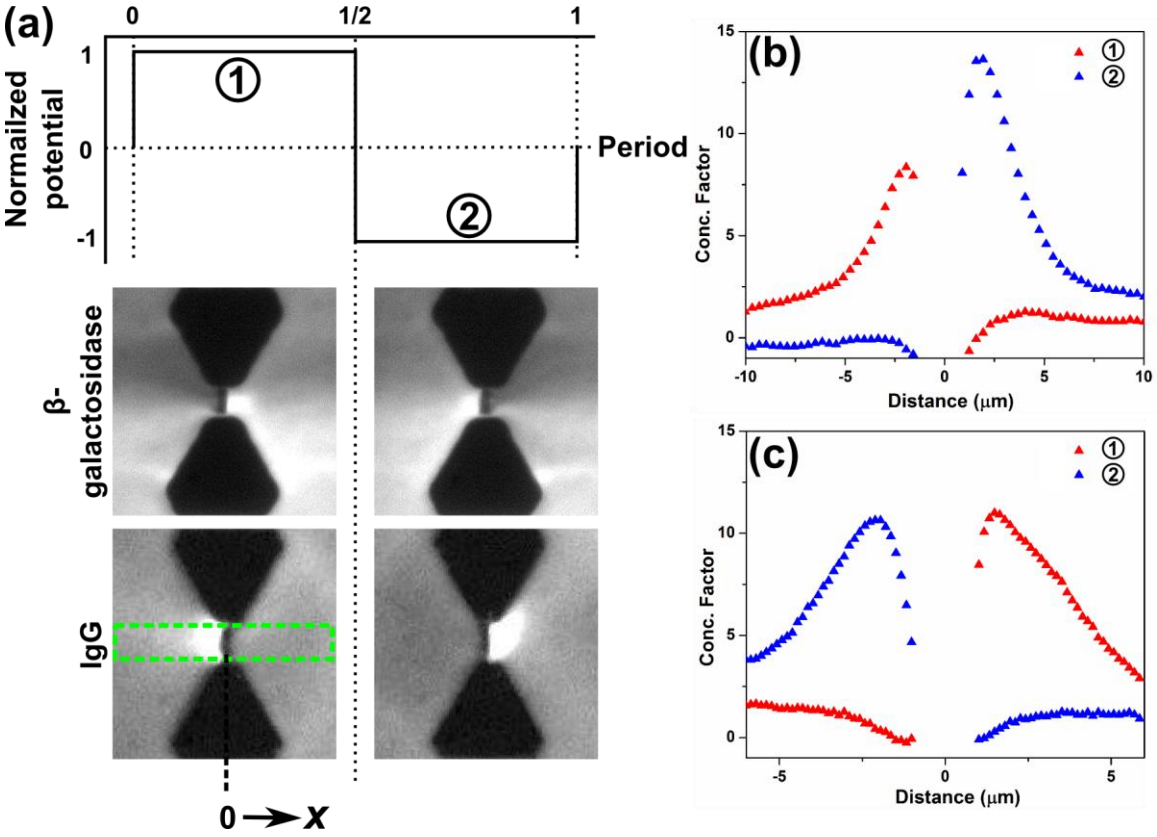

Figure 6-7. iDEP protein trapping at 1Hz voltage modulation with amplitude of 500 V for a 0.8 cm and 1.5 cm channel for β-galactosidase and IgG, respectively. (a) Fluorescence microscope images with an application of 1 Hz AC step function of 500 V_{pp}. At the positive half cycle, β-galactosidase is concentrated on the right side of the post, while IgG concentration occurs on the opposite side. At the negative half cycle, the region of each protein concentration changes the sides. (b-c)) Protein concentration profiles at the positive half cycle (red) and negative half cycle (blue) of (b) IgG and (c) β-galactosidase extracted from the concentration distribution at the regions perpendicular to the nanopost as highlighted with the green rectangle in (a). Fluorescence intensity is normalized with the intensity at the same region at 0 V.

Frequency Dependence. Subsequently, the frequency dependency on protein iDEP concentration was investigated. *Figure 6-8* shows the representative fluorescence microscopy images at frequencies of 5, 100, and 500 Hz, demonstrating the change in magnitude of protein concentration as well as the locations where the protein is concentrated. *Figure 6-8* reveals that there are two main locations of protein concentration: sides of the triangular microposts and the middle of the rectangular nanoposts. These locations correspond to the regions of the low electric field gradients, revealing that β-galactosidase exhibits nDEP. The observed frequency dependent concentration is expected to be caused by the combination of electrokinesis, DEP, and diffusion. At relatively low frequencies (e.g. 5 Hz, see *Figure 6-8*a) electrokinetic transport still prevails, thus proteins can move from one DEP trap to the other locations. This is evident from the stream-like patterns shown in *Figure 6-8*a, which is expected to occur due to the significant contribution of EK. On the other hand, when the frequency is increased to 100 Hz in *Figure 6-8*b, the protein concentration is more localized to the regions of low electric field gradient since particle transport via EK is decreased. As shown in *Figure 6-9*, the protein concentration decreases with increasing applied frequency and almost disappears at 5 kHz with 500 V_{pp} applied potential. Moreover, the protein concentration disappears at lower frequency than compared to 5000 Hz when 100 V_{pp} was applied (data not shown). This was unexpected finding since a higher concentration effect would be expected with increased frequency since EK is suppressed at high frequencies. The potential reasoning for this experimental observation is frequency dependent double layer polarization (Beltramo & Furst, 2012, 2013). At high frequencies, ions does not have time to be transported to the end of the particle, thus

double layer polarization declines while increasing the applied frequency. I can also potentially explain such frequency dependency with AC electroosmosis which exhibits frequency dependent velocity (N. G. Green, Ramos, González, Morgan, & Castellanos, 2000). Additionally, recently Wirth et al. reported electrolyte dependent particle motion arising from the polarization of the particle's diffuse layer, which affects the particle's electrophoretic mobility (Wirth, Sides, & Prieve, 2013). They also reported that the mobility is not only electrolyte dependent but also frequency dependent (Wirth et al., 2013), which can potentially explain the observed frequency dependent concentration effects.

This work demonstrated low frequency AC iDEP behaviors of IgG and β-galactosidase, revealing that the protein concentration is indeed strongly frequency dependent. The iDEP experiments performed in the range of 0.5 ~5 kHz showed that the β-galactosidase concentration decreases with increasing frequency and also β-galactosidase changes the regions of the concentration. Interestingly, at high frequencies around 5000 Hz, protein concentration effect ceased in contrary to our expectations. Protein iDEP with such low AC frequencies has not reported previously, thus further studies are needed to understand the observed AC iDEP behaviors.

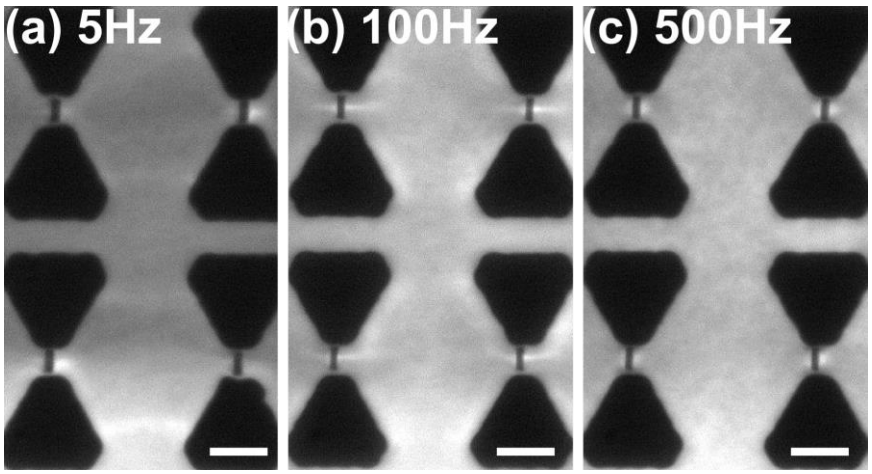

Figure 6-8. Fluorescence microscopy images of β-galactosidase concentrated due to negative DEP as a function of frequency (5, 100, and 500 Hz) at 500 V applied for a 0.8 cm channel. Scale bar is 10 μm.

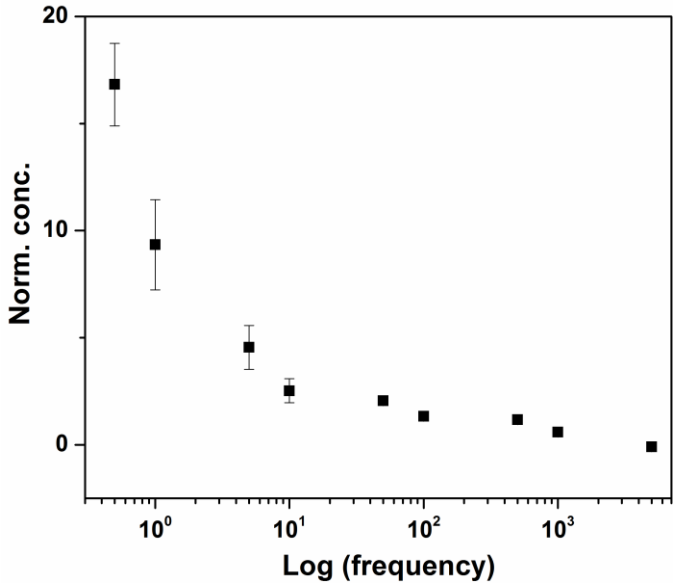

Figure 6-9. Normalized concentration factor of β-galactosidase as a function of frequency with an application of 500 V for a 0.8 cm long channel.

CHAPTER 7

TEMPORAL AND LOCAL TEMPERATURE VARIATION IN MICROFLUIDIC CHANNELS

INTRODUCTION

Dielectrophoresis (DEP) is a powerful technique often implemented in microfluidic platforms and has shown to serve as a versatile tool in many bioanalytical applications for cells, organelles, crystals, and biomolecules (B. G. Abdallah, Chao, Kupitz, Fromme, & Ros, 2013; Pethig, 2010; Voldman, 2006; Zhang et al., 2010). The analytical applications span a number of methods such as separation, fractionation, purification, pre-concentration, and sorting. DEP is referred as translational motion of a particle or biomolecule under the influence of an inhomogeneous electric field, which results in particle transport toward the region of high electric field gradient (positive DEP) or away from it (negative DEP). The electric field gradients necessary for the occurrence of DEP can be created by mainly two strategies. The most traditional approach is integrating microelectrodes on a substrate (Martinez-Duarte, 2012). The second and somewhat newer approach employs insulating topological structures within a microfluidic channel and is named insulator-based dielectrophoresis (iDEP) (Lapizco-Encinas & Rito-Palomares, 2007; Srivastava et al., 2011).

The application of iDEP has been demonstrated with a variety of designs including constrictions with various shapes (Hawkins, Smith, Syed, & Kirby, 2007; K. H. Kang, Kang, Xuan, & Li, 2006; Y. Kang et al., 2008), oil droplets (Barbulovic-Nad, Xuan, Lee, & Li, 2006), insulating post arrays with various geometries (Chou et al., 2002; Cummings, 2003; Gallo-Villanueva, Rodríguez-López, Díaz-de-la-Garza, Reyes-

Betanzo, & Lapizco-Encinas, 2009; Lapizco-Encinas, Davalos, Simmons, Cummings, & Fintschenko, 2005; Lapizco-Encinas et al., 2008a, 2004; Nakano et al., 2012, 2011; Regtmeier et al., 2007, 2010), sawtooth devices (Pysher & Hayes, 2007; Staton et al., 2012), and serpentine channels (Zhu, Tzeng, Hu, & Xuan, 2009). With iDEP devices, problems prevalent to electrode based DEP, such as electrode fouling and electrode reactions interfering with DEP can be eliminated in the regions where DEP occurs. Additionally, most of the iDEP experiments were performed under DC conditions where particles can be transported by electrokinesis, thus eliminating the need of hydrodynamic pumps.

Despite the aforementioned advantages over the electrode-based applications, iDEP requires relatively high applied potentials to create significant electric field gradients necessary to manipulate sub-micrometer particles or even biomolecules. The application of high electric fields leads to Joule heating which may result in temperature elevation within the device. Elevated temperatures can have detrimental influence on biological analytes of interest by affecting their viability, biological functionality, and/or stability. Moreover, one would expect a higher temperature rise at the regions of the localized electric field (e.g. constrictions) in iDEP devices due to the large electric fields necessary to manipulate sub-micrometer biological objects such as organelles or biomolecules. Arising temperature gradients may create an additional electrothermal flow interfering with DEP. For the aforementioned reasons most experimental iDEP studies have been performed with low conductivity buffers. Although some work has been reported with high conductivity buffers or even physiological buffers (Chaurey et al., 2012; Clarke et al., 2005; Liao & Chou, 2012; Liao et al., 2012), the direct influence of

Joule heating on samples has to be alleviated in some ways. Nevertheless, the degree of Joule heating mostly depends on the buffer conductivity, applied potential, device dimension, and insulating structure geometries. Therefore, for realization of iDEP as a reliable analytical tool, it is of extreme importance to monitor and control temperatures within the device.

A variety of methods have been employed to measure temperature in microfluidic devices, such as the popular use of thermocouples integrated in the device (T. Chen & Garimella, 2006; de Mello, Habgood, Lancaster, Welton, & Wootton, 2004; Lagally, Medintz, & Mathies, 2001; Lee, Garimella, & Liu, 2005). However, thermocouples only enable the assessment of the external temperatures, which may not match with the temperature within the channel. Unlike the externally attached thermocouples, resistive sensors inside the channel can determine the in-channel temperature (Jaeger, Mueller, & Schnelle, 2007). However, this method lacks the spatial resolution since the temperature can only be measured at the locations of resistors, thus not over an entire device geometry. Nuclear magnetic resonance (NMR) thermometry (Lacey, Webb, & Sweedler, 2000) was also employed to monitor the in-channel liquid temperature by measuring the proton resonance shift from water molecules. Although NMR thermometry provides a non-invasive approach to assess in-channel temperature, it also suffers from the low spatial resolution. Infrared (IR) thermography (Jaeger et al., 2007) is another technique to track the temperature, providing excellent longitudinal resolutions. However, IR thermography can only assess the temperature on the outer surface of the device.

High spatial temperature resolution can be achieved by addition of thermosensitive substances to the working solutions such as liquid crystalline probes

(Chaudhari, Woudenberg, Albin, & Goodson, 1998; Fujisawa, Funatani, & Katoh, 2005; Richards & Richards, 1998), semiconductor nanocrystals (Mao, Yang, & Cremer, 2002; S. Wang, Westcott, & Chen, 2002), and dyes with temperature dependent optical properties (Gielen, Pereira, deMello, & Edel, 2010; Ross, Gaitan, & Locascio, 2001; Ross & Locascio, 2002). Among those approaches, the use of thermosensitive dyes is popular due to its accessibility and cost-effectiveness. Rhodamine B (RhB) is the most commonly used temperature sensitive dye which exhibits strong temperature dependent fluorescence in the range of 0 ~ 100 ºC (Coppeta & Rogers, 1998). However, a serious issue arises when RhB is used for polymer-based devices such as poly(dimethylsiloxane) (PDMS), commonly used for microfluidic applications. Small hydrophobic analytes such as RhB are known to strongly adsorb on the PDMS surface and diffuse into the PDMS due to its hydrophobic nature (Mukhopadhyay, 2007). Such dye adsorption leads to the fluctuation of the baseline fluorescence intensity, resulting in false temperature reading.

A variety of approaches were attempted to overcome the RhB incompatibility with PDMS by modifying the PDMS surface properties. The main approaches were carried out by dynamic coating of PDMS with chemical agents such as a nonionic surfactant Triton X-100 at high concentrations (J. Kang et al., 2005), sodium dodecyl sulfate (Roman, McDaniel, & Culbertson, 2006), polybrene solution (Erickson, Liu, Venditti, Li, & Krull, 2005), a combination of ionic liquid and nonionic surfactant (Xu, Jiang, & Wang, 2007), and the immobilization of ~ 10 nm SO_2 particles onto the PDMS surface to prevent the dye diffusion into PDMS (Roman, Hlaus, Bass, Seelhammer, & Culbertson, 2005). The undesirable fluorescence signal derived from the adsorbed dye can also be distinguished from the dye in free solution and eliminated by using

fluorescence life time imaging (Robinson et al., 2009). Moreover, Samy et al.(Samy, Glawdel, & Ren, 2008) employed an assembly where thin PDMS saturated with RhB is sandwiched in between two glass slides. By introducing such assembly, RhB can be physically separated from the PDMS surface, therefore completely eliminating the adsorption problem.

Temperature changes for DEP applications have been investigated previously. While experimental measurements were reported for eDEP, Joule heating effects were not yet assessed experimentally in iDEP to the best of our knowledge. For example Jaeger et al. employed a variety of methods to measure the temperature change for cell handling in dielectrophoretic cages employing eDEP (Jaeger et al., 2007). Additionally, Otto et al. recently measured the *in-situ* temperature of an eDEP silicon based chip using RhB dye under AC conditions (Otto, Kaletta, Bier, Wenger, & Hölzel, 2014). In iDEP, several studies assessed temperature in iDEP devices with theoretical models. For example, Hawkins et al. investigated Joule heating and the effect of the resultant electrothermal flow in iDEP (Hawkins & Kirby, 2010). The influence of Joule heating on electroosmotic flow was discussed by Sridharan et al. where the temperature field was solved using numerical simulations (Xuan, 2008). Another example was performed by Chaurey et al. where temperature rise in a nano-constriction device was numerically simulated (Chaurey et al., 2013). Recently, Gallo-Villanueva et al. numerically simulated a temperature increase in PDMS iDEP devices (Gallo-Villanueva, Sano, Lapizco-Encinas, & Davalos, 2014).

In this work temperature is experimentally investigated via fluorescence thermometry using RhB dye for iDEP applications in PDMS/glass hybrid devices with

two methods. The first method enables in-channel temperature measurement by introducing a zwitterionic additive to the buffer in order to prevent RhB adsorption onto the PDMS microchannel surface. For the second method, the sandwich approach by Samy et al.(Samy et al., 2008) was adapted, where temperature was measured on a thin film of PDMS located about 150 μm below the iDEP channel. Results from both methods show similar temporal temperature variation trends, however, the sandwich method provides ~ 20 ºC smaller temperature change than the in channel measurement method. In addition, a numerical model is presented and showed excellent agreement with the experimental results. Furthermore, this temperature measurement technique was applied to the same conditions as previously employed to study iDEP behavior of mitochondria. Our study revealed that the temperature changes are marginal for low conductivity buffers and therefore the viability of mitochondria and other biological species is not significantly influenced through temperature variations in iDEP.

EXPERIMENTAL PROCEDURES

Chemicals and Materials. Si wafers (5 in.) were obtained from University Wafer. The negative photoresist SU-8 2007 and developer were purchased from Microchem (Newton, MA, USA). (Tridecafluoro-1,1,2,2-tetrahydrooctyl)dimethylchlorosilane (TDTS) was purchased from Gelest (Morrisville, PA, USA). Sylgard184, composed of the silicon elastomer base and the curing agent for poly(dimethylsiloxane) (PDMS) was obtained from Dow Corning Corporation (Midland, MI, USA). Rhodamine B, 4-(2-hydroxyethyl)-1-piperazineethanesulfonic acid (HEPES), poly(ethylene glycol)-block-poly (propylene glycol)-block-poly(ethylene glycol) (F108),

potassium hydroxide, sucrose, potassium phosphate monobasic, sodium phosphate dibasic, and 3-[(3-Cholamidopropyl)dimethylammonio]-1-propanesulfonate (CHAPS) were purchased from Sigma-Aldrich (St. Louis, MO, USA). Deionized water was supplied from a Synergy purification system (Millipore, USA).

Microchip Fabrication. As shown schematically in *Figure 7-1*, the microfluidic device has dimensions of 100 μm width and 10 μm height with triangular insulating post arrays integrated in the 1 cm long channel. The device was fabricated with standard photo- and soft lithographic techniques as described previously.(Nakano et al., 2011) Briefly, the master relief of SU-8 negative photoresist was patterned on Si wafer via photolithography, followed by PDMS casting on the master wafer. Subsequently, the cured PDMS mold was peeled off from the master wafer and 2 mm reservoir holes were manually punched at the both ends of the 1 cm long channel.

For in-channel temperature measurement experiments (method A), the resultant PDMS piece as well as a pre-cleaned 150 μm thick glass slide was treated with oxygen plasma (PDC-001 Harrick Plasma, Harrick, USA) for 60 s at the highest RF setting to obtain a tight seal. For temperature measurement experiments using a thin film of PDMS doped in RhB (method B), the previously reported experimental procedures were followed (Samy et al., 2008). Briefly, PDMS was first spin coated on a 1 mm thick glass slide at 3000 rpm for 60 s, resulting in an approximately 30 μm thick film. After polymerization, thin film PDMS was submersed into 1 mM RhB solution for 5 days in the dark to prevent photobleaching and was dried completely. To form a tight seal between the thin film PDMS/glass substrate and a 150 μm thick cover glass, both pieces were treated with oxygen plasma. The resultant substrate, where PDMS was sandwiched

between the glass slide and the cover glass, was plasma treated and bonded to the PDMS channel mold. A 5 mm thick PDMS slab with 5 mm diameter reservoir holes was pressed on the top of the device above the microchip reservoirs to enlarge the reservoirs. Pt electrodes attached to both reservoirs were connected to a high voltage power supply (HVS448 6000V, LabSmith, CA) to apply DC voltages.

Mitochondria iDEP Experiments. After assembly, the microfluidic channels were immediately filled with Buffer A (1 mM F108, 10 mM HEPES, pH adjusted to 7.2 ~ 7.4 with KOH) by capillarity and the chip was placed in a humid environment overnight. Then buffer A was removed by vacuum suction, and the channels were washed with Buffer B (10 µg/mL RhB, 25 mg/mL CHAPS and 250 mM sucrose dissolved in Buffer A) three times and refilled by adding Buffer B to the outlet reservoirs. The conductivity of buffer B is ~300 µS/cm. A potential of 3000 V was applied for a 1cm long channel for the iDEP experiments using mitochondria.

Temperature Measurement Experiments with iDEP Devices. For method A the assembled iDEP channel was filled with the desired buffers. Three different buffers were tested: pH 8 phosphate buffers at conductivities of 100 µS/cm and 1 mS/cm with 10 µg/mL RhB and 25 mg/mL CHAPS added and Buffer B at 300 µS/cm to examine the temperature rise under the same conditions used in mitochondria iDEP experiments. To each buffer 10 µg/mL RhB and 25 mg/mL CHAPS were added. For method B the iDEP channel was filled with the buffer after assembly. To compare with the result from method A the phosphate buffers at the same conductivities (100 µS/cm and 1 mS/cm) was used. For both method A and B fluorescence intensities were recorded upon the application of potentials between the inlet and outlet. For each applied potential

experiments were repeated three times to test reproducibility. For each trial a single nominal temperature value was calculated by averaging the temperature from the entire channel within the image. The average temperature values from three trials were plotted as a function of duration of potential application.

Temperature Calibration. To determine the correlation between the fluorescence intensities of RhB and the corresponding temperature change, the following experiments were performed for each temperature measurement methodology. For the in-channel temperature measurement experiment (method A) fluorescent intensities at various temperatures were measured within a 1 cm diameter chamber for temperature calibration. A Ni-Cr alloy wire (Omega, CT, USA) was embedded inside of the PDMS surrounding the chamber to control the temperature by resistance heating. A solution containing 10 µg/mL RhB dissolved in pH 8 phosphate buffer with a conductivity of 100 µS/cm was freshly prepared and filtered through a 0.22 µm syringe filter prior to use. The PDMS chamber containing 1 mL of this buffer was heated by supplying current through the resistive wire. The temperature change was monitored using a K-type thermocouple probe (Omega, CT, USA) in specific increments. For each increment fluorescence intensity was recorded after a constant temperature was reached.

For the method employing the RhB saturated PDMS thin film (method B), the resistive heating wire was directly embedded onto the RhB doped PDMS thin film to control the PDMS surface temperature. The K-type thermocouple probe was attached onto the PDMS to assess the surface temperature. For both methods, images were acquired at various temperatures from room temperature up to ~ 90 ºC. For the calibration curve, fluorescent intensity measured at each temperature was normalized

with the intensity measured at room temperature. The resultant data sets (normalized intensity vs. temperature) were fitted with a third order polynomial, as was previously performed for temperature measurement with RhB (Ross et al., 2001).

Detection and Data Analysis. RhB fluorescence intensity was recorded either in the microchannel (method A) or in a sandwiched thin PDMS layer underneath the microchannel (method B). For fluorescence microscopy imaging, an inverted microscope (IX 71, Olympus, USA) with a 40x objective (Olympus, USA), a mercury burner (U-RFL-T, Olympus, USA), and an appropriate fluorescent filter set (Olympus, USA) containing a 531/40 nm exciter, 562 nm dichroic, and 593/40 nm emitter was used. Throughout the experiments, two neutral density filters of 12 and 25 % were used in order to reduce the excitation light from the source. In addition, sample exposure to the incoming light was controlled by using an automatic shutter (Prior scientific, MA, USA) in order to minimize photobleaching of the dye. Images were acquired at 10 ms/frame for the calibration experiments and 100 ms/frame for the measurement in the microfluidic devices using a CCD camera (Quantum 512 SC, Photometrics, USA) and Micro-Manager software (University of California, USA). Resultant images were analyzed with Image J software (version 1.43).

RESULTS AND DISCUSSIONS

The quantification of temperature changes in iDEP experiments is important, specifically for biological species such as cells and their organelle constituents or for iDEP with biomolecules. These biological entities could be degraded, altered, deactivated or form aggregates upon exposure to high electric fields and thereof arising temperature

increases. For small species, such as biomolecules, specifically proteins and organelles such as mitochondria, large potentials in the order of several hundred up to a few thousand Volts are typically applied in iDEP streaming and trapping. For example, numerical simulations performed previously by our group showed that the magnitude of the electric field in iDEP application can reach up to 10^6 V/m and corresponding electric field gradients amount in as high as 10^{17} V^2/m^3 (Camacho-Alanis et al., 2012).

A typical iDEP structure is schematically shown in *Figure 7-1*. In the past iDEP experiments were performed with biomolecules such as DNA (Gan, Chao, Camacho-Alanis, & Ros, 2013) and proteins (Nakano et al., 2012, 2011) with similar structures and more recently studied the iDEP behavior of cell organelles such as mitochondria in similar devices. *Figure 7-1*b provides a top view of the iDEP regions where the DEP force acts on particles in the presence of inhomogeneous electric fields created by the triangular insulating posts.

*Figure 7-1*c shows a snapshot of the iDEP trapping of semimembranosus muscle mitochondria under DC conditions in a triangular post device. These experiments were carried out at a medium pH of ~ 7.4 and 300 µS/cm conductivity (Luo, Abdallah, Wolken, Arriaga, & Ros, 2014). Mitochondria were fluorescently labeled with MitoTracker Green to enable the visualization under a fluorescence microscope. As shown in *Figure 7-1*c, we observed negative DEP of mitochondria under DC conditions with the application of 3000 V for a 1cm channel. The mitochondria showed three different modes of iDEP, related to wiggling in-between posts, trap hopping or iDEP trapping. Such effects could arise due to aggregates of mitochondria exhibiting different DEP properties than the single mitochondrion. The formation of aggregates might be

triggered by temperature increases under iDEP operation. In the following temperature changes are thus assessed related to DC iDEP applications. Experimental observations are compared with numerical simulations and two different methods are tested to measure temperature.

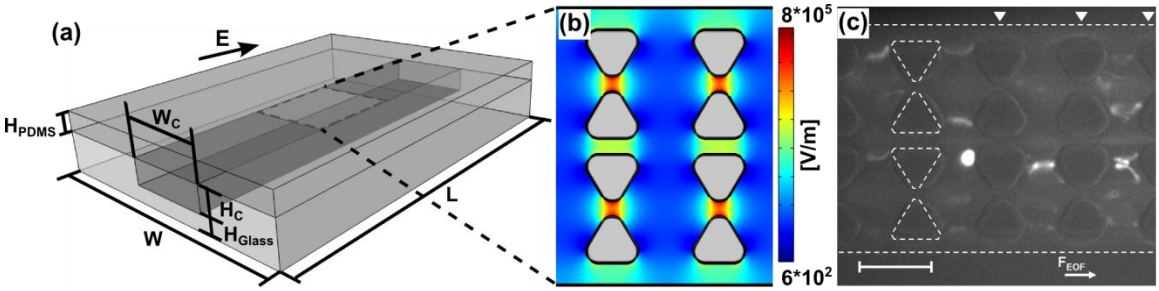

Figure 7-1. Schematic of the iDEP device, the produced electric field distribution, and fluorescence microscopy image of mitochondria DEP. (a) Schematic of the iDEP microfluidic device (not to scale). Arrow represents the direction of applied electric field (***E***). Sizes shown are the actual device dimensions (without reservoirs for simplification) used for the experiments and applied to the numerical modeling. The dimensions are the following: L (device length) = 1 cm, W (device width) = 2 cm, W_c (channel width) = 100 µm, H_c (channel depth) = 10 µm, H_{glass} (thickness of the bottom glass slide)= 150 µm for method A and 1 mm for method B, and H_{PDMS} (thickness of the top PDMS wall)= 0.5 mm. (b) Numerically simulated electric field distribution at 3000 V/cm inside of the channel where the insulating triangular posts are integrated to create an inhomogeneous electric field necessary for DEP.(c) The result of mitochondria DEP experiment, providing a fluorescence microscopy image of mitochondria obtained under DC conditions at 3000 V/cm. White dash lines indicate the edges of the channel and that of a row of posts, and the other rows of posts are indicated by triangles. Scale bar is 30 µm. As shown in the figure, mitochondria were either wiggling in-between adjacent rows of posts or trapped at the edges of posts, which could be caused by electroosmotic flow, electrophoretic force, and negative DEP force on mitochondria.

Calibration of the Temperature Dependent Dye. The temperature dependent fluorescence of RhB dye was utilized to probe temperature within the iDEP device. RhB was selected since it is known to have a highly temperature dependent quantum yield in a wide temperature range (0 ~ 100 ºC), while it is insensitive to pH changes over a solution pH above 6 (Coppeta & Rogers, 1998). The latter point is important especially when

using low ionic strength buffers commonly used in iDEP applications since the buffers are susceptible to the pH change within the order of ~ 10 min under the application of large electric fields (Gencoglu et al., 2011).

First, a calibration curve was constructed to determine the dependency of fluorescence intensity on temperature. As described in the Method section, two methods were examined: method A to measure temperature in a microfluidic channel and method B where temperature measurements were carried out with a thin PDMS film sandwiched between two glass slides slightly below the iDEP channel (see *Figure 7-2*). Therefore, each method required a separate temperature calibration. For method A, RhB was directly added to the working solution and its temperature dependent fluorescence intensity was measured in a large chamber (1 mL in volume) where the solution temperature was carefully controlled. For method B, a thin layer of PDMS was first spin coated on a glass slide and cured to form a thin film. Subsequently, the PDMS film was saturated with RhB dye by immersing it in 1 mM RhB dye solution. The calibration experiment for method B was performed by directly heating the thin PDMS film and measuring the fluorescence intensities at various temperatures.

For both methods, the resulting fluorescence intensities measured at each temperature were normalized to 25 ºC and plotted as a function of temperature as shown in *Figure 7-3*. Square markers and triangular markers show the sets of data points obtained from method A and B, respectively. The resultant calibration curve is shown with corresponding polynomial fits for method A (blue) and B (red). I confirmed that the temperature dependent fluorescence occurs reversibly by performing the calibration experiment with increasing as well as decreasing temperature. Both calibration curves

were similar to the previously reported results by Ross et al. (Ross et al., 2001) for the in-channel calibration curve and Samy et al. (Samy et al., 2008) for the thin-film calibration.

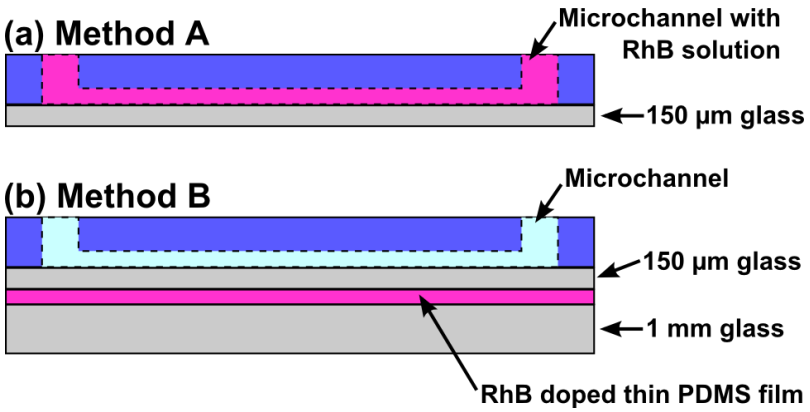

Figure 7-2. Schematic representation of two methodologies employed to measure temperature in iDEP microfluidic devices. The 2D schematics correspond to the cross-section view of the iDEP device shown in *Figure 7-1* (not to scale). (a) In method A, the channel (dotted line) is filled with the RhB containing buffer (pink). (b) In method B, a thick and thin glass slide sandwich the RhB doped thin PDMS film located 150 µm below the channel. Channel is filled with the desired working buffer which does not contain RhB (light blue).

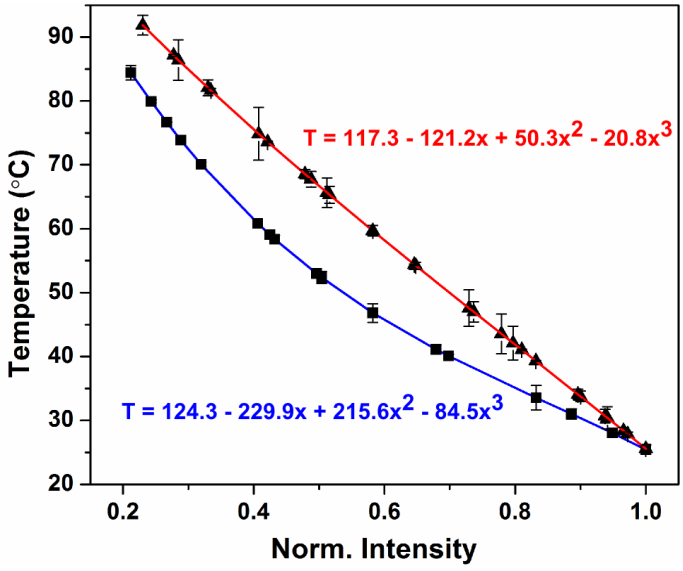

Figure 7-3. Normalized fluorescence intensity plotted as a function of temperature to calibrate the temperature dependent fluorescence of RhB. Both sets of data obtained from method A (■) and B (▲) are fitted with a third polynomial as indicated in the graph.

The Choice of Buffer Additive for In-channel Temperature Measurements.

Using the aforementioned calibration curves, the temperature change within our iDEP device due to Joule heating can be measured by monitoring the fluctuation of the fluorescence intensity. First, the in-channel temperature measurement was performed by adding RhB dye to the working buffer. Note that RhB is known to be incompatible with the hydrophobic PDMS surfaces on which RhB tends to get strongly adsorbed (Mukhopadhyay, 2007). Indeed, when using the unmodified PDMS an increase of the baseline fluorescence intensity was observed even without applying potential, which is translated to a temperature decline below room temperature. Since this is physically highly unlikely, this is assumed to be caused by RhB adsorption onto the PDMS surface. The amount of the adsorbed dye increases over time and the adsorption kinetics can vary depending on the conditions in the channel (e.g. temperature) (J. D. Wang, Douville, Takayama, & ElSayed, 2012). Therefore, the dye adsorption onto the PDMS surface is difficult to quantify and can consequently lead to false temperature reading.

However, when adding the zwitterionic surfactant CHAPS, the RhB adsorption was greatly suppressed. For further testing, a series of dye adsorption experiments was performed using various CHAPS concentrations within a large PDMS chamber similar to the ones used for the calibration experiment. These experiments showed that the chemical modification of the PDMS surface via CHAPS dynamic coating above its critical micelle concentration (CMC) significantly suppresses the dye adsorption onto the PDMS (data not shown). Although it has been previously demonstrated that the chemical modification of PDMS reduces RhB adsorption (J. Kang et al., 2005; Roman et al., 2006), the use of CHAPS as a surface modification agent has not been reported to the best of our

knowledge. Using CHAPS as a surface modification agent has several advantages for iDEP applications. First, CHAPS is known to improve protein solubility in bioanalytical applications (Hjelmeland et al., 1983) and has already been used for iDEP applications as an additive to reduce protein aggregation (Nakano et al., 2011). Moreover, owing to the zwitterionic nature of CHAPS, addition of CHAPS does not significantly change the overall buffer conductivity. The latter point is important since relatively low conductivity buffers are commonly used for iDEP experiments and thus increasing buffer conductivity would lead to larger Joule heating effects (see below).

In-channel Temperature Measurements (Method A). First, in-channel temperature measurements were performed by monitoring the fluorescence intensity fluctuation with addition of 25 mg/mL CHAPS and 10 μg/mL RhB in the same working buffer used for the mitochondria DEP experiment. Note that the severe photobleaching of the dye can lead to large intensity variations, thus sample exposure to the incoming light was minimized by using an automated shutter. Additionally, the extent of photobleaching was assessed prior to the temperature measurement experiments by acquiring an image sequence without applying a potential. Since the intensity fluctuations fall within the error obtained from the calibration measurements, I concluded that the contribution of photobleaching to the overall fluorescence intensity is negligible with this approach.

Subsequently, the maximum potential used for the mitochondria DEP experiments (3000 V for a 1cm channel) was applied to study the maximum temperature rise within the channel. Figure 7-4 shows the temperature surface plot at time t after the initiation of the potential application. These four images at t = 22, 102, 222, and 322 s show the temperature evolution within the channel, revealing that the in-channel temperature

reaches the steady temperature of ~ 34 ºC in ~ 3 min since the amount of the generated heat in the system becomes equal to the dissipated heat to the surroundings.

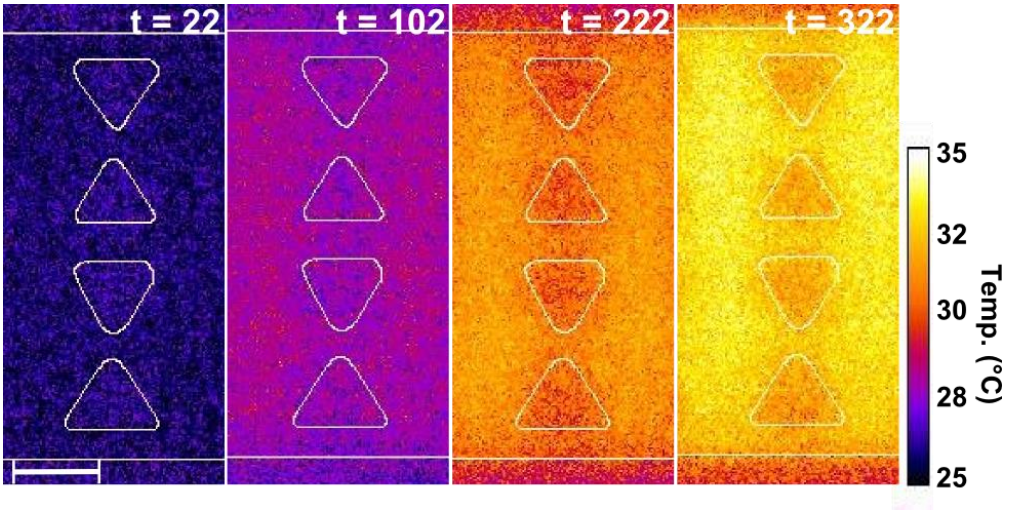

Figure 7-4. Temperature surface plot at various times after applying a DC potential of 3000 V for a 1 cm channel. Temperature evolution within the iDEP channel reveals that the temperature does not exceed 34 °C. White lines indicate the edges of the channel and that of triangular insulating posts. The scale bar is 20 µm.

The temperature measurement was subsequently performed within the channel at a conductivity of 100 µS/cm and 1 mS/cm prepared with phosphate buffer. Since these two conductivities are in the range of commonly used iDEP buffers, it is worthwhile to exploit the temperature change with these conditions. Our iDEP device was filled with each conductivity buffer containing 25 mg/mL CHAPS and 10 µg/mL RhB and three different potentials (100 V, 1000 V, and 3000 V) were tested for a 1cm channel. *Figure 7-5*a-b show the in-channel temperature plotted as a function of duration of potential application. In theory, larger Joule heating is expected by the enhanced current density due to the localized high electric fields between the tips of the triangular posts. However, the observed spatial temperature variation in the vicinity of the insulating post regions is less than the temperature resolution of 1 ºC estimated from the standard deviation of

residuals from the polynomial fit. Furthermore, as shown in *Figure 7-5*a, the temperature increases less than 5 ºC when using the 100 µS/cm conductivity buffer even with the application of the highest potential (3000 V). Significant temperature increase up to ~70 ºC (*Figure 7-5*b) was observed only when using 1 mS/cm buffer with the highest potential of 3000 V. *Figure 7-5*a-b also show the temporal temperature transition, demonstrating that it takes longer to reach a steady state temperature for larger applied potentials. For example, in case of 3000 V with 1 mS/cm conductivity buffer, the temperature equilibrates at ~ 70 ºC after 150 sec of potential application, while it takes only 5 sec in the case of 1000 V with 1 mS/cm buffer. The small absolute temperature changes of ~ 2 ºC in the case of 100 µS/cm conditions are within the range of the experimental error (*Figure 7-5*a). The experimental method thus does not allow resolving the temporal temperature changes in this case.

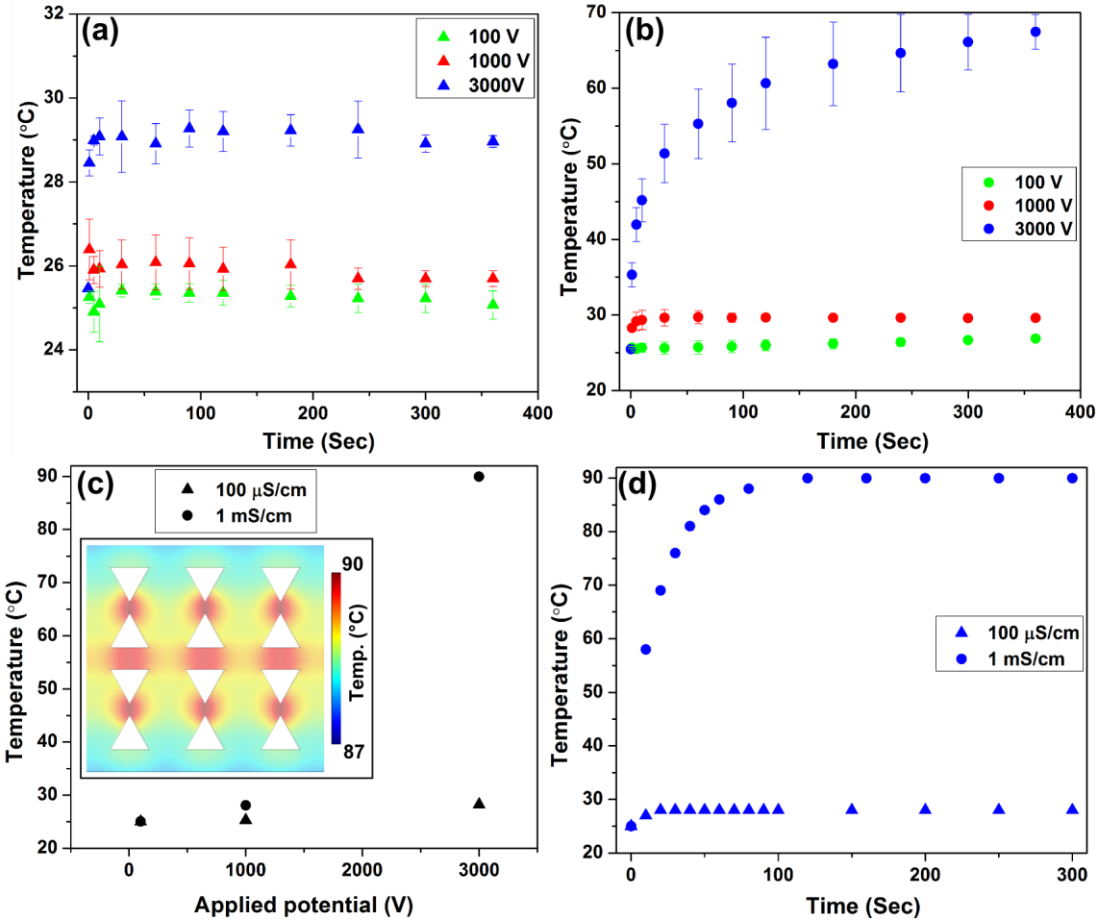

Figure 7-5. Experimentally and numerically obtained temperature resulted from Joule heating inside of the iDEP channel, tested with various conductivities and applied potentials. (a-b) Experimentally measured temporal temperature variations using a phosphate buffer with conductivity of (a) 100 µS/cm (~0.6 mM) and (b) 1 mS/cm (~5 mM). Three different potentials were tested for each conductivity of 100 µS/cm (triangles) and 1 mS/cm (dots): 100 V (green), 1000 V (red), and 3000 V (blue) for a 1cm long channel. (c) Numerical simulation results showing the steady state temperatures as a function of applied potential for the buffer conductivity of 100 µS/cm (triangles) and 1 mS/cm (dots). Inset shows the spatial temperature variations, revealing that the temperature variation is ~1.5 ºC within the channel. (d) Temporal temperature variations obtained numerically for 100 µS/cm (triangles) and 1 mS/cm (dots) when 3000 V is applied.

To support the experimental results presented above, numerical simulations were performed to model the Joule heating inside of the channel. First, steady-state simulations were performed to study the temperature reached with each set of conductivities and

applied potentials. As shown in *Figure 7-5*c, the temperature rise is less than 5 ºC for all cases except when 3000 V is applied with 1 mS/cm conductivity where the temperature increases significantly up to ~90 ºC. The absolute temperature increase was in excellent agreement with the experimental results at 100 V and 1000 V, however deviated by about 20 ºC for 3000 V applied at 1 mS/cm buffer conductivity. This discrepancy is attributed to the increase in RhB adsorption onto the PDMS at exceptionally high temperatures since adsorption kinetics is enhanced with increasing temperature. Additionally, the spatial temperature changes were investigated in the iDEP post regions. The temperature variation was negligible for the low conductivity and low applied potentials. The numerical simulation result with 1 mS/cm at 3000 V however shows that the highest temperature was obtained between the tips of the posts and the overall temperature varies spatially by ~ 1.5 °C (see inset of *Figure 7-5*c). This variation could not be detected in experiments, since the numerically obtained temperature variations fall within the experimental error.

Subsequently, the temperature transitions during the potential application were investigated by performing time dependent simulations. *Figure 7-5*d provides the resultant temporal variations in temperature with the highest applied potential (3000 V) for 100 µS/cm and 1 mS/cm conductivity. The saturation temperature of ~ 90 ºC is higher than the experimentally obtained temperature of ~70 ºC (see *Figure 7-5*b), similar to the steady state case (*Figure 7-5*c). Again, this discrepancy with measured temperatures can be attributed to the enhanced RhB adsorption at elevated temperatures. Moreover, I found that the numerical simulation also depends strongly on the chosen heat transfer coefficient value (*h*), which in turn greatly depends on the surrounding environment (i.e.

air flow rate). Especially for larger temperatures, this factor can affect absolute temperature changes in the order of 10 ºC (See Appendix C 1). Nonetheless, we found that the kinetics of both experimental and simulation results are in agreement. In case of the low conductivity buffer, temperature equilibrates within a short period of time (< 20 s), while it takes much longer (~ 150 s) with the high conductivity buffer.

Thin-PDMS Film Temperature Measurement (Method B). The temperature measurement in the iDEP device was performed by using the thin-PDMS film methodology exploited previously.(Samy et al., 2008) The experiment was performed using the 100 µS/cm and 1 mS/cm buffer. However, no RhB or CHAPS were added to these buffers. The change in fluorescence intensity was recorded for each applied potential (100 V, 1000 V, and 3000 V) and analyzed similarly to the previous in-channel experiment. The resulting temperature variations experimentally measured in the film located 150 µm below the channel reveal a large temperature rise up to ~ 49 °C only when using 1 mS/cm conductivity at 3000 V (see in *Figure 7-6*a-b). In contrast, the temperature increase is less than 2 °C for the lower potentials (100 and 1000 V) with 1 mS/cm as well as all potentials tested with 100 µS/cm.

Next, the numerically obtained temperature transitions were also compared to the experimental results for method B. The temperature values were obtained 150 µm below the channel from the same numerical model as the in-channel cases however with a geometry adapted to the sandwich method. For simplicity, a 1.15 mm thick glass composite at the bottom of the channel was employed in the simulation domain instead of the sandwiched assembly. *Figure 7-6*c demonstrates the temporal temperature variation with 100 µS/cm and 1 mS/cm conductivity at 3000 V, revealing that the numerical model

resulted in slightly lower values than the experiments. The largest discrepancy between the experimentally measured and numerically obtained temperatures on the film was found with 1 mS/cm conductivity at 3000 V as the steady temperature of ~ 45 °C numerically, while ~ 49 °C experimentally. This small inconsistency between the experiment and simulation can be explained with deviations in the actual heat transfer coefficient value (see above) or from the simplified geometry used in the numerical simulation assuming a single thick glass layer (and not the glass/thin-PDMS sandwich). Despite the discrepancy, the numerical simulation generally captures the trend presented by experiments such as the time frame to reach the steady state temperature (~ 150 sec). Moreover, the same numerical model allows the estimation of in-channel temperatures which resulted in 3 ~ 4 °C higher than the temperature in the film (see *Figure 7-6*c).

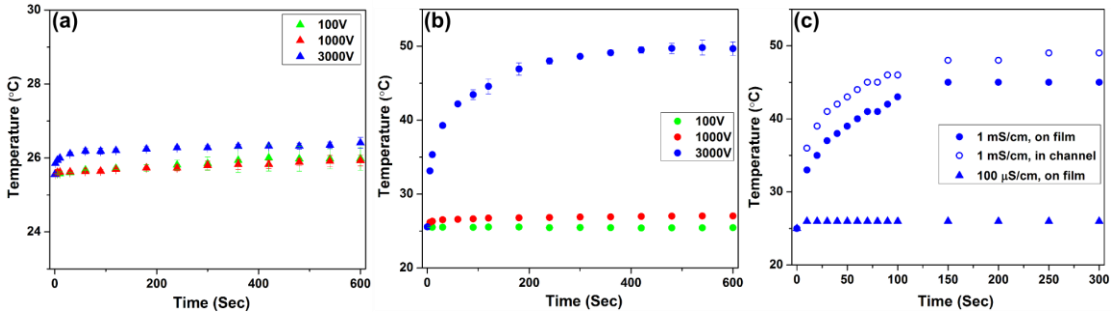

Figure 7-6. Experimentally and numerically obtained temperature resulted from Joule heating with various conductivities and applied potentials. Temperature was measured on thin PDMS film located ~150 µm below the iDEP channel. (a-b) Experimentally measured temporal temperature variations using a phosphate buffer with conductivity of (a) 100 µS/cm (~0.6 mM) and (b) 1 mS/cm (~5 mM). Three different potentials were tested for each conductivity: 100 V (green), 1000 V (red), and 3000 V (blue) for a 1cm long channel. (c) Temporal temperature variations obtained numerically for 100 µS/cm (triangles), 1 mS/cm on the film (filled circles), and in the channel (non-filled circles) when 3000 V is applied.

Comparison of the Two Approaches for Temperature Measurements. The two temperature measurement methods (method A and B) can be used complimentarily depending on the circumstances. Method A enables the direct temperature measurement within the iDEP channel. Moreover, the measurement of temporal and spatial variations is possible with this method. However, when employing the in-channel method, to circumvent the issue of RhB dye adsorption onto the PDMS surface, it is necessary to use an additional surfactant such as CHAPS as additive to buffers used for iDEP experiments. As seen in *Figure 7-5*a-b (method A) and *Figure 7-6*a-b (method B), larger errors are found using method A, which could be attributed to fluorescence intensity fluctuations due to largely reduced but still not entirely suppressed dye adsorption onto the PDMS even with the addition of CHAPS. Adsorption of RhB onto the PDMS surface increases the baseline fluorescence intensity, leading to underestimated temperature values as indicated by a comparison to the numerical simulations especially at exceptionally elevated temperatures. On the other hand, for method B the incompatibility issue of RhB and PDMS is overcome by physically separating RhB from the channel walls with a 150 μm thick glass slide. Moreover, the thin film method could be used in parallel with the iDEP experiment when the set up allows detecting dual fluorescence from sample analytes and RhB dye even though the temperature can be only measured at 150 μm below the channel.

As a result of the numerical simulations, the temperature increase was found to be marginal for all the conductivity and potential cases using both method A and B except when the highest potential of 3000 V was applied at 1 mS/cm conductivity. In this case, the temperature increased up to ~ 90 ºC with method A and ~ 45 ºC in the film located

150 µm below the channel with which the in-channel temperature can be estimated to be ~49 ºC by numerical simulation. Experimentally, the results from both methods are in excellent agreement with the numerical simulation for potentials < 1000 V and low conductivity, showing marginal temperature increases. Only in the case of 3000 V at 1 mS/cm conductivity the temperature changed significantly. In this case, method A resulted in the saturation temperature of ~ 70 ºC as obtained from experiments, whereas ~ 49 ºC was measured using method B experimentally. Note both experimentally and numerically temperatures obtained by method A are higher than the temperature measured using method B. This might be caused by the difference in thickness of the bottom glass slides employed in the two methods (i.e. 150 µm in method A and 1 mm for method B). I assume that the heat dissipation is enhanced with the thicker glass slide (method B) with the conditions employed in the study, leading to the lower saturation temperature. Furthermore, the time to reach the steady state is similar for both methods. For example, the system takes ~ 150 s to reach the saturation temperature in the case of 1 mS/cm at 3000 V using both methods (see *Figure 7-5*b and *Figure 7-6*b), indicating that the time scale to reach the steady state is similar for both within the channel and in the film.

Additionally, the temperature change was assessed under the same conditions where mitochondria iDEP was performed. Our results demonstrated that the in-channel temperature does not exceed 34 ºC in iDEP experiments considering the application of an extreme potential as high as 3000 V. Thus, it is expected that the mitochondria viability is not significantly affected by Joule heating during iDEP experiments and thus viable mitochondria can be subsequently used for further analysis in other assays. Our work also

shows conditions under which degradation of biomolecules is little affected by temperature changes.

Apart from biomolecules and bioparticle degradation Joule heating can also create electrothermal flow interfering with DEP. In the past, numerical simulations were performed to assess the temperature change due to Joule heating in iDEP devices as well as to evaluate the effect of electrothermal flow on DEP (Hawkins & Kirby, 2010). Chaurey et al. numerically simulated the temperature change within a nano-constriction iDEP device and found that the temperature increased up to 43.4 ºC with application of 350 V/cm field at the 100 nm constrictions using 1 S/m conductivity buffer (Chaurey et al., 2013). In another example, Sridharan et al. reported 52 ºC temperature enhancements with 470 µS/cm conductivity buffer with 600 V/cm (Xuan, 2008). A larger temperature increase of 71 ºC was reported by Gallo-Villanueva et al. at conductivity of 100 µS/cm under an application of 750 V/cm in an iDEP device (Gallo-Villanueva et al., 2014).

As demonstrated in these examples, the degree of Joule heating mainly depends on the buffer conductivity, applied potential, device dimension, insulating structure geometries, and the microchannel material. Our experimental temperature measurements fall in the range of these previously reported theoretical studies. The direct comparison of temperature measurements with the numerical simulations as presented in this study shows excellent agreement for all cases and is still reasonable for 1 mS/cm and the largest applied potential. I thus postulate that the presented approach is robust and can be used for a variety of iDEP applications in the future.

SECTION CONCLUSIONS

In this study, the temperature change was experimentally quantified in iDEP devices, which occurs due to Joule heating upon application of high electrical potentials. For an assessment of the arising temperature variations, the thermosensitive optical property of RhB was utilized by monitoring its temperature dependent fluorescence intensities. Two measurement methods were applied and evaluated experimentally: directly in the microfluidic channel and slightly below in a thin film. With the former method, in-channel temperature measurement becomes possible in iDEP devices with temporal and spatial resolution with the addition of the surfactant such as CHAPS used in this study to prevent RhB adsorption onto the PDMS surface. With this in-channel method the incompatibility issue of RhB and PDMS is greatly reduced and the experimental results showed excellent agreement with the numerical simulations. Only at larger conductivity (1 mS/cm) and applied potential (3000 V) the experimental results start deviating from the numerical models. The second method employing thin RhB saturated PDMS film underneath the microchannel showed similar temporal trends than the in-channel methods, however absolute temperature changes were smaller both experimentally and numerically. The thicker glass layer is thus advantageous to reduce temperature increases due to Joule heating in iDEP devices under the conditions employed in our protein and mitochondria iDEP studies. Moreover, this method will allow for elegant iDEP studies with fluorescent analytes, while observing temperature changes with adequate fluorescence optics simultaneously.

The two temperature measurement methods investigated in this work are easy to implement in iDEP microfluidic devices and complimentary. In summary, our study

provides useful guidelines for experimental temperature determination in iDEP devices which allows assessing Joule heating effects in future iDEP applications but also provides suitable numerical methods to estimate these changes prior to iDEP experiments with precious biological samples.

CHAPTER 8

SUMMARY AND CONCLUSIONS

In summary, successful iDEP-based manipulations of proteins was demonstrated with different geometries in a PDMS-based microfluidic system. Our iDEP device design ranges from devices with various geometries of topological micropost array for which the fabrication processes only require equipment for standard photo- and soft lithography, to the nano-constriction devices for which the implementation of FIBM as an additional step is required. In the case of micropost array devices, positive DEP behavior was demonstrated using diagnostically relevant IgG and BSA proteins resulting in locally concentrated streamlines, which were confirmed theoretically by performing numerical simulations. Both numerical simulation and the experiments show excellent qualitative agreement. Moreover, this work demonstrates that protein aggregation readily occurs using low conductivity phosphate buffers without the use of additives. These protein aggregates exhibit a different behavior (i.e. DEP trapping) as opposed to individual proteins in presence of a surfactant, CHAPS. Our results indicate the potential for manipulation of biomolecules with molecular dimension smaller than 10 nm, thus highlighting the ability to manipulate proteins using DEP. Specifically, streaming DEP demonstrated the ability to concentrate proteins within a microfluidic device, thus providing an exciting new tool for protein analysis devices in microfluidic format.

Furthermore, a detailed investigation of factors influencing DEP of IgG molecules was demonstrate using insulator-based DEP under DC conditions. The pH range in which concentration of IgG due to streaming iDEP occurs without aggregate formation was found to match the pH range suitable for immunoreactions (pH 6 ~ 8). Numerical

simulations of the electrokinetic factors pertaining to DEP streaming in this range further suggested that the protein charge and electroosmotic flow significantly influence iDEP streaming. These predictions are in accordance with the experimentally observed pH-dependent iDEP streaming profiles as well as the determined IgG molecular properties. Moreover, a transition in the streaming behavior caused by a change from positive to negative DEP was observed. This transition is expected to occur through micelle formation and the experimentally observed protein concentration showed excellent qualitative agreement with numerical simulations. Our study thus relates molecular immunoglobulin properties to observed iDEP, which will be useful for the future development of protein pre-concentration or separation methods based on DEP.

Another factor which can influence protein iDEP is temperature rise in iDEP devices due to Joule heating. In this regard, the temperature change in iDEP devices was experimentally quantified for the first time to the best of our knowledge. For an assessment of the arising temperature variations occurring due to Joule heating upon application of high electrical potentials, the thermosensitive optical property of RhB was utilized by monitoring its temperature dependent fluorescence intensities. Two measurement methods were applied and evaluated experimentally: directly in the microfluidic channel and slightly below in a thin film. With the former method, in-channel temperature measurement becomes possible in iDEP devices with temporal and spatial resolution with the addition of the surfactant such as CHAPS used in this study to prevent RhB adsorption onto the PDMS surface. With this in-channel method the incompatibility issue of RhB and PDMS is greatly reduced and the experimental results showed excellent agreement with the numerical simulations. Only at larger conductivity

(1 mS/cm) and applied potential (3000 V) the experimental results start deviating from the numerical models. The second method employing thin RhB saturated PDMS film underneath the microchannel showed similar temporal trends than the in-channel methods, however absolute temperature changes were smaller both experimentally and numerically. The thicker glass layer is thus advantageous to reduce temperature increases due to Joule heating in iDEP devices under the conditions employed in our protein and mitochondria iDEP studies. Moreover, this method will allow for elegant iDEP studies with fluorescent analytes, while observing temperature changes with adequate fluorescence optics simultaneously.

The two temperature measurement methods investigated in this work are easy to implement in iDEP microfluidic devices and complimentary. Thus, our study provides useful guidelines for experimental temperature determination in iDEP devices which allows assessing Joule heating effects in future iDEP applications but also provides suitable numerical methods to estimate these changes prior to iDEP experiments with precious biological samples.

For iDEP using the nano-constriction devices, the enhancement of this iDEP concentration was observed by further optimization of the device geometry. Numerical simulation suggests significant increase of $\nabla \boldsymbol{E}^2$ as high as 10^{19} V^2/m^3. With the improved iDEP device, $\nabla \boldsymbol{E}^2$ was enhanced by two orders of magnitude from the previous micropost array devices. With these devices, DEP experiments were performed with two proteins, IgG and β-galactosidase and positive DEP of IgG was observed with 12-fold concentration enhancement, while negative DEP for β-galactosidase. Additionally, observation of a unique voltage dependent protein concentration suggested the possibility

of ion concentration polarization occurring at the nano-constrictions. Furthermore, the comparison of numerical simulation to the experimental results suggested that the DEP force calculated using the conventional DEP theory expressed with equation (1. 6) and (3. 1) might underestimate the actual DEP force acting on the proteins. Indeed the past work on nanoparticles with think EDL reported the significantly larger DEP force than estimated by the classical theory. One of the causes of such DEP force enhancement is the electrophoretic motion of the particle which modifies the ion distribution around it and changes the induced dipole moment (Zhao & Bau, 2009; Zhao, 2011a). Our study estimated the DEP force using the classical DEP theory to be 20 ~ 40 fN for IgG and β-galactosidase, respectively, however the nanoparticle DEP reported in the past as well as our numerical simulations indicates that the DEP force acting on the protein might be underestimated.

FUTURE WORK

Microfluidic iDEP Device Improvement. The critical step in the microfluidic device design consists in the implementation of DEP traps for proteins. We aim for improved microfluidic device designs which can increase DEP force acting on proteins for separations by a) pre-concentration and b) the specific removal of molecular species but the protein of interest. For proteins with size of several nanometers, a significantly high field gradient has to be created by improving the device design such as via the use of FIBM presented in our work. However, FIBM requires long milling time to create multiple holes extending throughout the length of the entire channel, which might not be best suited for our ultimate purpose of protein separation requiring long post arrays

extended to a few cm long. Therefore, two layer designs (such as shown in *Figure 8-1*) that can be fabricated within a short time with only standard optical lithography setting are more ideal. Various device designs can be tested by numerical simulations to predict the generated electric field gradients. Such devices are expected to result in pre-concentration factors as high as presented with a nano-constriction device in this work. This method may find use in the purification of other low abundant species in serum and has further high significance to proteome studies, as the pre-concentration can be performed in gel-free solution.

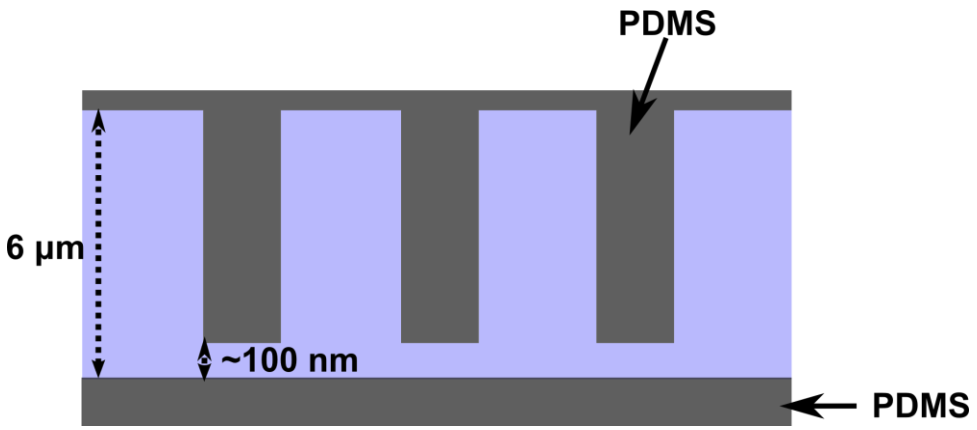

Figure 8-1. Schematic representation providing a side view of a two-layer iDEP device which can be fabricated using only standard photo- and soft lithographic techniques.

Extension of Protein iDEP Studies to Biomarker Separations. Ultimately, our plan is to explore Aβ oligomer separation in our microfluidic DEP device. Evidence points towards a key role of soluble Aβ oligomer species in Alzheimer's disease (Roychaudhuri, Yang, Hoshi, & Teplow, 2009; Walsh & Selkoe, 2007). However, a systematic investigation of the cytotoxicity of Aβ oligomers is hampered by the lack of reliable experimental techniques which are able to separate these species. Factors influencing the Aβ oligomer separation are the long time necessary for traditional

separation (low molecular weight species may already have built up high molecular weight species) and the interfering interaction with the separation medium. Investigation of Aβ oligomeric species is proposed by ultra-fast separations using our iDEP devices in the order of a few minutes and separate oligomers from monomers as well as Aβ oligomeric aggregates. Investigation can be performed using the synthetic Aβ wild-type with a fluorescent marker at the N-terminus. It has previously been shown that oligomer formation is still induced in the end-labeled Aβ (Sengupta et al., 2003) and the amyloid peptide α-synuclein (Thirunavukkuarasu, Jares-Erijman, & Jovin, 2008), giving this end-labeling method a clear preference to cumbersome post-column labeling strategies for the native peptide. Our preliminary study shows that the different sized Aβ species can be prepared using the commercially available Aβ 1-42 monomers (see Appendix D 1). Our goal is to attach different Aβ species such as monomers, oligomers, and aggregates to specific anti-amyloid antibodies which are fluorescently labeled for detection. Another important example of amyloidogenic monomeric precursor protein is lysozyme of which oligomeric species are known for its toxicity to cells which leads to cell dysfunction or eventual death (Frare et al., 2009; Hill, Miti, Richmond, & Muschol, 2011). In his regard, our preliminary study demonstrates the formation of lysozyme oligomers (see Appendix D 2). Investigation of these lysozyme species are also of our interest. Therefore, these amyloidogenic species exhibiting the different dielectric properties in solutions are then separated with our DEP microfluidic device.

REFERENCES

Abdallah, B., Chao, T.-C., Fromme, P., & Ros, A. (2012). Size based nanoparticle separation using dielectrophoretic focusing for femtosecond nanocrystallography of membrane proteins. In *Proceeding of µTAS 2012*. Okinawa, Japan.

Abdallah, B. G., Chao, T.-C., Kupitz, C., Fromme, P., & Ros, A. (2013). Dielectrophoretic sorting of membrane protein nanocrystals. *ACS Nano*, *7*(10), 9129–9137. doi:10.1021/nn403760q

Agastin, S., King, M. R., & Jones, T. B. (2009). Rapid enrichment of biomolecules using simultaneous liquid and particulate dielectrophoresis. *Lab on a Chip*, *9*(16), 2319–2325. doi:10.1039/B903831K

Albrecht, D. R., Underhill, G. H., Wassermann, T. B., Sah, R. L., & Bhatia, S. N. (2006). Probing the role of multicellular organization in three-dimensional microenvironments. *Nature Methods*, *3*(5), 369–375. doi:10.1038/nmeth873

Alexandridis, P., Holzwarth, J. F., & Hatton, T. A. (1994). Micellization of poly(ethylene oxide)-poly(propylene oxide)-poly(ethylene oxide) triblock copolymers in aqueous solutions: thermodynamics of copolymer association. *Macromolecules*, *27*(9), 2414–2425. doi:10.1021/ma00087a009

Alexandridis, P., Nivaggioli, T., & Hatton, T. A. (1995). Temperature effects on structural properties of pluronic P104 and F108 PEO-PPO-PEO block copolymer solutions. *Langmuir*, *11*(5), 1468–1476. doi:10.1021/la00005a011

Antosiewicz, J. (1995). Computation of the dipole moments of proteins. *Biophysical Journal*, *69*(4), 1344–1354. doi:10.1016/S0006-3495(95)80001-9

Antosiewicz, J., & Porschke, D. (1989). The nature of protein dipole moments: experimental and calculated permanent dipole of .alpha.-chymotrypsin. *Biochemistry*, *28*(26), 10072–10078. doi:10.1021/bi00452a029

Asokan, S. B., Jawerth, L., Carroll, R. L., Cheney, R. E., Washburn, S., & Superfine, R. (2003). Two-dimensional manipulation and orientation of actin−myosin systems with dielectrophoresis. *Nano Letters*, *3*(4), 431–437. doi:10.1021/nl0259434

Bakewell, D. J. G., Hughes, M. P., Milner, J. J., & Morgan, H. (1998). Dielectrophoretic manipulation of avidin and DNA. *Ann. Int. IEEE. Embs.*, *2*, 1079–1082. doi:10.1109/IEMBS.1998.745640

Barbulovic-Nad, I., Xuan, X., Lee, J. S. H., & Li, D. (2006). DC-dielectrophoretic separation of microparticles using an oil droplet obstacle. *Lab on a Chip*, *6*(2), 274–279. doi:10.1039/b513183a

Basuray, S., & Chang, H.-C. (2007). Induced dipoles and dielectrophoresis of nanocolloids in electrolytes. *Physical Review E*, *75*(6), 060501(1)–060501(4). doi:10.1103/PhysRevE.75.060501

Basuray, S., & Hsueh-Chia Chang. (2010). Designing a sensitive and quantifiable nanocolloid assay with dielectrophoretic crossover frequencies. *Biomicrofluidics*, *4*(1), 013205–20511.

Basuray, S., Wei, H.-H., & Chang, H.-C. (2010). Dynamic double layer effects on ac-induced dipoles of dielectric nanocolloids. *Biomicrofluidics*, *4*(2), 022801(1)–022801(7). doi:doi:10.1063/1.3455720

Baylon-Cardiel, J. L., Lapizco-Encinas, B. H., Reyes-Betanzo, C., Chávez-Santoscoy, A. V., & Martínez-Chapa, S. O. (2009a). Prediction of trapping zones in an insulator-based dielectrophoretic device. *Lab on a Chip*, *9*(20), 2896–2901. doi:10.1039/B906976C

Baylon-Cardiel, J. L., Lapizco-Encinas, B. H., Reyes-Betanzo, C., Chávez-Santoscoy, A. V., & Martínez-Chapa, S. O. (2009b). Prediction of trapping zones in an insulator-based dielectrophoretic device. *Lab on a Chip*, *9*(20), 2896. doi:10.1039/b906976c

Beech, J. P., Jönsson, P., & Tegenfeldt, J. O. (2009). Tipping the balance of deterministic lateral displacement devices using dielectrophoresis. *Lab on a Chip*, *9*(18), 2698–2706. doi:10.1039/B823275J

Beltramo, P. J., & Furst, E. M. (2012). Transition from dilute to concentrated electrokinetic behavior in the dielectric spectra of a colloidal suspension. *Langmuir*, *28*(29), 10703–10712. doi:10.1021/la301876w

Beltramo, P. J., & Furst, E. M. (2013). Predicting the disorder–order transition of dielectrophoretic colloidal assembly with dielectric spectroscopy. *Electrophoresis*, *34*(7), 1000–1007. doi:10.1002/elps.201200419

Bergman, T. L., Lavine, A. S., Incropera, F. P., & DeWitt, D. P. (2011a). *Fundamentals of Heat and Mass Transfer* (7th ed.). New York: John Wiley & Sons.

Bergman, T. L., Lavine, A. S., Incropera, F. P., & DeWitt, D. P. (2011b). *Introduction to Heat Transfer* (6th ed.). New York: John Wiley & Sons.

Camacho-Alanis, F., Gan, L., & Ros, A. (2012). Transitioning streaming to trapping in DC insulator-based dielectrophoresis for biomolecules. *Sensors and Actuators B: Chemical*, *173*(0), 668–675. doi:10.1016/j.snb.2012.07.080

Castillo, J., Tanzi, S., Dimaki, M., & Svendsen, W. (2008). Manipulation of self-assembly amyloid peptide nanotubes by dielectrophoresis. *Electrophoresis*, *29*(24), 5026–5032. doi:10.1002/elps.200800260

Chao, T., Kalinowski, J., Nyalwidhe, J., & Hansmeier, N. (2010). Comprehensive proteome profiling of the Fe(III)-reducing myxobacterium Anaeromyxobacter dehalogenans 2CP-C during growth with fumarate and ferric citrate. *PROTEOMICS*, *10*(8), 1673–1684. doi:10.1002/pmic.200900687

Chaudhari, A. M., Woudenberg, T. M., Albin, M., & Goodson, K. E. (1998). Transient liquid crystal thermometry of microfabricated PCR vessel arrays. *Journal of. Microelectromechanical Systems.*, *7*(4), 345–355. doi:10.1109/84.735341

Chaurey, V., Polanco, C., Chou, C.-F., & Swami, N. S. (2012). Floating-electrode enhanced constriction dielectrophoresis for biomolecular trapping in physiological media of high conductivity. *Biomicrofluidics*, *6*(1), 012806. doi:10.1063/1.3676069

Chaurey, V., Rohani, A., Su, Y.-H., Liao, K.-T., Chou, C.-F., & Swami, N. S. (2013). Scaling down constriction-based (electrodeless) dielectrophoresis devices for trapping nanoscale bioparticles in physiological media of high-conductivity. *Electrophoresis*, *34*(7), 1097–1104. doi:10.1002/elps.201200456

Chen, K. P., Pacheco, J. R., Hayes, M. A., & Staton, S. J. R. (2009). Insulator-based dielectrophoretic separation of small particles in a sawtooth channel. *Electrophoresis*, *30*(9), 1441–1448. doi:10.1002/elps.200800833

Chen, T., & Garimella, S. V. (2006). Measurements and high-speed visualizations of flow boiling of a dielectric fluid in a silicon microchannel heat sink. *International Journal of Multiphase Flow*, *32*(8), 957–971. doi:10.1016/j.ijmultiphaseflow.2006.03.002

Chou, C.-F., Tegenfeldt, J. O., Bakajin, O., Chan, S. S., Cox, E. C., Darnton, N., … Austin, R. H. (2002). Electrodeless dielectrophoresis of single- and double-stranded DNA. *Biophysical Journal*, *83*(4), 2170–2179. doi:10.1016/S0006-3495(02)73977-5

Clarke, R. W., Piper, J. D., Ying, L., & Klenerman, D. (2007). Surface conductivity of biological macromolecules measured by nanopipette dielectrophoresis. *Physical Review Letters*, *98*(19), 198102(1)–198102(4). doi:10.1103/PhysRevLett.98.198102

Clarke, R. W., White, S. S., Zhou, D., Ying, L., & Klenerman, D. (2005). Trapping of proteins under physiological conditions in a nanopipette. *Angewandte. Chemie International Edition.* *44*(24), 3747–3750. doi:10.1002/ange.200500196

Clow, A. L., Gaynor, P. T., & Oback, B. J. (2010). A novel micropit device integrates automated cell positioning by dielectrophoresis and nuclear transfer by electrofusion. *Biomedical Microdevices*, *12*(5), 777–786. doi:10.1007/s10544-010-9432-3

Coppeta, J., & Rogers, C. (1998). Dual emission laser induced fluorescence for direct planar scalar behavior measurements. *Experiments in Fluids*, *25*(1), 1–15. doi:10.1007/s003480050202

Cummings, E. B. (2003). Streaming dielectrophoresis for continuous-flow microfluidic devices. *IEEE Engineering in Medicine and Biology Magazine: The Quarterly Magazine of the Engineering in Medicine & Biology Society*, *22*(6), 75–84.

Cummings, E. B., & Singh, A. K. (2003). Dielectrophoresis in microchips containing arrays of insulating posts: theoretical and experimental results. *Analytical Chemistry*, *75*(18), 4724–4731. doi:10.1021/ac0340612

Davalos, R., McGraw, G., Wallow, T., Morales, A., Krafcik, K., Fintschenko, Y., … Simmons, B. (2008). Performance impact of dynamic surface coatings on polymeric insulator-based dielectrophoretic particle separators. *Analytical and Bioanalytical Chemistry*, *390*(3), 847–855. doi:10.1007/s00216-007-1426-5

Davalos, R. V., McGraw, G. J., Wallow, T. I., Morales, A. M., Krafcik, K. L., Fintschenko, Y., … Simmons, B. A. (2008). Performance impact of dynamic surface coatings on polymeric insulator-based dielectrophoretic particle separators. *Analytical and Bioanalytical Chemistry*, *390*(3), 847–855. doi:10.1007/s00216-007-1426-5

De la Rica, R., Mendoza, E., Lechuga, L. M., & Matsui, H. (2008). Label-Free Pathogen Detection with Sensor Chips Assembled from Peptide Nanotubes. *Angewandte Chemie International Edition*, *47*(50), 9752–9755. doi:10.1002/anie.200804299

De Mello, A. J., Habgood, M., Lancaster, N. L., Welton, T., & Wootton, R. C. R. (2004). Precise temperature control in microfluidic devices using Joule heating of ionic liquids. *Lab on a Chip*, *4*(5), 417–419. doi:10.1039/B405760K

Dukhin, S. S. (1993). Non-equilibrium electric surface phenomena. *Advances in Colloid and Interface Science*, *44*(0), 1–134. doi:10.1016/0001-8686(93)80021-3

Duong, T. T., Kim, G., Ros, R., Streek, M., Schmid, F., Brugger, J., … Ros, A. (2003). Size-dependent free solution DNA electrophoresis in structured microfluidic systems. *Microelectronic Engineering*, *67–68*, 905–912. doi:10.1016/S0167-9317(03)00153-9

Erickson, D., Liu, X., Venditti, R., Li, D., & Krull, U. J. (2005). Electrokinetically based approach for single-nucleotide polymorphism discrimination using a microfluidic device. *Analytical Chemistry*, *77*(13), 4000–4007. doi:10.1021/ac050236r

Ermolina, I., & Morgan, H. (2005). The electrokinetic properties of latex particles: comparison of electrophoresis and dielectrophoresis. *Journal of Colloid and Interface Science*, *285*(1), 419–428. doi:10.1016/j.jcis.2004.11.003

Frare, E., Mossuto, M. F., de Laureto, P. P., Tolin, S., Menzer, L., Dumoulin, M., … Fontana, A. (2009). Characterization of oligomeric species on the aggregation pathway of human lysozyme. *Journal of Molecular Biology*, *387*(1), 17–27. doi:10.1016/j.jmb.2009.01.049

Fujisawa, N., Funatani, S., & Katoh, N. (2005). Scanning liquid-crystal thermometry and stereo velocimetry for simultaneous three-dimensional measurement of temperature and velocity field in a turbulent Rayleigh-Bérnard convection. *Experiments in Fluids*, *38*(3), 291–303. doi:10.1007/s00348-004-0891-2

Gagnon, Z. R. (2011). Cellular dielectrophoresis: applications to the characterization, manipulation, separation and patterning of cells. *Electrophoresis*, *32*(18), 2466–2487. doi:10.1002/elps.201100060

Gallo-Villanueva, R. C., Rodríguez-López, C. E., Díaz-de-la-Garza, R. I., Reyes-Betanzo, C., & Lapizco-Encinas, B. H. (2009). DNA manipulation by means of insulator-based dielectrophoresis employing direct current electric fields. *Electrophoresis*, *30*(24), 4195–4205. doi:10.1002/elps.200900355

Gallo-Villanueva, R. C., Sano, M. B., Lapizco-Encinas, B. H., & Davalos, R. V. (2014). Joule heating effects on particle immobilization in insulator-based dielectrophoretic devices. *Electrophoresis*, *35*(2-3), 352–361. doi:10.1002/elps.201300171

Gan, L., Chao, T.-C., Camacho-Alanis, F., & Ros, A. (2013). Six-helix bundle and triangle DNA origami insulator-based dielectrophoresis. *Analytical Chemistry*, *85*(23), 11427–11434. doi:10.1021/ac402493u

Gencoglu, A., Camacho-Alanis, F., Nguyen, V. T., Nakano, A., Ros, A., & Minerick, A. R. (2011). Quantification of pH gradients and implications in insulator-based dielectrophoresis of biomolecules. *Electrophoresis*, *32*(18), 2436–2447. doi:10.1002/elps.201100090

Gielen, F., Pereira, F., deMello, A. J., & Edel, J. B. (2010). High-resolution local imaging of temperature in dielectrophoretic platforms. *Analytical Chemistry*, *82*(17), 7509–7514. doi:10.1021/ac101557g

Gong, J.-R. (2010). Label-free attomolar detection of proteins using integrated nanoelectronic and electrokinetic devices. *Small*, *6*(8), 967–973. doi:10.1002/smll.200902132

Green, N. ., Morgan, H., & Milner, J. J. (1997). Manipulation and trapping of sub-micron bioparticles using dielectrophoresis. *Journal of Biochemical and Biophysical Methods*, *35*(2), 89–102. doi:10.1016/S0165-022X(97)00033-X

Green, N. G., & Morgan, H. (1999). Dielectrophoresis of submicrometer latex spheres. 1. Experimental results. *The Journal of Physical Chemistry B*, *103*(1), 41–50. doi:10.1021/jp9829849

Green, N. G., Ramos, A., González, A., Morgan, H., & Castellanos, A. (2000). Fluid flow induced by nonuniform ac electric fields in electrolytes on microelectrodes. I. Experimental measurements. *Physical Review E*, *61*(4), 4011–4018. doi:10.1103/PhysRevE.61.4011

Gunda, N. S. K., & Mitra, S. K. (2010). Modeling of dielectrophoretic transport of myoglobin molecules in microchannels. *Biomicrofluidics*, *4*(1), 014105(1)–014105(20). doi:doi:10.1063/1.3339773

Hawkins, B. G., & Kirby, B. J. (2010). Electrothermal flow effects in insulating (electrodeless) dielectrophoresis systems. *Electrophoresis*, *31*(22), 3622–3633. doi:10.1002/elps.201000429

Hawkins, B. G., Smith, A. E., Syed, Y. A., & Kirby, B. J. (2007). Continuous-flow particle separation by 3D insulative dielectrophoresis using coherently shaped, dc-biased, ac electric fields. *Analytical Chemistry*, *79*(19), 7291–7300. doi:10.1021/ac0707277

Haynes, W. M. (2012). *CRC Handbook of Chemistry and Physics* (93rd ed.). Boca Raton: CRC Press.

Hellmich, W., Regtmeier, J., Duong, T. T., Ros, R., Anselmetti, D., & Ros, A. (2005). Poly(oxyethylene) based surface coatings for poly(dimethylsiloxane) microchannels. *Langmuir*, *21*(16), 7551–7557. doi:10.1021/la0510432

Henning, A., Bier, F. F., & Hölzel, R. (2010). Dielectrophoresis of DNA: Quantification by impedance measurements. *Biomicrofluidics*, *4*(2), 022803(1)–022803(9). doi:doi:10.1063/1.3430550

Heuvel, M. G. L. van den, & Dekker, C. (2007). Motor proteins at work for nanotechnology. *Science*, *317*(5836), 333–336. doi:10.1126/science.1139570

Hill, S. E., Miti, T., Richmond, T., & Muschol, M. (2011). Spatial extent of charge repulsion regulates assembly pathways for lysozyme amyloid fibrils. *PLoS ONE*, *6*(4), e18171. doi:10.1371/journal.pone.0018171

Hjelmeland, L. M., Nebert, D. W., & Osborne, J. C., Jr. (1983). Sulfobetaine derivatives of bile acids: nondenaturing surfactants for membrane biochemistry. *Analytical Biochemistry*, *130*(1), 72–82.

Hölzel, R., Calander, N., Chiragwandi, Z., Willander, M., & Bier, F. F. (2005). Trapping single molecules by dielectrophoresis. *Physical Review Letters*, *95*(12), 128102(1)–128102(4). doi:10.1103/PhysRevLett.95.128102

Hu, X., Bessette, P. H., Qian, J., Meinhart, C. D., Daugherty, P. S., & Soh, H. T. (2005). Marker-specific sorting of rare cells using dielectrophoresis. *Proceedings of the National Academy of Sciences of the United States of America*, *102*(44), 15757–15761. doi:10.1073/pnas.0507719102

Huang, L. R., Tegenfeldt, J. O., Kraeft, J. J., Sturm, J. C., Austin, R. H., & Cox, E. C. (2002). A DNA prism for high-speed continuous fractionation of large DNA molecules. *Nature Biotechnology*, *20*(10), 1048–1051. doi:10.1038/nbt733

Hübner, Y., Hoettges, K. F., McDonnell, M. B., Carter, M. J., & Hughes, M. P. (2007). Applications of dielectrophoretic/electro-hydrodynamic “zipper” electrodes for detection of biological nanoparticles. *International Journal of Nanomedicine*, *2*(3), 427–431.

Hughes, M. P. (2002). *Nanoelectromechanics in Engineering and Biology* (1st ed.). Boca Raton: CRC Press.

Hughes, M. P. (2002). Strategies for dielectrophoretic separation in laboratory-on-a-chip systems. *Electrophoresis*, *23*(16), 2569–2582. doi:10.1002/1522-2683(200208)23:16<2569::AID-ELPS2569>3.0.CO;2-M

Iler, R. K. (1979). *The Chemistry of Silica: Solubility, Polymerization, Colloid and Surface Properties and Biochemistry of Silica*. New York: Wiley.

Jaber, F. T., Labeed, F. H., & Hughes, M. P. (2009). Action potential recording from dielectrophoretically positioned neurons inside micro-wells of a planar microelectrode array. *Journal of Neuroscience Methods*, *182*(2), 225–235. doi:10.1016/j.jneumeth.2009.06.013

Jachimska, B., Wasilewska, M., & Adamczyk, Z. (2008). Characterization of globular protein solutions by dynamic light scattering, Electrophoretic mobility, and viscosity measurements. *Langmuir*, *24*(13), 6866–6872. doi:10.1021/la800548p

Jacobson, R. H., Zhang, X.-J., DuBose, R. F., & Matthews, B. W. (1994). Three-dimensional structure of β-galactosidase from E. coli. *Nature*, *369*(6483), 761–766. doi:10.1038/369761a0

Jaeger, M. S., Mueller, T., & Schnelle, T. (2007). Thermometry in dielectrophoresis chips for contact-free cell handling. *Journal of Physics D: Applied Physics*, *40*(1), 95–105. doi:10.1088/0022-3727/40/1/S14

Jones, T. B. (2005). *Electromechanics of Particles*. Cambridge: Cambridge University Press.

Kang, H., Lee, J., Park, J., & Lee, H. H. (2006). An improved method of preparing composite poly(dimethylsiloxane) moulds. *Nanotechnology*, *17*(1), 197. doi:10.1088/0957-4484/17/1/032

Kang, J., Yan, J., Liu, J., Qiu, H., Yin, X.-B., Yang, X., & Wang, E. (2005). Dynamic coating for resolving rhodamine B adsorption to poly(dimethylsiloxane)/glass hybrid chip with laser-induced fluorescence detection. *Talanta*, *66*(4), 1018–1024. doi:10.1016/j.talanta.2005.01.002

Kang, K. H., Kang, Y., Xuan, X., & Li, D. (2006). Continuous separation of microparticles by size with direct current-dielectrophoresis. *Electrophoresis*, *27*(3), 694–702. doi:10.1002/elps.200500558

Kang, Y., Li, D., Kalams, S. A., & Eid, J. E. (2008). DC-Dielectrophoretic separation of biological cells by size. *Biomedical Microdevices*, *10*(2), 243–249. doi:10.1007/s10544-007-9130-y

Kawabata, T., & Washizu, M. (2001). Dielectrophoretic detection of molecular bindings. *IEEE Transactions on Industry Applications*, *37*(6), 1625–1633. doi:10.1109/28.968170

Kim, S. J., Li, L. D., & Han, J. (2009). Amplified electrokinetic response by concentration polarization near nanofluidic channel. *Langmuir*, *25*(13), 7759–7765. doi:10.1021/la900332v

Kim, S. M., Burns, M. A., & Hasselbrink, E. F. (2006). Electrokinetic protein preconcentration using a simple glass/poly(dimethylsiloxane) microfluidic chip. *Analytical Chemistry*, *78*(14), 4779–4785. doi:10.1021/ac060031y

Koh, S. J. (2007). Strategies for controlled placement of nanoscale building blocks. *Nanoscale Research Letters*, *2*(11), 519–545. doi:10.1007/s11671-007-9091-3

Kwon, J.-S., Maeng, J.-S., Chun, M.-S., & Song, S. (2008). Improvement of microchannel geometry subject to electrokinesis and dielectrophoresis using numerical simulations. *Microfluidics and Nanofluidics*, *5*(1), 23–31. doi:10.1007/s10404-007-0210-3

Lacey, M. E., Webb, A. G., & Sweedler, J. V. (2000). Monitoring temperature changes in capillary electrophoresis with nanoliter-volume NMR thermometry. *Analytical Chemistry*, *72*(20), 4991–4998. doi:10.1021/ac000649m

Lagally, E. T., Medintz, I., & Mathies, R. A. (2001). Single-molecule DNA amplification and analysis in an integrated microfluidic device. *Analytical Chemistry*, *73*(3), 565–570. doi:10.1021/ac001026b

Lapizco-Encinas, B. H., Davalos, R. V., Simmons, B. A., Cummings, E. B., & Fintschenko, Y. (2005). An insulator-based (electrodeless) dielectrophoretic concentrator for microbes in water. *Journal of Microbiological Methods*, *62*(3), 317–326. doi:10.1016/j.mimet.2005.04.027

Lapizco-Encinas, B. H., Ozuna-Chacón, S., & Rito-Palomares, M. (2008). Protein manipulation with insulator-based dielectrophoresis and direct current electric fields. *Journal of Chromatography A*, *1206*(1), 45–51. doi:10.1016/j.chroma.2008.05.077

Lapizco-Encinas, B. H., & Rito-Palomares, M. (2007). Dielectrophoresis for the manipulation of nanobioparticles. *Electrophoresis*, *28*(24), 4521–4538. doi:10.1002/elps.200700303

Lapizco-Encinas, B. H., Simmons, B. A., Cummings, E. B., & Fintschenko, Y. (2004). Dielectrophoretic concentration and separation of live and dead bacteria in an array of insulators. *Analytical Chemistry*, *76*(6), 1571–1579. doi:10.1021/ac034804j

Lee, P.-S., Garimella, S. V., & Liu, D. (2005). Investigation of heat transfer in rectangular microchannels. *International Journal of. Heat Mass Transfer*, *48*(9), 1688–1704. doi:10.1016/j.ijheatmasstransfer.2004.11.019

Li, H., & Bashir, R. (2002). Dielectrophoretic separation and manipulation of live and heat-treated cells of Listeria on microfabricated devices with interdigitated electrodes. *Sensors and Actuators B: Chemical*, *86*(2–3), 215–221. doi:10.1016/S0925-4005(02)00172-7

Li, H.-W., Muir, B. V. O., Fichet, G., & Huck, W. T. S. (2003). Nanocontact printing: A route to sub-50-nm-scale chemical and biological patterning. *Langmuir*, *19*(6), 1963–1965. doi:10.1021/la0269098

Liao, K.-T., Chaurey, V., Tsegaye, M., Chou, C.-F., & Swami, N. S. (2011). Nanofluidics for selective protein trapping in bio-fluids. In *Proceeding of µTAS 2011*. Seattle, WA.

Liao, K.-T., & Chou, C.-F. (2012). Nanoscale Molecular Traps and dams for ultrafast protein enrichment in high-conductivity buffers. *Journal of the American Chemical Society*, *134*(21), 8742–8745. doi:10.1021/ja3016523

Liao, K.-T., Tsegaye, M., Chaurey, V., Chou, C.-F., & Swami, N. S. (2012). Nano-constriction device for rapid protein preconcentration in physiological media through a balance of electrokinetic forces. *Electrophoresis*, *33*(13), 1958–1966. doi:10.1002/elps.201100707

Liu, R., Barkhordarian, H., Emadi, S., Park, C. B., & Sierks, M. R. (2005). Trehalose differentially inhibits aggregation and neurotoxicity of beta-amyloid 40 and 42. *Neurobiology of Disease*, *20*(1), 74–81. doi:10.1016/j.nbd.2005.02.003

Luo, J., Abdallah, B. G., Wolken, G. G., Arriaga, E. A., & Ros, A. (2014). Insulator-based dielectrophoresis of mitochondria. *Biomicrofluidics*, *8*, 021801. doi: 10.1063/1.486685

Lyklema, J. (1995). *Fundamentals of Interface and Colloid Science* (Vols. 1-2). Waltham, MA: Academic Press.

MacQueen, L. A., Buschmann, M. D., & Wertheimer, M. R. (2008). Gene delivery by electroporation after dielectrophoretic positioning of cells in a non-uniform electric field. *Bioelectrochemistry*, *72*(2), 141–148. doi:10.1016/j.bioelechem.2008.01.006

Mao, H., Yang, T., & Cremer, P. S. (2002). A microfluidic device with a linear temperature gradient for parallel and combinatorial measurements. *Journal of the American Chemical Society*, *124*(16), 4432–4435. doi:10.1021/ja017625x

Martinez-Duarte, R. (2012). Microfabrication technologies in dielectrophoresis applications—A review. *Electrophoresis*, *33*(21), 3110–3132. doi:10.1002/elps.201200242

Maruyama, H., & Nakayama, Y. (2008). Trapping protein molecules at a carbon nanotube tip using dielectrophoresis. *Applied Physics Express*, *1*(12), 124001(1)–124001(3). doi:10.1143/APEX.1.124001

Mastrangelo, I. A., Ahmed, M., Sato, T., Liu, W., Wang, C., Hough, P., & Smith, S. O. (2006). High-resolution atomic force microscopy of soluble Aβ42 Oligomers. *Journal of Molecular Biology*, *358*(1), 106–119. doi:10.1016/j.jmb.2006.01.042

Matyushov, D. V. (2012a). Dipolar response of hydrated proteins. *The Journal of Chemical Physics*, *136*(8), 085102(1)–085102(15). doi:doi:10.1063/1.3688229

Matyushov, D. V. (2012b). On the theory of dielectric spectroscopy of protein solutions. *Journal of Physics: Condensed Matter*, *24*(32), 325105(1)–325105(8). doi:10.1088/0953-8984/24/32/325105

Meighan, M. M., Staton, S. J. R., & Hayes, M. A. (2009). Bioanalytical separations using electric field gradient techniques. *Electrophoresis*, *30*(5), 852–865. doi:10.1002/elps.200800614

Morgan, H., & Green, N. G. (1997). Dielectrophoretic manipulation of rod-shaped viral particles. *Journal of Electrostatics*, *42*(3), 279–293. doi:10.1016/S0304-3886(97)00159-9

Mukhopadhyay, R. (2007). When PDMS isn't the best. *Analytical Chemistry*, *79*(9), 3248–3253. doi:10.1021/ac071903e

Nakano, A., Camacho-Alanis, F., Chao, T.-C., & Ros, A. (2012). Tuning direct current streaming dielectrophoresis of proteins. *Biomicrofluidics*, *6*(3), 034108. doi:doi:10.1063/1.4742695

Nakano, A., Chao, T.-C., Camacho-Alanis, F., & Ros, A. (2011). Immunoglobulin G and bovine serum albumin streaming dielectrophoresis in a microfluidic device. *Electrophoresis*, *32*(17), 2314–2322. doi:10.1002/elps.201100037

Napoli, M., Eijkel, J. C. T., & Pennathur, S. (2010). Nanofluidic technology for biomolecule applications: a critical review. *Lab on a Chip*, *10*(8), 957–985. doi:10.1039/B917759K

Odom, T. W., Love, J. C., Wolfe, D. B., Paul, K. E., & Whitesides, G. M. (2002). Improved pattern transfer in soft lithography using composite stamps. *Langmuir*, *18*(13), 5314–5320. doi:10.1021/la020169l

Oleinikova, A., Sasisanker, P., & Weingärtner, H. (2004). What can really be learned from dielectric spectroscopy of protein solutions? A case study of ribonuclease A. *The Journal of Physical Chemistry B*, *108*(24), 8467–8474. doi:10.1021/jp049618b

Otto, S., Kaletta, U., Bier, F. F., Wenger, C., & Hölzel, R. (2014). Dielectrophoretic immobilisation of antibodies on microelectrode arrays. *Lab on a Chip*, *14*(5), 998–1004. doi:10.1039/C3LC51190A

Pethig, R. (1979). *Dielectric and Electronic Properties of Biological Materials*. New York: Wiley.

Pethig, R. (1996). Dielectrophoresis: Using inhomogeneous AC electrical fields to separate and manipulate cells. *Critical Reviews in Biotechnology*, *16*(4), 331–348. doi:10.3109/07388559609147425

Pethig, R. (2010). Review article—dielectrophoresis: Status of the theory, technology, and applications. *Biomicrofluidics*, *4*(2), 022811. doi:doi:10.1063/1.3456626

Pohl, H. A. (1978). *Dielectrophoresis*. Cambridge: Cambridge University Press.

Pommer, M. S., Zhang, Y., Keerthi, N., Chen, D., Thomson, J. A., Meinhart, C. D., & Soh, H. T. (2008). Dielectrophoretic separation of platelets from diluted whole blood in microfluidic channels. *Electrophoresis*, *29*(6), 1213–1218. doi:10.1002/elps.200700607

Probstein, R. F. (2003). *Physicochemical Hydrodynamics: An Introduction* (2nd Edition.). Hoboken, NJ: Wiley.

Pysher, M. D., & Hayes, M. A. (2007). Electrophoretic and dielectrophoretic field gradient technique for separating bioparticles. *Analytical Chemistry*, *79*(12), 4552–4557. doi:10.1021/ac070534j

Regtmeier, J., Duong, T. T., Eichhorn, R., Anselmetti, D., & Ros, A. (2007). Dielectrophoretic manipulation of DNA: Separation and polarizability. *Analytical Chemistry*, *79*(10), 3925–3932. doi:10.1021/ac062431r

Regtmeier, J., Eichhorn, R., Bogunovic, L., Ros, A., & Anselmetti, D. (2010). Dielectrophoretic trapping and polarizability of DNA: The role of spatial conformation. *Analytical Chemistry*, *82*(17), 7141–7149. doi:10.1021/ac1005475

Richards, C. D., & Richards, R. F. (1998). Transient temperature measurements in a convectively cooled droplet. *Experiments in Fluids*, *25*(5-6), 392–400. doi:10.1007/s003480050246

Rivette, N. J., & Baygents, J. C. (1996). A note on the electrostatic force and torque acting on an isolated body in an electric field. *Chemical Engineering Science*, *51*(23), 5205–5211. doi:http://dx.doi.org/10.1016/S0009-2509(96)00337-5

Robinson, T., Schaerli, Y., Wootton, R., Hollfelder, F., Dunsby, C., Baldwin, G., … deMello, A. (2009). Removal of background signals from fluorescence thermometry measurements in PDMS microchannels using fluorescence lifetime imaging. *Lab Chip*, *9*(23), 3437–3441. doi:10.1039/B913293G

Roman, G. T., Hlaus, T., Bass, K. J., Seelhammer, T. G., & Culbertson, C. T. (2005). Sol−gel modified poly(dimethylsiloxane) microfluidic devices with high electroosmotic mobilities and hydrophilic channel wall characteristics. *Analytical Chemistry*, *77*(5), 1414–1422. doi:10.1021/ac048811z

Roman, G. T., McDaniel, K., & Culbertson, C. T. (2006). High efficiency micellar electrokinetic chromatography of hydrophobic analytes on poly(dimethylsiloxane) microchips. *Analyst, 131*(2), 194–201. doi:10.1039/B510765B

Rosenqvist, E., Jøssang, T., Feder, J., & Harbitz, O. (1986). Characterization of a heat-stable fraction of human IgG. *Journal of Protein Chemistry, 5*(5), 323–333. doi:10.1007/BF01025961

Ross, D., Gaitan, M., & Locascio, L. E. (2001). Temperature measurement in microfluidic systems using a temperature-dependent fluorescent dye. *Analytical Chemistry, 73*(17), 4117–4123. doi:10.1021/ac010370l

Ross, D., & Locascio, L. E. (2002). Microfluidic temperature gradient focusing. *Analytical Chemistry*, *74*(11), 2556–2564. doi:10.1021/ac025528w

Roychaudhuri, R., Yang, M., Hoshi, M. M., & Teplow, D. B. (2009). Amyloid β-protein assembly and Alzheimer disease. *Journal of Biological Chemistry, 284*(8), 4749–4753. doi:10.1074/jbc.R800036200

Ryan, D. A., Narrow, W. C., Federoff, H. J., & Bowers, W. J. (2010). An improved method for generating consistent soluble amyloid-beta oligomer preparations for in vitro neurotoxicity studies. *Journal of Neuroscience Methods, 190*(2), 171–179. doi:10.1016/j.jneumeth.2010.05.001

Samy, R., Glawdel, T., & Ren, C. L. (2008). Method for microfluidic whole-chip temperature measurement using thin-film poly(dimethylsiloxane)/rhodamine B. *Analytical Chemistry*, *80*(2), 369–375. doi:10.1021/ac071268c

Sandin, S., Öfverstedt, L.-G., Wikström, A.-C., Wrange, Ö., & Skoglund, U. (2004). Structure and flexibility of individual immunoglobulin G molecules in solution. *Structure, 12*(3), 409–415. doi:10.1016/j.str.2004.02.011

Sasisanker, P., Oleinikova, A., Weingärtner, H., Ravindra, R., & Winter, R. (2004). Solvation properties and stability of ribonuclease A in normal and deuterated water studied by dielectric relaxation and differential scanning/pressure perturbation calorimetry. *Physical Chemistry Chemical Physics*, *6*(8), 1899–1905. doi:10.1039/B314070A

Sengupta, P., Garai, K., Sahoo, B., Shi, Y., Callaway, D. J. E., & Maiti, S. (2003). The amyloid beta peptide (Abeta(1-40)) is thermodynamically soluble at physiological concentrations. *Biochemistry*, *42*(35), 10506–10513. doi:10.1021/bi0341410

Srivastava, S. K., Gencoglu, A., & Minerick, A. R. (2011). DC insulator dielectrophoretic applications in microdevice technology: a review. *Analytical and Bioanalytical Chemistry*, *399*(1), 301–321. doi:10.1007/s00216-010-4222-6

Staton, S. J. R., Jones, P. V., Ku, G., Gilman, S. D., Kheterpal, I., & Hayes, M. A. (2012). Manipulation and capture of Aβ amyloid fibrils and monomers by DC insulator gradient dielectrophoresis (DC-iGDEP). *Analyst*, *137*(14), 3227–3229. doi:10.1039/C2AN35138B

Stine, W. B., Dahlgren, K. N., Krafft, G. A., & LaDu, M. J. (2003). In Vitro Characterization of conditions for amyloid-β peptide oligomerization and fibrillogenesis. *Journal of Biological Chemistry*, *278*(13), 11612–11622.

Swami, N., Chou, C.-F., Ramamurthy, V., & Chaurey, V. (2009). Enhancing DNA hybridization kinetics through constriction-based dielectrophoresis. *Lab on a Chip*, *9*(22), 3212–3220. doi:10.1039/B910598K

Takashima, S. (2002). Electric dipole moments of globular proteins: measurement and calculation with NMR and X-ray databases. *Journal of Non-Crystalline Solids*, *305*(1–3), 303–310. doi:10.1016/S0022-3093(02)01255-3

Tandon, V., Bhagavatula, S. K., Nelson, W. C., & Kirby, B. J. (2008). Zeta potential and electroosmotic mobility in microfluidic devices fabricated from hydrophobic polymers: 1. The origins of charge. *Electrophoresis*, *29*(5), 1092–1101. doi:10.1002/elps.200700734

Thirunavukkuarasu, S., Jares-Erijman, E. A., & Jovin, T. M. (2008). Multiparametric fluorescence detection of early stages in the amyloid protein aggregation of pyrene-labeled alpha-synuclein. *Journal of Molecular Biology*, *378*(5), 1064–1073. doi:10.1016/j.jmb.2008.03.034

Uppalapati, M., Huang, Y.-M., Jackson, T. N., & Hancock, W. O. (2008). Microtubule alignment and manipulation using AC electrokinetics. *Small*, *4*(9), 1371–1381. doi:10.1002/smll.200701088

Viefhues, M., Manchanda, S., Chao, T.-C., Anselmetti, D., Regtmeier, J., & Ros, A. (2011). Physisorbed surface coatings for poly(dimethylsiloxane) and quartz microfluidic devices. *Analytical and Bioanalytical Chemistry*, *401*(7), 2113–2122. doi:10.1007/s00216-011-5301-z

Voldman, J. (2006). Electrical forces for microscale cell manipulation. *Annual Review of Biomedical Engineering*, *8*, 425–454. doi:10.1146/annurev.bioeng.8.061505.095739

Voldman, J., Gray, M. L., Toner, M., & Schmidt, M. A. (2002). A microfabrication-based dynamic array cytometer. *Analytical Chemistry*, *74*(16), 3984–3990. doi:10.1021/ac0256235

von Smoluchowski, M. (1914). *Elektrische endosmose und stromungsstrome. In Handbuch der Elektrizitat und des Magnetimus* (Vol. 2). Leipzig: J. A. Barth.

Walsh, D. M., & Selkoe, D. J. (2007). Aβ Oligomers – a decade of discovery. *Journal of Neurochemistry*, *101*(5), 1172–1184. doi:10.1111/j.1471-4159.2006.04426.x

Wang, J. D., Douville, N. J., Takayama, S., & ElSayed, M. (2012). Quantitative analysis of molecular absorption into PDMS microfluidic channels. *Annals of Biomedical Engineering*, *40*(9), 1862–1873. doi:10.1007/s10439-012-0562-z

Wang, S., Westcott, S., & Chen, W. (2002). Nanoparticle luminescence thermometry. *The Journal of Physical Chemistry B*, *106*(43), 11203–11209. doi:10.1021/jp026445m

Wang, X.-B., Yang, J., Huang, Y., Vykoukal, J., Becker, F. F., & Gascoyne, P. R. C. (2000). Cell separation by dielectrophoretic field-flow-fractionation. *Analytical Chemistry*, *72*(4), 832–839. doi:10.1021/ac990922o

Wang, Y.-C., Stevens, A. L., & Han, J. (2005). Million-fold preconcentration of proteins and peptides by nanofluidic filter. *Analytical Chemistry*, *77*(14), 4293–4299. doi:10.1021/ac050321z

Washizu, M., Suzuki, S., Kurosawa, O., Nishizaka, T., & Shinohara, T. (1994). Molecular dielectrophoresis of biopolymers. *IEEE Transactions on Industry Applications*, *30*(4), 835–843. doi:10.1109/28.297897

Wirth, C. L., Sides, P. J., & Prieve, D. C. (2013). Electrolyte dependence of particle motion near an electrode during ac polarization. *Physical Review E*, *87*(3), 032302. doi:10.1103/PhysRevE.87.032302

Xu, Y., Jiang, H., & Wang, E. (2007). Ionic liquid-assisted PDMS microchannel modification for efficiently resolving fluorescent dye and protein adsorption. *Electrophoresis*, *28*(24), 4597–4605. doi:10.1002/elps.200700261

Xuan, X. (2008). Joule heating in electrokinetic flow. *Electrophoresis*, *29*(1), 33–43. doi:10.1002/elps.200700302

Yang, J., Huang, Y., Wang, X., Wang, X.-B., Becker, F. F., & Gascoyne, P. R. C. (1999). Dielectric properties of human leukocyte subpopulations determined by electrorotation as a cell separation criterion. *Biophysical Journal*, *76*(6), 3307–3314. doi:10.1016/S0006-3495(99)77483-7

Yang, J., Huang, Y., Wang, X.-B., Becker, F. F., & Gascoyne, P. R. C. (1999). Cell separation on microfabricated electrodes using dielectrophoretic/gravitational field-flow fractionation. *Analytical Chemistry*, *71*(5), 911–918. doi:10.1021/ac981250p

Yang, J., Huang, Y., Wang, X.-B., Becker, F. F., & Gascoyne, P. R. C. (2000). Differential analysis of human leukocytes by dielectrophoretic field-flow-fractionation. *Biophysical Journal*, *78*(5), 2680–2689. doi:10.1016/S0006-3495(00)76812-3

Zangle, T. A., Mani, A., & Santiago, J. G. (2010). Theory and experiments of concentration polarization and ion focusing at microchannel and nanochannel interfaces. *Chemical Society Reviews*, *39*(3), 1014–1035. doi:10.1039/B902074H

Zhang, C., Khoshmanesh, K., Mitchell, A., & Kalantar-zadeh, K. (2010). Dielectrophoresis for manipulation of micro/nano particles in microfluidic systems. *Analytical and Bioanalytical Chemistry*, *396*(1), 401–420. doi:10.1007/s00216-009-2922-6

Zhao, H. (2011a). Double-layer polarization of a non-conducting particle in an alternating current field with applications to dielectrophoresis. *Electrophoresis*, *32*(17), 2232–2244. doi:10.1002/elps.201100035

Zhao, H. (2011b). Role of hydrodynamic behavior of DNA molecules in dielectrophoretic polarization under the action of an electric field. *Physical Review E*, *84*(2), 021910(1)–021910(6). doi:10.1103/PhysRevE.84.021910

Zhao, H., & Bau, H. H. (2009). The polarization of a nanoparticle surrounded by a thick electric double layer. *Journal of Colloid and Interface Science*, *333*(2), 663–671. doi:10.1016/j.jcis.2009.01.056

Zhao, H., & Bau, H. H. (2010). Polarization of nanorods submerged in an electrolyte solution and subjected to an ac electrical field. *Langmuir*, *26*(8), 5412–5420. doi:10.1021/la903842z

Zheng, L., Brody, J. P., & Burke, P. J. (2004). Electronic manipulation of DNA, proteins, and nanoparticles for potential circuit assembly. *Biosensors and Bioelectronics*, *20*(3), 606–619. doi:10.1016/j.bios.2004.03.029

Zhu, J., Tzeng, T.-R. J., Hu, G., & Xuan, X. (2009). DC dielectrophoretic focusing of particles in a serpentine microchannel. *Microfluidics and Nanofluidics*, *7*(6), 751–756. doi:10.1007/s10404-009-0432-7

APPENDIX A

SUPPLEMENTAL MATERIAL FOR CHAPTER 3

Appendix A 1: Theoretical DEP models for a prolate and oblate ellipsoid.

For IgG estimating the prolate ellipsoidal shape with its dimension of a = 5 nm, $b = c$ = 2.5 nm (Sandin et al., 2004), Z is calculated as (Clarke et al., 2007; Morgan & Green, 1997):

$$Z = \frac{bc}{2a^2e^3}\left[ln\left(\frac{1+e}{1-e}\right) - 2e\right] \quad \text{(A 1)}$$

where e corresponds to eccentricity given as:

$$e = \sqrt{1 - \frac{bc}{a^2}} \quad \text{(A 2)}$$

Additionally, the mean translational coefficient $\bar{R}$ is given as:

$$\bar{R} = {}^{2}/_{S} \quad \text{(A 3)}$$

For a prolate ellipsoid, S amounts in (Probstein, 2003):

$$S = \frac{2}{\sqrt{a^2-b^2}} \ln \frac{a+\sqrt{a^2-b^2}}{b} \quad \text{(A 4)}$$

For an oblate ellipsoidal particle, such as β-galactosidase with the dimension approximated as 4.5 × 4.5 × 8 nm from the crystallography data (Jacobson et al., 1994), Z is calculated as:

$$Z = \left(-\frac{\gamma^2}{2M}\right) + \left(\frac{\pi\gamma}{4M^{1.5}}\right) - \left(\frac{\gamma}{2M^{1.5}}\right) arctan\left(\frac{\gamma^2}{M}\right)^{0.5} \quad \text{(A 5)}$$

where $\gamma = \frac{c}{a}$ and $M = 1 - \gamma^2$.

In the case of oblate ellipsoid, S is given as:

$$S = \frac{2}{\sqrt{a^2-c^2}} \tan^{-1} \frac{\sqrt{a^2-c^2}}{c} \quad \text{(A 6)}$$

Using equation (A 3) and (A 4), $\bar{R}$ = 3.29 × 10^{-9} m for IgG. Similarly, $\bar{R}$ = 6.8 × 10^{-9} m can be obtained for β-galactosidase using equation (A 3) and (A 6).

APPENDIX B

SUPPLEMENTAL MATERIAL FOR CHAPTER 5

Appendix B 1: Definition of Trapping Condition.

In a trapping DEP flow, the particle motions are strongly governed by DEP, and the direction of the flux is perpendicular to the electric field $\boldsymbol{E}$ ($\boldsymbol{J} \cdot \boldsymbol{E} = 0$) (Baylon-Cardiel, Lapizco-Encinas, Reyes-Betanzo, Chávez-Santoscoy, & Martínez-Chapa, 2009b; R. Davalos et al., 2008; Kwon, Maeng, Chun, & Song, 2008b). Using equation (3. 7) from the main manuscript while neglecting the diffusion term, one can write:

$$\boldsymbol{J} = c\left(\boldsymbol{u_{ek}} + \boldsymbol{u_{dep}}\right) \tag{B 1}$$

Arranging equation (B 1), we arrive at:

$$-\frac{\mu_{dep}\nabla \boldsymbol{E}^2}{\mu_{ek}\boldsymbol{E}^2} \cdot \boldsymbol{E} = 1 \tag{B 2}$$

Equation (B 2) allows us to determine the trapping condition. DEP dominates over the electrokinetic term when equation (B 2) is greater than 1. For values smaller than one electrokinesis dominates. Hence, trapping does not occur and streaming DEP is observed. In *Figure B-1*, the results from equation (B 2) computed with *COMSOL Multiphysics* are presented with an applied potential of 4200 V in a 1cm long channel. The mobilities for both cases were $\mu_{dep} = 8.6 \times 10^{-24}$ m^4/V^2s and $\mu_{ek} = 1.5 \times 10^{-8}$ m^2/Vs. I thus conclude that the trapping condition is not satisfied for this device because all values are in the order of 1×10^{-4} or smaller. Therefore, streaming behavior is expected to occur for proteins in this iDEP device. Note that streaming DEP is indeed observed in the here presented device experimentally. Thus, a possible cause for experimentally observed trapping in devices with similar or even larger post distances could originate from aggregate formation, as for example reported by Lapizco-Encinas et al.(Lapizco-Encinas,

Ozuna-Chacón, & Rito-Palomares, 2008b) With IgG, this is the case at pH ranges below 6 and above 8 in the here presented triangular post array (see main manuscript).

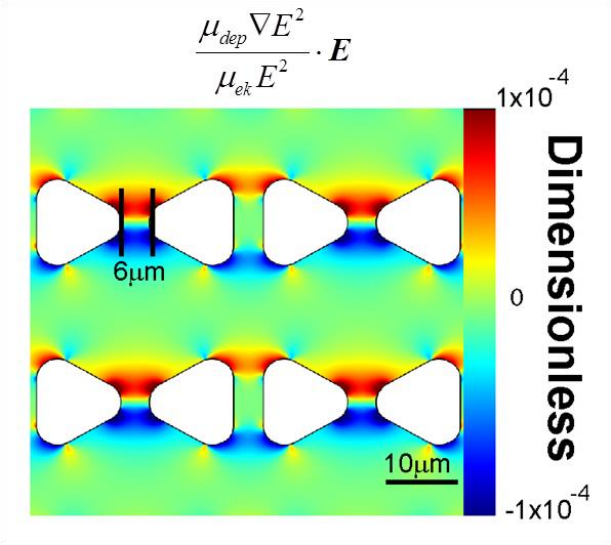

Figure B-1. Plotting the trapping condition (equation (B 2)) using *COMSOL* for proteins in the triangular structure as employed in the main manuscript. The applied potential is 4200 V in a 1cm long channel, μ_{dep} of 8.6×10^{-24} m^4/V^2s and μ_{ek} of 1.5×10^{-8} m^2/Vs.

Appendix B 2: Isoelectric focusing.

To investigate the isoelectric point of IgG used for DEP experiments, isoelectric focusing (IEF) was performed as reported earlier(Chao, Kalinowski, Nyalwidhe, & Hansmeier, 2010) with slight modifications. In short, protein samples were first desalted using centrifugal filters (Amicon Ultra-0.5 Ultracel-50 Membrane 50 kDa, Millipore, MA, USA). Subsequently, 100 µL of 2 mg/mL IgG protein (Invitrogen, Carlsbad, CA, USA) with or without 3 µL of IEF protein standard (Bio-Rad, Hercules ,CA, USA) were suspended in 350 µL rehydration buffer composed of 50 % glycerol and 2 % w/v CHAPS. The protein solution was loaded on IPG strips (Bio-rad, Hercules , CA, USA) of 24 cm length and linear pH gradient of 3 ~ 10 by means of passive rehydration. Protein was focused using a Protein IEF cell (Bio-rad) at 20 °C using a rapid ramp up to 8000 V

continuing until 80 kVh were reached. After IEF, the strips were fixed for 2 ~ 3 hours in a fixation solution composed of 10 % acetic acid, 40 % ethanol and water. Scanning of strips was performed with a scanner (Scanmaker i800, Microtek, CA, USA).

*Figure B-2*a-b shows the IPG strips for a) IEF protein standard of pI range 4.45 ~ 9.6 (Bio-rad, CA, USA) and b) the polyclonal Alexa488-labelled IgG, respectively. Numbers denote (1) phycocyanin with pI 4.45, 4.65 and 4.7, (2) myoglobin with pI 6.8 and 7 and (3) cytochrome C with pI 9.6 are naturally colored, thus they can be visualized without staining (see *Figure B-2*a), while for the strips with Alexa488-IgG a broad, yellow band is observed (*Figure B-2*b). The pI range is expected to be broad due to the polyclonal origin of IgG as well as glycosylation. Upon comparison of two strips the pI of Alexa488-IgG was found to be below 5.

Figure B-2. IEF of protein standard and polyclonal IgG protein. (a) The IPG strip contains IEF isoelectric point (pI) protein standards: (1) phycocyanin (pI 4.45, 4.65, 4.75), (2) myoglobin (6.8, 7.0) and (3) cytochrome c (9.6). (b) The IPG strip of fluorescently labeled Alexa488-IgG.

Appendix B 3: Dynamic light scattering (DLS).

Dynamic light scattering (DLS) was employed in order to investigate F108 micelle formation above the critical micelle concentration (CMC) in relation to the negative DEP behavior observed under F108 dynamic coating condition. DLS measurement was performed using a DynaPro NanoStar instrument (Wyatt Technology Corp. Santa Barbara, CA, USA). Data collection and analysis were performed with the instrument's software DYNAMICS. For sample preparation, all buffers were filtered with a 20 nm filter with IgG protein.

The temperature dependent micellation of F108 was studied with a 3.3 nM IgG sample diluted with pH 8 phosphate buffer containing 3 mM F108 and 1.6 mM CHAPS. *Figure B-3*a shows that the light scattering intensity increases drastically above 25 °C, indicating the formation of larger species at this temperature presumably arising from F108 micelle formation. The size distribution in *Figure B-3*b at temperatures below and above the critical micelle concentration clearly indicates the formation of large species at elevated temperature. The observed size of this species (~ 9.7 nm) in our experiment is in excellent agreement with the previously reported value of ~ 10 nm for F108 micelles by Alexandridis et al..(Alexandridis, Nivaggioli, & Hatton, 1995) I thus conclude that F108 micelles are present at iDEP conditions used in our study (see main manuscript).

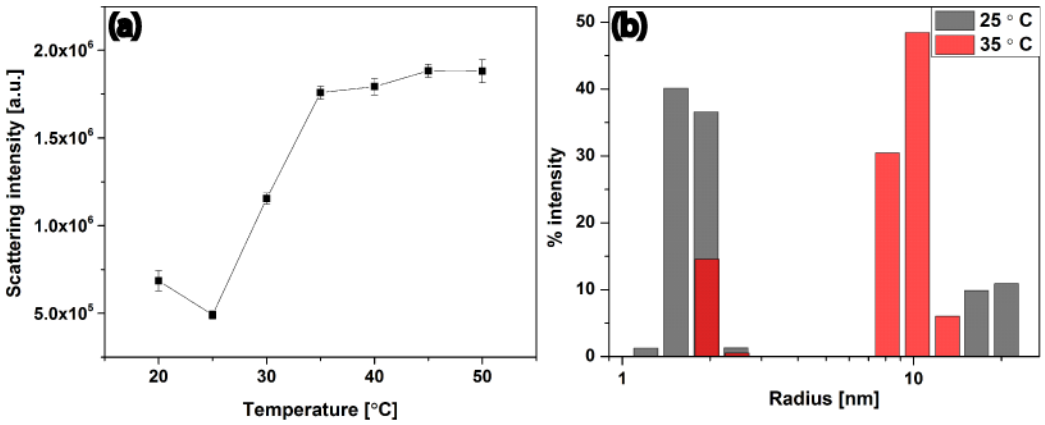

Figure B-3. Results of DLS study: (a) scattering light intensity plotted as a function of temperature from 20 °C to 50 °C. The abrupt increase in light scattering intensity at 30 °C indicates the formation of F108 micelles. (b) radius distribution in terms of % intensity for a 3 mM F108 containing 3.3 nM Alexa488-IgG sample and 1.6 mM CHAPS.

APPENDIX C

SUPPLEMENTAL MATERIAL FOR CHAPTER 7

Appendix C 1: Influence of heat transfer coefficient on temperature.

This supplemental information demonstrates the influence of the variation of heat transfer coefficient (h) value on the resultant temperature in the iDEP device via numerical modeling.

To numerically model temperate distribution in the iDEP device, numerical simulations were performed as described in the Method section of the main manuscript. Upon solving the model, the condition of the outer surface of the device was set as a natural convection heat transfer with surrounding air for which the value of $10 \sim 20$ W/m^2 s can be reasonably employed. However, instead of $h = 20$ W/m^2 s (results shown in the main text), $h = 30$ W/m^2 s was herein employed to investigate the influence of variation of h on temperature.

*Figure C-1*a shows the temporal temperature variations simulated numerically using the domain employed in method A for each buffer conductivity (100 µS/cm and 1 mS/cm), revealing that the saturation temperature resulted in lower value than the temperature simulated using $h = 20$ W/m^2 s. Especially in the case of 1 mS/cm at 3000 V/cm, the saturation temperature declined by 18 ºC (90 ºC with $h = 20$ as shown in the main manuscript).

In *Figure C-1*b, the temporal temperature variations were numerically calculated for method B where temperature value was obtained 150 µm below the channel. Similar to the previous temperature variations in method A, the overall temperature values decreased compared to the temperature at $h = 20$. Specifically in the case of 1 mS/cm at 3000 V/cm, the saturation temperature resulted in ~ 39 ºC in contrast to ~ 45 ºC obtained employing $h = 20$.

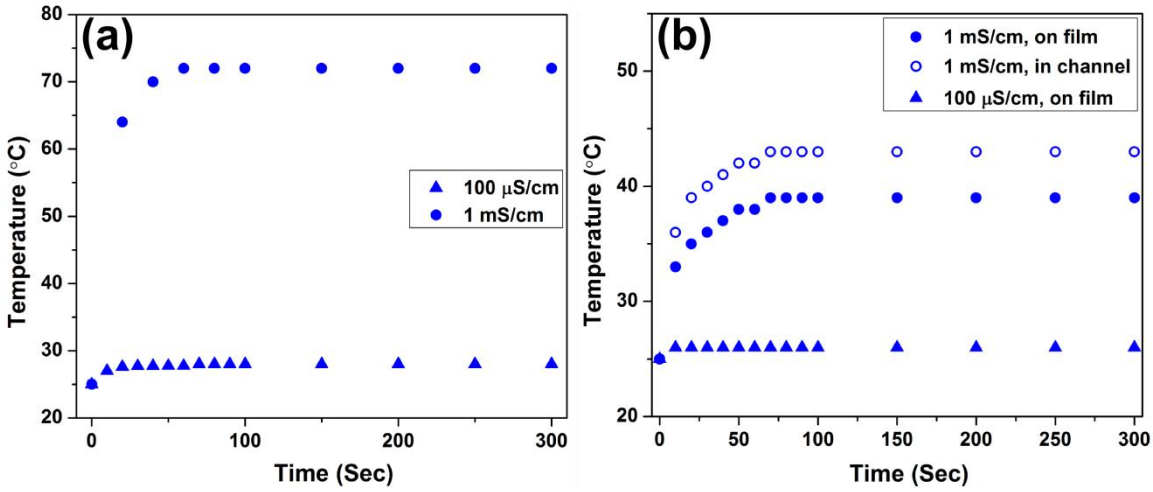

Figure C-1. (a) Temporal temperature variations obtained numerically in method A for 100 μS/cm (triangles) and 1 mS/cm (dots) when 3000 V is applied. (b) Temporal temperature variations obtained numerically in method B for 100 μS/cm (triangles), 1 mS/cm on the film (filled circles), and in the channel (non-filled circles) when 3000 V is applied.

APPENDIX D

SUPPLEMENTAL MATERIAL FOR CHAPTER 8

Appendix D 1: Preparation of Aβ monomers and oligomers

Aβ peptides 1-42 (American peptide company, Sunnyvale CA, USA) are very hydrophobic and will almost immediately aggregate in water-soluble buffers. This preparation will retard the rate of aggregation.

The received Aβ peptides were dissolved in 1,1,1,3,3,3-hexafluoro-2-propanol (HFIP) (100%) at a peptide concentration of 1 mM to avoid forming aggregates. HFIP breaks hydrogen-bond used to eliminate pre-existing structural inhomogeneities in the received Aβ peptides. Subsequently, Aβ peptides were sonicated at a water bath at 37 ºC for 1.5 hours to completely solubilize them, separated in aliquots of 100 µL each, dried under vacuum overnight, and stored at ~ 20 ºC until future use (Liu, Barkhordarian, Emadi, Park, & Sierks, 2005). For monomer preparation, Aβ peptides were prepared immediately before used to minimize potential aggregation. First, Aβ peptides were resuspended in DMSO to 5 mM concentration, briefly vortexed, and sonicated for 5 min at room temperature. Subsequently, Aβ peptides were further diluted to 50 µg/mL (11 µM) concentration in 1x PBS (Ryan, Narrow, Federoff, & Bowers, 2010), vortexed for 15 sec, and used immediately. For oligomer preparation, Aβ peptides were first resuspended in DMSO to 5 mM concentration, briefly vortexed, sonicated in a water bath for 5 mins, and filtered through a sterile 0.22 µm filter. Aβ peptides/DMSO solution were mixed slowly with cold PBS (pH 7.4) and 0.05 % SDS to 100 µM (Ryan et al., 2010). In the mixture sonicated for 10 min at room temperature, aggregation was allowed to proceed for 24 hours at 4 ºC. Finally, the peptide solution was further diluted with PBS to 50 µg/mL and incubated for 2 weeks at 4 ºC to facilitate higher order aggregation.

The resultant Aβ species were imaged via atomic force microscopy with intermittent contact mode with a MFP-3D BIO (Asylum Research, Goleta, CA, USA) which confirmed the formation of Aβ species (see *Figure D-1*). The size of resultant Aβ species ranges widely, including 4 ~ 7 nm height and ~ 30 nm lateral dimension, ones of 6 ~ 8 nm height and ~ 50 nm lateral dimensions, and larger species of > 15 nm height. The smallest observed size is similar to the reported dimension of the high MW Aβ oligomers, while the 6 ~ 8 nm height and ~ 50 nm lateral dimensions are close to the size of protofibrils (Mastrangelo et al., 2006; Stine, Dahlgren, Krafft, & LaDu, 2003). Note the small species such as monomers are difficult to be observed with our AFM due to the external noise.

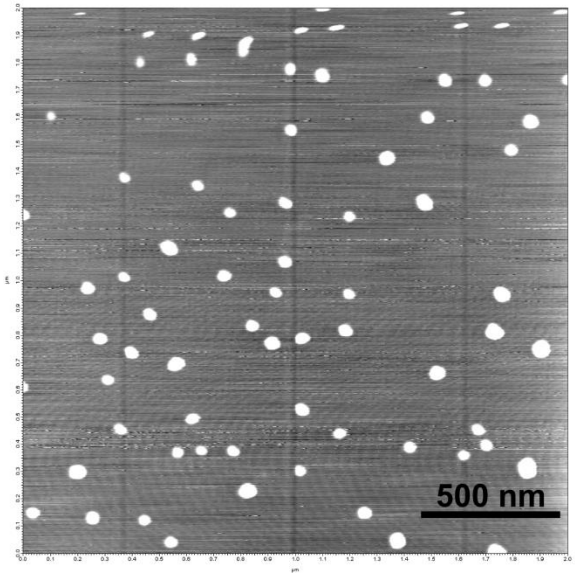

Figure D-1. Atomic force microscopy image of prepared Aβ species with 100 nM peptide concentration.

Appendix D 2: Preparation of lysozyme oligomers

Lysozyme (Sigma-Aldrich, St. Louis, MO, USA) was originally dissolved in a buffer of 25 mM sodium acetate pH 4.5 in 50 % glycerol. Therefore, the buffer was exchanged to a buffer containing 20 mM HEPES and 40 mM NaCl at pH 7 using a 3 kDa centrifugal filter (Amicon Ultra-0.5 Ultracel-50 Membrane, Millipore, MA, USA). After the buffer exchange, the solution was placed in a water bath at 70 º C. After 22 hours of incubation, size distribution of lysozyme was determined by AFM (see *Figure D-2*), revealing the presence of species (4 ~ 5 nm height, ~ 10 nm lateral dimension) matching with the size previously reported for lysozyme oligomers (Frare et al., 2009; Hill et al., 2011).

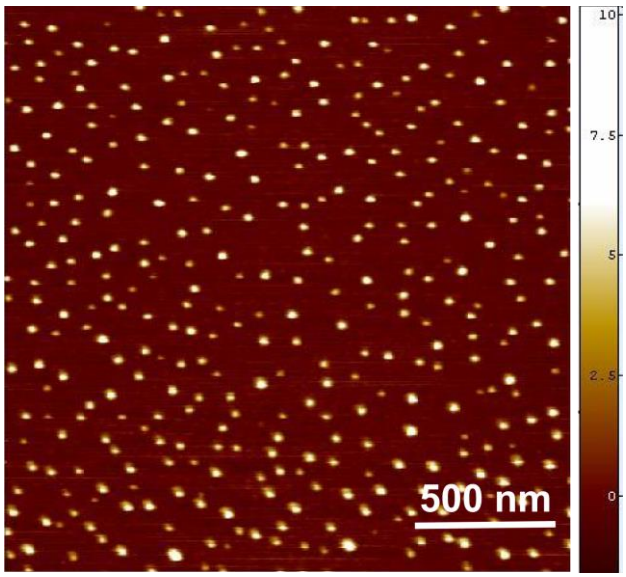

Figure D 2. Atomic force microscopy image of lysozyme with 150 nM concentration.

APPENDIX E

COPYRIGHT PERMISSIONS

JOHN WILEY AND SONS LICENSE
TERMS AND CONDITIONS

Mar 27, 2014

This is a License Agreement between asuka nakano ("You") and John Wiley and Sons ("John Wiley and Sons") provided by Copyright Clearance Center ("CCC"). The license consists of your order details, the terms and conditions provided by John Wiley and Sons, and the payment terms and conditions.

All payments must be made in full to CCC. For payment instructions, please see information listed at the bottom of this form.

License Number	3357280404233
License date	Mar 27, 2014
Licensed content publisher	John Wiley and Sons
Licensed content publication	Electrophoresis
Licensed content title	Immunoglobulin G and bovine serum albumin streaming dielectrophoresis in a microfluidic device
Licensed copyright line	Copyright © 2011 WILEY-VCH Verlag GmbH & Co. KGaA, Weinheim
Licensed content author	Asuka Nakano,Tzu-Chiao Chao,Fernanda Camacho-Alanis,Alexandra Ros
Licensed content date	Jul 27, 2011
Start page	2314
End page	2322
Type of use	Dissertation/Thesis
Requestor type	Author of this Wiley article
Format	Print and electronic
Portion	Full article
Will you be translating?	No
Title of your thesis / dissertation	Protein Dielectrophoresis Using Insulator-based Microfluidic Platforms
Expected completion date	May 2014

Expected size (number of pages)	180
Total	0.00 USD

Terms and Conditions

Terms and Conditions are not available at this time.

If you would like to pay for this license now, please remit this license along with your payment made payable to "COPYRIGHT CLEARANCE CENTER" otherwise you will be invoiced within 48 hours of the license date. Payment should be in the form of a check or money order referencing your account number and this invoice number RLNK501262972.
Once you receive your invoice for this order, you may pay your invoice by credit card. Please follow instructions provided at that time.

Make Payment To:
Copyright Clearance Center
Dept 001
P.O. Box 843006
Boston, MA 02284-3006

For suggestions or comments regarding this order, contact RightsLink Customer Support: customercare@copyright.com or +1-877-622-5543 (toll free in the US) or +1-978-646-2777.

Gratis licenses (referencing $0 in the Total field) are free. Please retain this printable license for your reference. No payment is required.

JOHN WILEY AND SONS LICENSE TERMS AND CONDITIONS

Mar 27, 2014

This is a License Agreement between asuka nakano ("You") and John Wiley and Sons ("John Wiley and Sons") provided by Copyright Clearance Center ("CCC"). The license consists of your order details, the terms and conditions provided by John Wiley and Sons, and the payment terms and conditions.

All payments must be made in full to CCC. For payment instructions, please see information listed at the bottom of this form.

License Number	3357280476419
License date	Mar 27, 2014
Licensed content publisher	John Wiley and Sons
Licensed content publication	Electrophoresis
Licensed content title	Protein dielectrophoresis: Advances, challenges, and applications
Licensed copyright line	© 2013 WILEY-VCH Verlag GmbH & Co. KGaA, Weinheim
Licensed content author	Asuka Nakano,Alexandra Ros
Licensed content date	Apr 2, 2013
Start page	1085
End page	1096
Type of use	Dissertation/Thesis
Requestor type	Author of this Wiley article
Format	Print and electronic
Portion	Full article
Will you be translating?	No
Title of your thesis / dissertation	Protein Dielectrophoresis Using Insulator-based Microfluidic Platforms
Expected completion date	May 2014

Expected size (number of pages)	180
Total	0.00 USD

Terms and Conditions

Terms and Conditions are not available at this time.

If you would like to pay for this license now, please remit this license along with your payment made payable to "COPYRIGHT CLEARANCE CENTER" otherwise you will be invoiced within 48 hours of the license date. Payment should be in the form of a check or money order referencing your account number and this invoice number RLNK501262973.
Once you receive your invoice for this order, you may pay your invoice by credit card. Please follow instructions provided at that time.

Make Payment To:
Copyright Clearance Center
Dept 001
P.O. Box 843006
Boston, MA 02284-3006

For suggestions or comments regarding this order, contact RightsLink Customer Support: customercare@copyright.com or +1-877-622-5543 (toll free in the US) or +1-978-646-2777.

Gratis licenses (referencing $0 in the Total field) are free. Please retain this printable license for your reference. No payment is required.

AIP PUBLISHING LLC LICENSE
TERMS AND CONDITIONS

Mar 27, 2014

All payments must be made in full to CCC. For payment instructions, please see information listed at the bottom of this form.

License Number	3357280009857
Order Date	Mar 27, 2014
Publisher	AIP Publishing LLC
Publication	Biomicrofluidics
Article Title	Tuning direct current streaming dielectrophoresis of proteins
Author	Asuka Nakano,Fernanda Camacho-Alanis,Tzu-Chiao Chao, et al.
Online Publication Date	Aug 2, 2012
Volume number	6
Issue number	3
Type of Use	Thesis/Dissertation
Requestor type	Author (original article)
Format	Print and electronic
Portion	Excerpt (> 800 words)
Will you be translating?	No
Title of your thesis / dissertation	Protein Dielectrophoresis Using Insulator-based Microfluidic Platforms
Expected completion date	May 2014
Estimated size (number of pages)	20
Total	0.00 USD

Terms and Conditions

AIP Publishing LLC -- Terms and Conditions: Permissions Uses

AIP Publishing LLC ("AIPP"") hereby grants to you the non-exclusive right and license to use and/or distribute the Material according to the use specified in your order, on a one-time basis, for the specified term, with a maximum distribution equal to the number that you have ordered. Any links or other content accompanying the Material are not the subject of this license.

This Agreement shall be governed by and construed in accordance with the laws of the State of New York. Both parties hereby submit to the jurisdiction of the courts of New York County for purposes of resolving any disputes that may arise hereunder.

If you would like to pay for this license now, please remit this license along with your payment made payable to "COPYRIGHT CLEARANCE CENTER" otherwise you will be invoiced within 48 hours of the license date. Payment should be in the form of a check or money order referencing your account number and this invoice number RLNK501262964.
Once you receive your invoice for this order, you may pay your invoice by credit card. Please follow instructions provided at that time.

Make Payment To:
Copyright Clearance Center
Dept 001
P.O. Box 843006
Boston, MA 02284-3006

For suggestions or comments regarding this order, contact RightsLink Customer Support: customercare@copyright.com or +1-877-622-5543 (toll free in the US) or +1-978-646-2777.

Gratis licenses (referencing $0 in the Total field) are free. Please retain this printable license for your reference. No payment is required.